

2024-09-16

# Quantifying Ionospheric Electron Density Enhancements and their Impact on High Frequency Radio Wave Propagation

Ghaly, Filobateer

---

Ghaly, F. (2024). Quantifying ionospheric electron density enhancements and their impact on high frequency radio wave propagation (Master's thesis, University of Calgary, Calgary, Canada). Retrieved from <https://prism.ucalgary.ca>.

<https://hdl.handle.net/1880/119764>

*Downloaded from PRISM Repository, University of Calgary*

UNIVERSITY OF CALGARY

Quantifying Ionospheric Electron Density Enhancements and their Impact on High Frequency Radio Wave  
Propagation

by

Filobateer Ghaly

A THESIS

SUBMITTED TO THE FACULTY OF GRADUATE STUDIES  
IN PARTIAL FULFILMENT OF THE REQUIREMENTS FOR THE  
DEGREE OF MASTER OF SCIENCE

GRADUATE PROGRAM IN PHYSICS AND ASTRONOMY

CALGARY, ALBERTA

SEPTEMBER, 2024

## Abstract

This thesis presents two related projects that investigate the impact of space weather on radio signals. The first project examines a new, prototype riometer, the Space Weather Adaptive Network (SWAN) Hyper Spectral Riometer (HSR), which can measure both terrestrial radio signals and Cosmic Noise Absorption (CNA). The simultaneous loss of both signals in the data can be used to estimate the size of electron density enhancements in the D-region. The second project investigates the use of existing riometers and a High Frequency (HF) transmitter-receiver circuit to predict radio signal fadeout during space weather events. By analyzing riometer absorption data, this project aims to establish thresholds that can be used for nowcasting radio disruptions. The project will quantify the probability of fadeout at different frequencies based on riometer absorption levels and examine the influence the position of the riometer has on its ability to nowcast. These projects aim to improve our understanding of how space weather affects radio signals and will ultimately help in the mitigation and reliability of HF communication and navigation systems.

# Preface

This thesis is an original work by the author.

**Chapter 4** of this thesis contains some wording and figures that have been published in:

Ghaly, F., Spanswick, E., Gillies, R., Cameron, T., Skone, S., Fiori, R. a. D., & Weatherwax, A. T. (2024). Use of Terrestrial High Frequency Signals in Riometer Data to Explore the Size of D-Region Electron Density Enhancements. *Journal of Geophysical Research: Space Physics*, 129(5), e2023JA032375.  
<https://doi.org/10.1029/2023JA032375>

# Acknowledgements

I would like to thank everyone who helped me get to where I am. First and foremost, I'd like to thank my family. You guys are my world. I always want to make you proud...

Thanks to Fam, my brother, for bearing my existence during times when I'm unbearable (always). I am surprised you still didn't wanna move out (*edit: it got close lol*).

Thanks to Reece and Shayne. You guys are family too. You both helped me so much and taught me lessons that some never get to learn. I am forever grateful to everything you have done for me. I never forget...

Thanks to everyone I met along the way... everyone I met has taught me something.

When I started working with Dr. Emma, I met her team. Lukas Vollmerhaus and Darren Chaddock, I learned a lot from you both. Lukas, you were the first person I met, and you helped me get started with the data and showed me how the lab equipment worked. You were always there when I asked for help.

Darren... I'm gonna miss you lol. Had a lot of fun and learned a ton from you. You're an IT genius. But you don't need me to tell you that...

Dr. Robert Gillies. You have been guiding me since I started my undergraduate project, always offering your time, expertise, and helping me in almost every step of the way. You are humble beyond means and truly gifted in this line of work. You are the one person I bugged the most, and yet not once did you turn me down. I am grateful to you and wish you all the best; you deserve it.

Dr. Taylor Cameron. You were also there from the start helping me. When we started the second

project, you offered your guidance almost every week. You helped me kickstart the project during my visit to NRCan. Your expertise with data analysis and extensive knowledge of HF propagation has helped me tremendously on many occasions. Your support throughout, including the meetings towards the end of my thesis, is something I am incredibly thankful for.

I also want to thank the NRCan team. Dr. Robyn Fiori, Dr. David Boteler, and everyone there is very welcoming. Dr. Robyn, I am glad I came in contact with you. You helped a lot with the paper. You are detail oriented and your feedback when writing was critical. I appreciate the effort from your side and am grateful for all the time you spent helping. All the best.

To everyone who has helped me, I hope I can pay it forward...

Finally... I would like to thank Dr. Emma Spanswick. You are the only reason I am here now. Without your faith in me, I would not be pursuing an MSc. This degree has been quite the journey for me. My family and friends noticed how I have changed throughout the years. And it started with being your TA that one summer. That was my favorite summer so far. Ever since, I learned so much... about coding, physics, but mostly about myself, and how to tackle problems, regardless of what they are. Being your student has taught me resilience, problem-solving, and attention to detail. Above all, however, it taught me how to be a true student and reignited my passion in physics. I am incredibly grateful for this opportunity. Without you, I would not be where I am today.

Thank you...

To Dr. Emma Spanswick...

# Table of Contents

<b>Abstract</b>	ii
<b>Preface</b>	iii
<b>Acknowledgements</b>	iv
<b>Dedication</b>	vi
<b>Table of Contents</b>	ix
<b>List of Figures</b>	xiv
<b>List of Tables</b>	xv
<b>List of Symbols, Abbreviations, and Nomenclature</b>	xvi
<b>Epigraph</b>	xix
<b>1 Introduction</b>	1
1.1 Space Weather . . . . .	1
1.1.1 Solar Radiation . . . . .	1
1.1.2 Energetic Particle Precipitation . . . . .	2
1.2 Research Goals . . . . .	3
1.2.1 Modelling the Spatial Extent of Regions of Enhanced Electron Density . . . . .	4
1.2.2 Developing a Threshold Riometer Absorption . . . . .	4
1.3 Outline of Thesis . . . . .	4
<b>2 Theory and Background</b>	6
2.1 Radiowave Propagation in The Ionosphere . . . . .	6
2.1.1 Ionospheric Layers . . . . .	6
2.1.2 Magnetoionic Theory . . . . .	8
2.1.3 Dispersion Relation . . . . .	9
2.2 Collisions . . . . .	20
2.3 Effects of Earth's Magnetic Field . . . . .	23
2.3.1 Anisotropic Medium . . . . .	23
2.3.2 Quasi-Longitudinal Approximation . . . . .	25
2.3.3 Trans-ionospheric Propagation . . . . .	26
2.4 Relevant Absorption Phenomena . . . . .	27
2.4.1 Short Wave Fadeout . . . . .	27
2.4.2 Polar Cap Absorption . . . . .	28
2.4.3 Auroral Absorption . . . . .	30

<b>3 Data and Instrumentation</b>	<b>31</b>
3.1 Solar and Geomagnetic Indices . . . . .	31
3.2 Riometers . . . . .	31
3.2.1 Baselines . . . . .	35
3.2.2 Prototype Hyperspectral Riometers . . . . .	39
3.2.3 The GO-Canada Riometer Network . . . . .	42
3.2.4 Event Signatures in Riometer Data . . . . .	43
3.3 High-Frequency Radio Transmitters and Receivers . . . . .	48
3.3.1 Natural Resources Canada Network . . . . .	49
3.3.2 Timing-Signal Transmitters . . . . .	52
<b>4 Remote Sensing Electron Density Enhancements</b>	<b>53</b>
4.1 Motivation and Goal . . . . .	53
4.2 Sources of Electron Density Enhancements . . . . .	55
4.3 Project Outline . . . . .	56
4.4 Methodology . . . . .	57
4.4.1 Identifying the Source of Terrestrial HF Signals . . . . .	57
4.4.2 Ray Tracing . . . . .	62
4.5 Event Study . . . . .	64
4.6 Discussion . . . . .	69
<b>5 Riometer Absorption Thresholds</b>	<b>73</b>
5.1 Motivation and Goal . . . . .	73
5.2 Project Outline . . . . .	74
5.3 Data Preparation . . . . .	75
5.3.1 Riometer Data . . . . .	75
5.3.2 HF Link Data . . . . .	75
5.4 Data Analysis . . . . .	85
5.5 Discussion . . . . .	89
<b>6 Conclusions and Future Work</b>	<b>91</b>
6.1 Conclusions . . . . .	91
6.2 Future Work . . . . .	92
6.2.1 HF Enhancements . . . . .	92
6.2.2 Frequency Dependence . . . . .	96
6.2.3 Link Status and D-region Electron Density using HSRs . . . . .	98
<b>Bibliography</b>	<b>99</b>
References . . . . .	99
<b>A Proofs and Derivations</b>	<b>110</b>
A.1 Plasma Electric Field . . . . .	110
A.2 Evanescent Waves . . . . .	112
A.2.1 Poynting Flux . . . . .	112
A.2.2 Total Internal Reflection . . . . .	114
A.3 The Fourier Trick . . . . .	116
A.4 Absorption Coefficient . . . . .	117
A.4.1 With Collisions, No Magnetic Field . . . . .	117
A.4.2 Quasi-Longitudinal, Trans-ionospheric Waves . . . . .	118
A.5 Appleton-Hartree Equation . . . . .	120
<b>B Realtime Baselining</b>	<b>125</b>
B.1 Baselining . . . . .	125
B.2 Frequency Dependence . . . . .	138



# List of Figures

1.1 Illustration of the day-side ionosphere exposed to a solar flare. A flare increases the ionization on the day-side, with more electron density closer to the subsolar point. Radiowaves passing through these enhanced regions lose their energy and fail to propagate further. . . . .	2
3figure.1.2	
2.1 Example electron density profiles for the (a) daytime ionosphere, and (b) the nighttime ionosphere. This simulation of electron density is obtained using the International Reference Ionosphere (IRI) model of 2016. . . . .	7
2.2 The electrons are bound to the relatively stationary ions. Any electrostatic disturbance (a) polarizes the medium, and leads to an oscillatory motion (b). . . . .	10
2.3 Illustration of (a) skywave- and (b) transionospheric- propagation, and (c) evanescent waves. . . . .	13
2.4 The plasma frequency profiles derived from the electron density profiles in Figure 2.1. . . . .	14
2.5 A plane ionosphere can be illustrated as a mirror, where the wave, incident at an angle $\theta$ will reflect at some virtual height $h'$ , covering a ground range distance $D$ . . . . .	15
2.6 A wave reflecting off a layer with frequency $f_p$ will have to have a higher frequency if it were incident at the same layer but via a higher incidence angle. . . . .	17
2.7 Every angle of incidence corresponds to two distinct distances on the ground, as the ray might reflect off of a different height. Alternatively, given a radio frequency one can achieve the same ground range by pointing the antenna at two distinct incidence angles, one high and the other low. The dotted line shows that 23.5 MHz is the MUF for a 2000 km link, given the plasma frequency profile in Figure 2.4 . . . . .	18
2.8 Illustration showing the geomagnetic field, which is roughly horizontal at the equator, and roughly vertical at high latitudes. The propagation dynamics of the radiowave depend on how the wave normal is oriented with respect to the geomagnetic field- whether it is perpendicular (transverse) or parallel (longitudinal) to the field. For high latitudes, orienting the wave normal with the z-axis of our coordinate system, with the geomagnetic field in the xz-plane, trans-ionospheric waves line up with the field such that $\theta \approx 0$ . . . . .	25
2.9 Illustration of the polar cap and auroral zone. . . . .	28
3.1 Picture showing a riometer site. . . . .	32
3.2 Illustration of the nominal riometer FOV, defined as the cone encapsulating the half-power points when projected to D-region altitudes of $\sim 85$ km. . . . .	34
3.3 As the Earth completes one full rotation about its orbital axis, traveling the $\sim 1^\circ$ of arc greatly exaggerated in the figure, it faces the distant stars. A further rotation of $\Delta\theta$ (much exaggerated) is required to face the Sun again. . . . .	35
3.4 Data from a quiet day. Signal voltage level is recorded as a function of Coordinated Universal Time (UTC) for a riometer operating at 30 MHz. Data taken from a riometer at Prince George. . . . .	36
3.5 The signature of solar radio bursts in riometer data. Shown is signal voltage as a function of time. Radio burst signatures are highlighted in red. The regular downward spikes in signal levels are simply calibration spikes. Data taken from a riometer at Rankin Inlet. . . . .	37

3.6	A map of riometers used in this study. The HSRs are shown as gray circles with red boundaries, indicating the nominal FOV as projected to 85 km altitude, covering $\sim$ 200 km in diameter across. The GO-Canada riometers FOVs are indicated via gray circles with black boundaries, covering $\sim$ 100 km in diameter. To note is an HSR colocated with a GO-Canada riometer at Rabbit Lake (RABB) and Prince George (PGEON), with uppercase denoting the HSR. For each HSR and their site code, refer to Table 3.1. . . . .	39
3.7	Panel (A) (left) shows full spectrum data for signals in the range 0.01–49.50 MHz from an HSR at Meanook (MEAN). Panel (B) (right) shows observed power in a 195 kHz (16 bins) passband centered around 30.51 MHz as a function of time. . . . .	40
3.8	The signature of SWF in riometer data. The top right panel shows the HSR full spectrum data from 7 May 2024. On the left, from the top down are plots for solar X-ray flux from GOES, the 30 MHz signal levels for the HSRs at Polar Flat (PFRR) and Prince George (PGEON), followed by the GO-Canada riometer voltage levels at Lake Dawson (daws), Rankin Inlet (rank) and (gill), for a period of time surrounding the SWF event, highlighted in red. The 30 MHz signal for PGEON is indicated by a dashed line on the full spectrogram. In the bottom right is a map showing where each riometer is located in relation to the solar terminator. . . . .	44
3.9	The signature of AA in riometer data. On the top right is the PGEON HSR full spectrum data, with power at 30 MHz indicated using the black dashed line. On the left, from the top down are the CARISMA AE index values, then the PFRR and PGEON HSR signal levels at 30 MHz, followed by the 30 MHz voltage levels for the GO riometers at <i>daws</i> , <i>rank</i> , <i>fsmi</i> , <i>chur</i> , <i>rabb</i> , <i>gill</i> , and <i>pgeo</i> , in that order, for the time of the event. The rise in AE index correlates with the activity, as indicated by the event time, highlighted in red. At the bottom right is a map to facilitate an understanding of the temporal and spatial signatures of the AA. The solar terminator is marked by the shaded region. . . . .	47
3.10	Map showing all HF transmitters and receivers used. Exact locations of the corresponding site codes, shown here, are listed in Tables 3.3, 3.5, and 3.4. NRCan's transmitter at Ottawa (OTTW) is close to NRC's CHU transmitter, hence they overlap on the map due to proximity. . . . .	48
3.11	Figure showing the SNR for the NRCan transmission frequencies as a function of time, as observed in the ALRT receiver data for the 21 <sup>st</sup> of September, 2019. . . . .	50
3.12	Data availability for the HF radio dataset for the OTTW to ALRT link for the year 2014. Brown dots within each day imply a signal was received and successfully decoded. If a day is totally missing data, it is marked by white. A day with even one reception is marked orange. Receptions vary by frequency, time of day, and season. . . . .	51
4.1	Riometer measurements from Meanook (MEAN) on 13 March 2022. Panel (A) (left) shows the full spectrum, from 0.01–49.50 MHz. An absorption event (loss of HF power) marked with a vertical dashed line begins at approximately 13:15 UT. The sub-panel shows the distinct loss of terrestrial HF signals at the dashed line. The inset axis shows power for signals with frequencies ranging from 1 to 21 MHz. Panel (B) is the equivalent riometer signal of a 30 MHz, single channel riometer, derived from the multi-frequency data. The cosmic absorption is marked with the same dashed line. . . . .	54
4.2	Example events from each of the HSRs from the prototype network. Highlighted in gray are times when CNA was simultaneous with loss of terrestrial signals. I focus on MEDO 21 February 2023 (right-most plot) for applying our methodology. . . . .	54
4.3	One-second power measurements from the HSR at Rabbit Lake (RABB) in the 5.37–5.39 MHz frequency range (black dots). Times of the 5.382 MHz transmissions from the NRCan transmitters at Yellowknife (YKNF) and Fort Churchill (FCHU) are shown as vertical lines (black and red, respectively). The noise floor at this frequency, for this period, is indicated with the horizontal gray line. . . . .	58
4.4	Superposed epoch analysis of riometer power at Rabbit Lake (RABB) in the 5.37–5.39 MHz band for 32 successive NRCan transmission cycles. Zero time is the time of the Yellowknife transmission. The timing of the Fort Churchill transmissions within the cycle is also shown. Churchill transmits 10 seconds after Yellowknife (1 <sup>st</sup> transmission). . . . .	59

4.5	Example riometer spectrum from Meanook (MEAN) for, 2 August 2021, showing the frequency range 9.75 to 10.25 MHz. The WWV/WWVH transmission at 10.00 MHz is identified (bordered by white dashed lines) . . . . .	60
4.6	(a) Simulation of ray paths for a signal at 15.00 MHz transmitted from WWV at a range of elevation angles along an azimuth towards Meadow Lake (MEDO). The ray-path that reaches MEDO is plotted in red. The FOV, a cone enclosing the half-power points of the antenna's radiation pattern, of the MEDO HSR is shown in red at the HSR site, terminating at the assumed absorbing altitude of 85 km. The minimum size of the absorbing region (shown as a green extension from the center of the cone) is assumed to be the distance from the center of the HSR's FOV to the pierce point of the red ray at 85 km altitude. For comparison, the subfigure (b), a zoomed-in version of (a), shows absorption distances and FOV projections at 55, 65, 75, 85, and 95 km altitudes. . . . .	64
4.7	An absorption event on 21 February 2023. HSR measurements taken from Meadow Lake (MEDO). Shown is the observed power at 30 MHz, with a passband of 195 kHz. The dashed line indicates the onset used in mapping the absorption region. . . . .	65
4.8	Spectra showing terrestrial transmissions for the 21 February 2023 event as observed by the Meadow Lake (MEDO) HSR. In order from top to bottom are plots showing the 14.67 MHz transmission by CHU, followed by 10 and then the 15 MHz transmissions by WWV/WWVH. The appropriate frequency bin is bordered by white dashed lines. Observed is simultaneous reduction of power for these terrestrial transmissions at the onset of absorption marked by the black dashed line. . . . .	66
4.9	The observed power in the 11.1084 MHz bin corresponding to the 11.107 MHz band in which NRCan transmits. Known transmission times for YKNF, FCHU and OTTW are marked by red triangles, circles, and rectangles, respectively. Observed is an instantaneous loss of the OTTW transmissions at the time of the event, highlighted in red. . . . .	67
4.10	Map showing the pierce-point of the rays that reach the riometer prior to absorption onset for the event on 21 February 2023. Ray traces were performed at 20:10 UT and 7.85 MHz for CHU, 10 and 15 MHz for WWV/WWVH, and 11.107 MHz for NRCan's Ottawa (OTTW) and transmitter. The HSR's FOV is projected to 85 km altitude. . . . .	68
4.11	Absorption measurements from the GO-Canada riometers for the day of the 21 February 2023. Peak absorption during the time of the event (highlighted in red), is shown by a horizontal red line along with the measurement of peak absorption above it (written in red). The site code is displayed on the top left corner of each plot. . . . .	69
4.12	Map showing the pierce points extracted via applying our methodology to both the Meanook (MEAN) and Meadow (MEDO) HSRs. The clustering of pierce points defines the boundary of the absorbing region. GO-Canada riometers, shown as gray circles with black boundaries, have been added to the map. Additionally, GO-Canada riometers with peak absorption of 0.5 dB or higher are marked with a red diamond behind the gray circle. The subsolar point is shown as a yellow star and the boundary of the solar terminator is marked by the shaded region. The distance from each riometer to different pierce points (red dashed lines) is indicated next to each pierce point. One pierce point connecting CHU to MEAN is located within MEDO's FoV. . . . .	70
5.1	Riometer absorption, shown in red, is filtered via the Kaiser window shown in the inset axis, and the filtered absorption is shown in black. . . . .	76
5.2	The distribution of occurrences for the 5.382 MHz transmissions for the whole dataset (left) and only a subset that included data from after 2016 (right). The peak at 4 occurrences for the distribution on the left is due to the maximum transmissions capped at 4 for data before 2016. . . . .	77

5.3	Baselining procedure for April 18, 2014 for the 5.382 MHz transmissions, using OMNI AE Index, GOES proton, and X-ray flux to identify disturbed times. Below these indices, shown in red and marked 1 are these disturbed hours. Below that is a sum, showing the number of disturbed hours in a 24-hour convolutional window. At the bottom are the normalized occurrences within each hour. Highlighted in green are the quiet times used in generating the baseline. . . . .	81
5.4	Hourly baseline for 5.382 MHz signal derived from quiet-time occurrences via the procedure in Figure 5.3. The daytime, highlighted in yellow, delineates the diurnal variation, as 5.382 MHz signals cannot propagate during the day. . . . .	82
5.5	The distribution of baseline values for 0 (left) and 8 (right) occurrences (the maximum) for 5.382 MHz. The inset axis shows a few enhancements, indicated by the values of the baseline $< 1$ . . . . .	82
5.6	Same as Figure 5.2 but after eliminating data with $B_N \leq 0.1$ . . . . .	83
5.7	The dropouts as measured relative to the maximum (x-axis) versus as measured relative to the baseline (y-axis). The colors as given by the colorbar scale with the baseline value. The dashed black line has a slope of 1. . . . .	84
5.8	An auroral absorption event. From the top, each panel represents: OMNI AE index, 5.382 MHz occurrence and their baselines, then riometer absorption at <i>talo</i> , <i>rank</i> , <i>chur</i> , <i>gill</i> and <i>isll</i> with dropout (calculated as baseline – occurrence) overplotted for the 5.382 MHz transmissions. Dawn to dusk at Alert are highlighted in yellow, times where AE was above 400 nT are highlighted in red. Gaps in riometer data signify the data are missing. . . . .	85
5.9	Probability Mass Function (PMF) and associated Cumulative Mass Function (CMF) of the distribution of dropouts for 5.382 MHz signal at each riometer absorption bin. The median is marked by a red cross, and is the absorption level below which (and above which) half of the dropouts occurred. Only the dropouts at the Minor class were considered. . . . .	86
5.10	The cumulative mass functions surface for the distribution of dropouts (z-axis and colorbar) at different levels as a function of riometer absorption (x-axis) at different sites (y-axis). The median for each distribution is shown as a red diamond. . . . .	87
5.11	Median absorption level at <i>chur</i> , <i>gill</i> , and <i>isll</i> as a function of frequency for different dropout levels. <i>chur</i> 's lines are opaque to indicate its missing 45% of the events' data. . . . .	89
5.12	Median absorption as a function of dropout level for 5.382 MHz for <i>chur</i> , <i>gill</i> , and <i>isll</i> . . . . .	89
6.1	Riometer on the path of the HF-link from OTTW to ALRT showing absorption at the time of signal enhancement. . . . .	92
6.2	Early observations of an AA event at an HSR in Gillam (GILL). The full spectrum data is shown on the left. The event occurs at about 15 UTC, as shown in the 30 MHz power plot on the right. . . . .	93
6.3	Zoomed in plots on parts of the spectrogram in Figure 6.2, showcasing the loss of the 5 MHz WWV/WWVH link (top left) and the 7.85 MHz CHU link (top right) in contrast with the enhancement of the WWV/WWVH link at 10 MHz (bottom left) and 15 MHz (bottom right). The CHU link at 14.67 MHz is also enhanced (bottom right). . . . .	93
6.4	Example showing HF enhancements at the 11.107 MHz band as shown in the HSR data (red) via the green markers, which shows reception during the time of the event. . . . .	94
6.5	Absorption vs. time for the same day (2 August 2021), showing receptions at 11.107 MHz as yellow dots, showcasing enhancement during the rise to the peak absorption level. . . . .	94
6.6	CHU signal absorption during the 2 August 2021 event. . . . .	95
6.7	Another, more sporadic, AA event on 3 February 2022. Data shown is from an HSR at MEAN, with the full spectrogram on the left and the 30 MHz signal power is shown on the right. Event onset is shown via the dashed black line. . . . .	96
6.8	The distribution of SNR for each pulse in the NRCan transmission schedule (active during the 3 February 2022 event) for the 5.382 MHz signal. The mean, $\mu$ , and standard deviation, $\sigma$ is highest for the 2 <sup>nd</sup> pulse from the Yellowknife transmitter. . . . .	96
6.9	Raw signal power at 30 MHz is shown in red with receptions from each transmitter superimposed on top. 14.3644 MHz transmissions are enhanced during the event, around 9 UTC. . . . .	97

B.1	Example of raw HSR data at various frequencies. Data is contaminated by interference (positive spikes in power level) and absorption (negative spikes in signal level). These noise sources evolve with time, with many factors at play. . . . .	126
B.2	An example of signal level taking multiple values as a function of time for specific frequency bins. . . . .	126
B.3	Example of raw signal taking a wave form, analogous to a carrier signal. . . . .	127
B.4	Example of low frequency ticks within the data. . . . .	127
B.5	Raw signal at various frequency bins around 30 MHz. Some bins, highlighted in red, exhibit the 'ticking' underlying signal. . . . .	128
B.6	The Kaiser window used to extract the 'ticking'. . . . .	129
B.7	Same as <b>Figure B.5</b> but the data is convolved with the Kaiser window in <b>Figure B.6</b> . . . . .	130
B.8	Same as <b>Figure B.7</b> , but the envelope of the data, without the ticking is shown in red. . . . .	130
B.9	An example of a heavily contaminated frequency bin. The same Kaiser window fails to detect any specific underlying signal that can be filtered. An FFT shows complicated harmonics. Zoomed-in versions of the FFT in both amplitude and frequency are included for illustration. . . . .	131
B.10	An example of noise bursts, lasting on the order of an hour. . . . .	132
B.11	The power distributions of the data from <b>Figure B.10</b> spanning 12–13, 13–14, 14–15 and 15–16 UTC, in that order. . . . .	132
B.12	A plot showcasing accuracy of the hourly distribution algorithm, where red highlights a noisy hour. . . . .	133
B.13	A screenshot taken from my manual baseliner application in its beta stages of development. . . . .	134
B.14	A mind map of the iterative baselining procedure. . . . .	135
B.15	A plot of signal level for the 28 <sup>th</sup> of February for data from PFRR, used to showcase the baselining procedure in action. The raw data is shown in red. Quiet data from the 7 previous days is used to generate the baseline, shown in red. From there, the algorithm starts detecting absorption, highlighted in light blue, and uses the hourly distribution algorithm to highlight interference (red). The hourly distribution sometimes (but not always) detects absorption, where the two colors overlap. . . . .	136
B.16	Example application of the iterative procedure to multiple days following the 28 <sup>th</sup> ( <b>Figure B.15</b> ), by taking the quiet time data (data at times void of noise or absorption) and binning them in sidereal time to generate a new QDC for the next day, iterating with each day. . . . .	136
B.17	A plot showing the manually generated baseline for 25 MHz. Raw data is shown in black and the QDC is shown in orange. . . . .	139
B.18	Same as <b>Figure B.17</b> but for 41 MHz. The deviation from the baseline is much higher! . . . . .	139

# List of Tables

2.1	Solar flares and their classification according to X-ray flux. . . . .	27
3.1	Site abbreviation code, location, and geodetic coordinates for HSRs used in this thesis. . . . .	40
3.2	GO-Canada riometer site abbreviation code, location, and geodetic coordinates. . . . .	42
3.3	NRCan network of transmitters and their receiver at Alert. Given are each instrument's site code, location and coordinates. . . . .	49
3.4	NRC's Transmitter site code, location, and coordinates. . . . .	52
3.5	NIST Trasnsmitter site codes, location and coordinates. . . . .	52
4.1	NRCan transmission schedule active during 5 March 2022. The transmission start times are staggered. Yellowknife (YKNF) is always ahead of Fort Churchill (FCHU), which is ahead of Ottawa (OTTW). This schedule starts at the beginning of each hour and repeats every 7.5 minutes (resulting in 8 cycles every hour). During this time OTTW was not transmitting at both 5.3820 and 6.9285 MHz. . . . .	57
4.2	Absorption distances at 55-, 65-, 75-, 85-, and 95-km altitudes for every Transmitter-HSR link investigated for this event. The average difference is the mean of the differences between absorption distances at the chosen altitudes (e.g., the mean of 40, 38, 37 and 38 km for the WWV-MEDO link at 15 MHz). The range is the maximum minus the minimum of those distances. . . . .	65
5.1	Maximum Occurrence Look-up Table. The number of maximum transmissions at a given frequency is displayed for each year. Years missing imply no data. Only 5.382 and 10.4220 MHz transmissions are affected by some operational change sometime after 2014, going from 4 to 8 maximum transmissions. . . . .	77
5.2	Information entropy of the hour of day, $S(H)$ , occurrences in the hour, $S(O)$ , as well as their joint entropy, $S(H, O)$ , and mutual information shared between the two, $I(H, O)$ . . . . .	79
5.3	Ordinal categorization of the dropout level as a function of dropouts. . . . .	86
5.4	Analysis of Variance (ANOVA) for riometer measurements at different dropout levels at 5.382 MHz. Shown are the F-statistic, associated p-value, and the number of samples, $n$ , for each riometer. . . . .	88

# List of Symbols, Abbreviations, and Nomenclature

## Symbols

$A$	Absorption
$B$	Baseline occurrences
$B_N$	Normalized baseline occurrences
$c$	Speed of light in vacuum
$D$	Dropouts
$D_N$	Normalized dropouts
$\vec{D}$	Displacement Vector
$e$	Fundamental charge
$\epsilon$	Permittivity of the medium
$\epsilon_0$	Permittivity of free space
$\epsilon_r$	Dielectric constant
$f$	Frequency of the radiowave
$f_p$	Plasma oscillation frequency
$\vec{E}$	Electric Field
$h'$	Virtual height
$H$	Hour of the day in coordinated universal time
$I(X, Y)$	Mutual information of two variables $X$ and $Y$
$\chi$	Imaginary part of index of refraction
$k$	Real part of wave vector
$\vec{k}$	Wave vector

$\mathcal{K}$	Absorption Coefficient
$m_e$	Mass of the electron
$n$	Index of refraction
$N_e$	Charge per unit volume
$\nu$	Effective Collision Frequency
$O$	Occurrences (number of signal receptions in an hour)
$O_N$	Normalized occurrences
$\vec{P}$	Polarization vector
$\vec{p}$	Electric dipole moment
$R$	Ground Range
$S(X)$	Information entropy of some variable $X$
$S(X, Y)$	Joint entropy of two variables $X$ and $Y$
$\sigma_b$	Bound surface charge per unit area
$\vec{r}$	Distance from equilibrium position
$\vec{B}$	Geomagnetic Field
$\eta$	Real part of index of refraction
$X$	Electric Susceptibility
$\omega$	Angular frequency of the radiowave
$\omega_c$	Electron gyrofrequency
$\omega_p$	Angular plasma oscillation frequency

## Abbreviations

AA	Auroral Absorption
AE	Auroral Electrojet
CNA	Cosmic Noise Absorption
CMF	Cumulative Mass Function
FOV	Field of View
GO	Geospace Observatory
GOES	Geostationary Satellite
HSR	Hyper Spectral Riometer
HF	High Frequency, (3–30 MHz)
IRI	International Reference Ionosphere

LUF	Least Usable Frequency
MLT	Magnetic Local Time
MUF	Maximum Usable Frequency
NRC	National Research Council
NRCan	Natural Resources Canada
NIST	National Institute of Standards and Technology
O-mode	Ordinary Mode Ray
PCA	Polar Cap Absorption
PMF	Probability Mass Function
QDC	Quiet Day Curve
Riometer	Relative Ionospheric Opacity Meter for Extra-terrestrial Radiation
SNR	Signal-to-Noise Ratio
SWAN	Space Weather Adaptive Network
SWF	Short Wave Fadeout
SWPC	Space Weather Prediction Center
UTC	Coordinated Universal Time
VHF	Very High Frequency
X-mode	Extraordinary Mode Ray
XRF	X-ray Flux

# Epigraph

*Chance favors the prepared mind.*

- Louis Pasteur

# Chapter 1

## Introduction

### 1.1 Space Weather

Space weather is a sub-field within space physics concerned with geospace processes that can impact human activities and technologies. It encompasses the dynamic interactions between solar processes, Earth's magnetic field, and the Earth's upper atmosphere. Space weather phenomena can significantly impact technologies such as satellites, communication systems, and power grids on Earth (e.g., Grant et al., 2012; Ruck & Themens, 2021; Uryadov et al., 2018). For example, induced currents during large geomagnetic storms can severely impact power grids, as was seen in the Quebec blackout of 1989 (Boteler, 2019). Such events highlight the technical challenges within our modern world and the connections to the dynamics of our space environment.

#### 1.1.1 Solar Radiation

Ultimately, space weather is driven by the Sun, which is constantly expelling plasma, or ionized gas called the **Solar Wind**, in addition to emitting radiation towards Earth. The constant radiation ionizes the Earth's upper atmosphere, called the **Ionosphere**. The dynamics on the Sun dictate the dynamics of the solar wind and the emitted radiation's spectrum and intensity.

The Sun-facing side of the ionosphere is sometimes exposed to more active regions of the Sun. These regions may abruptly release bursts of radiation over a wide band of wavelengths, from radio to X-rays (Davies, 1990), which enhances ionization in the day-side ionosphere. Figure 1.1 shows an illustration of the Earth's ionosphere reacting to the burst of radiation, referred to as a **Solar Flare**. After  $\sim 8$  minutes— the

time it takes for light to reach the Earth, the burst of radiation will further ionize the upper atmosphere, which can impact radio communication systems. The figure emphasizes the impact on over-the-horizon systems (though other radio systems are also affected), which rely on the ionosphere, in this case acting like a mirror, for radiowave propagation.

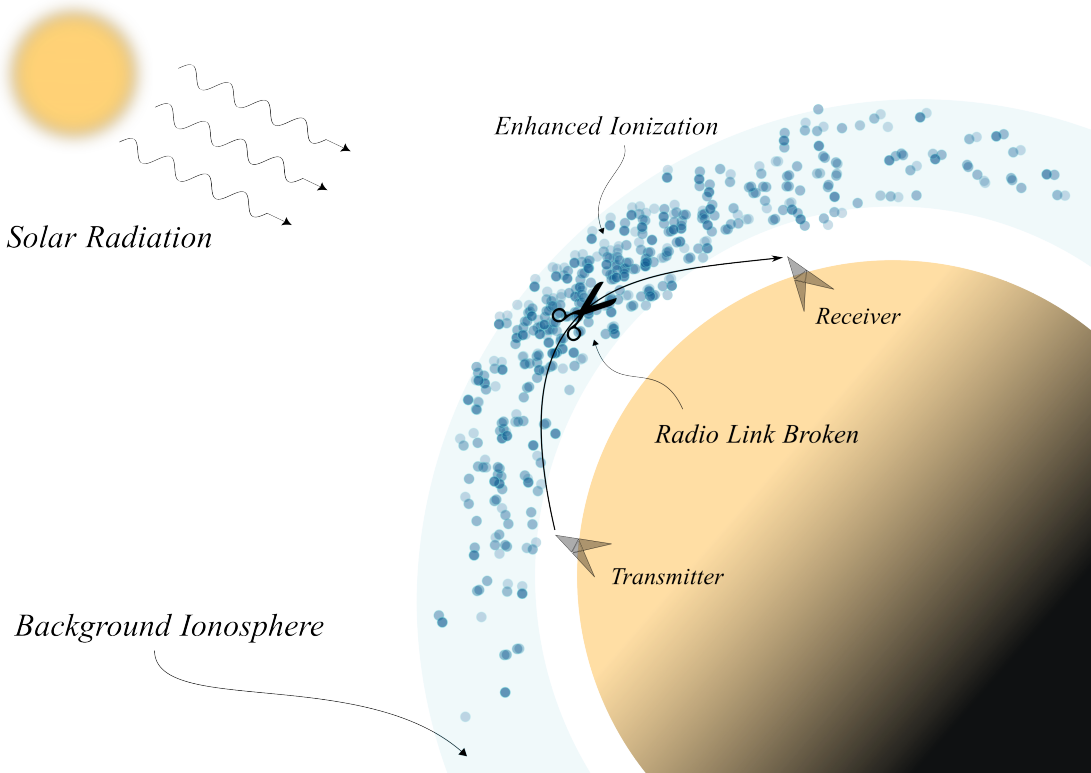


Figure 1.1: Illustration of the day-side ionosphere exposed to a solar flare. A flare increases the ionization on the day-side, with more electron density closer to the subsolar point. Radiowaves passing through these enhanced regions lose their energy and fail to propagate further.

### 1.1.2 Energetic Particle Precipitation

Besides radiation, the ejected magnetized plasma from the Sun (the solar wind) will interact with Earth's magnetic field. As a consequence, the intrinsically dipolar field of the Earth is compressed on the day side and stretched out on the night side, as illustrated in Figure 1.2. This cavity, which stretches hundreds of Earth radii away, is referred to as the ***Magnetosphere***, which deflects charged particles from directly entering the Earth's atmosphere.

Through the solar wind, the sun provides a constant and variable source of energy and particles to the magnetosphere. Energetic electrons, when allowed to penetrate the deepest layers of the ionosphere cause

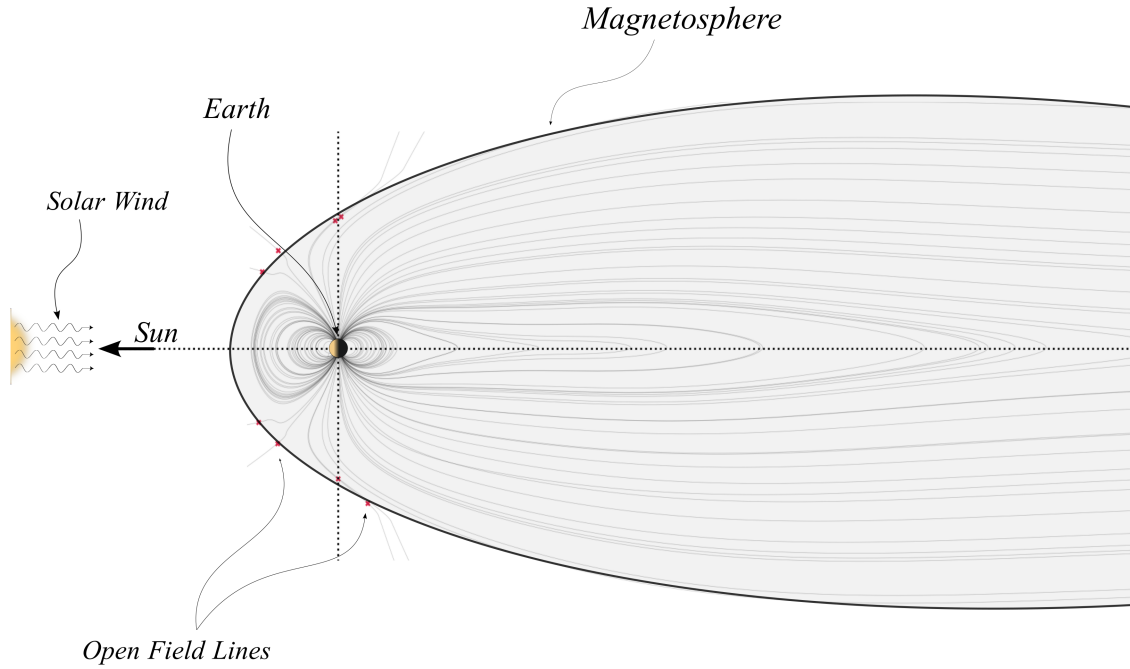


Figure 1.2: Illustration of Earth’s magnetosphere. Open field lines (ones which connect directly to the interplanetary medium) have a red marker attached to them. I use the Tsyganenko model (Tsyganenko & Stern, 1996) for the magnetic field lines.

ionization, which leads to radiowave absorption. The same can be said for protons. During some large solar flares, the Sun may eject energetic protons, which travel down the open field lines shown in Figure 1.2 and into the polar ionosphere, causing radio blackouts in those regions.

## 1.2 Research Goals

During space weather events, such as solar flares or energetic particle precipitation, the enhanced ionization in the ionosphere impacts radio systems. Investigation of these space weather phenomena via their impact on radio wave propagation is at the heart of my thesis research. Therefore, I will further explain the mechanism by which radiowaves are impacted as we progress through Chapters 2 and 3. For now, I describe my goals with this research and how they relate to the impact of space weather on radio systems.

### **1.2.1 Modelling the Spatial Extent of Regions of Enhanced Electron Density**

The first goal of this thesis is to develop a methodology for remote sensing the area impacted by enhanced ionization. This goal is of high importance to the scientific community and various industries. First, during precipitation events, regions of enhanced electron density are commensurable with the precipitation area of energetic particles, originating in the magnetosphere. The ability to track these spatial boundaries in the ionosphere corresponds to boundaries in the magnetosphere—such information is valuable for studies involving precipitation mechanisms and dynamics.

Additionally, enhanced ionization regions correspond to radio signal loss regions. These regions are of critical importance to radio communication and navigation systems. Such regions, which are byproducts of ionospheric disturbances, present hazards for industries such as aviation and maritime (see e.g., Grant et al., 2012; Neal et al., 2013; Pirjola et al., 2005). My research aims to contribute to the understanding of such hazards by providing information about the spatial extent of these regions in the ionosphere.

### **1.2.2 Developing a Threshold Riometer Absorption**

The second goal of this thesis is to contribute to the development of an alerting system with Natural Resources Canada’s (NRCan) Magnetic Observatory—the Canadian Space Weather Forecasting Center, which is concerned with the aforementioned hazards. Daily, the observatory monitors space weather using instruments to provide alerts for various industries based on prevailing space weather conditions, probability, and severity of impact. I aim to add one more instrument to their list, the RIOMETER (Relative Ionospheric Opacity Meter for Extra-terrestrial Radiation)—described later in Section 3.2; this is the central instrument of my thesis, and provides extensive information about radio signal loss. I aim to use riometers to provide a threshold which can be used to contribute to nowcast frameworks, providing alerts for when energetic electron precipitation is taking place. The results found in my research have potential implications for all high-latitude radio systems, where these precipitation events often occur.

## **1.3 Outline of Thesis**

The thesis is divided such that in Chapter 2, I explain all the sufficient background needed to understand how geomagnetic and solar events impact radiowave propagation in Earth’s ionosphere. In Chapter 3, I discuss the instrumentation used, how it works, and the signature of geophysical disturbances as observed in the data. In Chapter 4, I summarize the work done in (Ghaly et al., 2024), which utilizes new, prototype instruments to

develop a methodology for remote sensing the spatial extent of the region impacted by space weather events. In Chapter 5, I introduce my work in collaboration with NRCan on using the instruments introduced in **3.2** to develop alerting thresholds for the space weather phenomenon known as Auroral Absorption, introduced in Section 2.4.3. Finally, I conclude with some remarks and discuss future work in Chapter 6.

# Chapter 2

## Theory and Background

The goal of this thesis is to use new, prototype instruments to resolve the spatial structure of electron density enhancements as well as to study the impact of those enhancements on HF communications. This chapter is intended to provide the background information sufficient to support the analysis methods and conclusions.

### 2.1 Radiowave Propagation in The Ionosphere

An understanding of the ionospheric medium is required to begin any analysis on radiowave propagation. Here, I introduce the ionosphere and its nomenclature, describe its dispersive properties, then expand on this knowledge to contextualize radiowave attenuation and its relation to electron density enhancements—the latter being the main focus of this thesis.

I note that many terms used to describe the HF propagation environment are standard terminology used in the field. As such, a supplemental appendix has been provided to aid the reader. See **Appendix C**.

#### 2.1.1 Ionospheric Layers

As the sun rises on the dayside atmosphere, radiation of various wavelengths (mainly in the Ultra Violet and Extreme Ultra Violet) will ionize the neutral constituents, resulting in the ionosphere: the ionized region of the upper atmosphere, spanning  $\sim 70 - 1000$  km altitude. An example electron density profile simulated using the International Reference Ionosphere (IRI) 2016 model (Bilitza et al., 2017) is shown in Figure 2.1, where the electron density as a function of height has been simulated for both local noon and midnight for a given location. The loss of ionization rates during the night lowers the electron density.

The ionosphere is divided into layers according to the peaks in electron density. The highest electron density peak occurs between 200 – 400 km altitude, referred to as the ***F Region*** peak. Below, around  $\sim$  100 km is another peak in electron density, marking the ***E Region*** ionosphere, extending from 90 – 150 km, where visible aurora typically takes place. The lowermost region, typically considered to be below  $\sim$  90 km altitude is the ***D Region***.

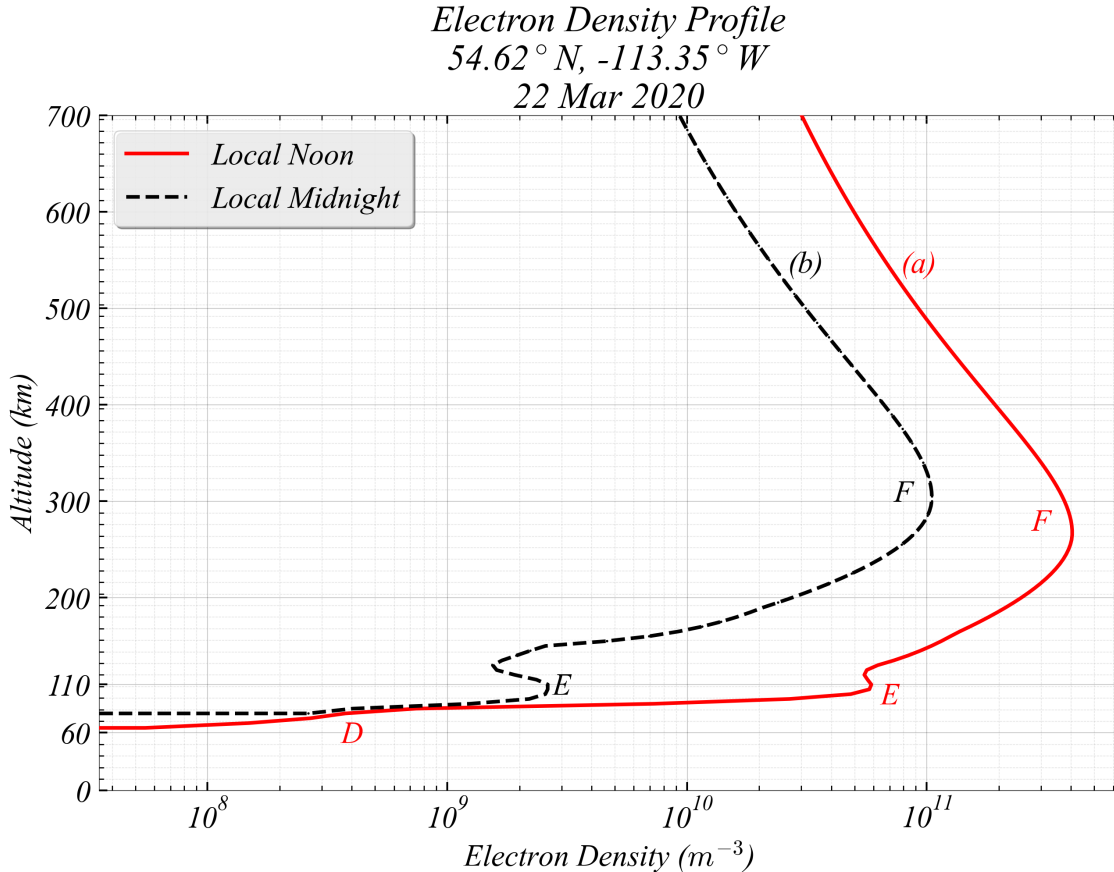


Figure 2.1: Example electron density profiles for the (a) daytime ionosphere, and (b) the nighttime ionosphere. This simulation of electron density is obtained using the International Reference Ionosphere (IRI) model of 2016.

When the sun sets, the ionization subsides and recombination dominates. As a result, the D-region, having relatively low electron density, and relatively high neutral density, disappears, and the ionosphere is reconfigured to have a profile similar to that shown in Figure 2.1 (b). The D-region is crucial to this thesis because it is the primary site for radiowave attenuation, as I will explain further in Section 2.2.

### 2.1.2 Magnetoionic Theory

Most textbooks start the discussion of radiowave propagation in the ionosphere by reviewing magnetoionic theory— the study of electromagnetic wave propagation through a magnetized, ionized medium. A standard treatment derives an equation given by Appleton and Hartree (Budden, 1985). While I offer a full derivation in **Appendix A.5**, in the following sections, I shall build up the elements needed to understand the significance of this equation. The following brief description of this equation should be used only as a reference and an outline. The derivations start in the next section (2.1.3).

The Appleton-Hartree equation reads

$$n^2 = 1 - \frac{X}{U - \frac{Y_T^2}{2(U-X)} \pm \sqrt{\frac{Y_T^4}{4(U-X)} + Y_L^2}}, \quad (2.1)$$

where  $n$  is the index of refraction, and the different terms are

$$X = \frac{\omega_p^2}{\omega^2}, \quad (2.2)$$

$$\omega_p^2 = \frac{N_e e^2}{m_e \epsilon_0}, \quad (2.3)$$

$$U = 1 - iZ, \quad (2.4)$$

$$Z = \frac{\nu}{\omega}, \quad (2.5)$$

$$Y_T = \frac{\omega_c}{\omega} \sin \theta, \quad (2.6)$$

$$Y_L = \frac{\omega_c}{\omega} \cos \theta, \quad (2.7)$$

$$\omega_c = \frac{e \|\vec{B}\|}{m_e}. \quad (2.8)$$

The first term,  $X$ , is the square of ratio of the angular rate of oscillations of the electrons in the ionospheric medium,  $\omega_p$ , to the angular frequency of the propagating radiowave,  $\omega$ . I shall derive both  $X$  and  $\omega_p$  in the following section (2.1.3). Then I shall introduce collisions in Section 2.2. The collision frequency of the electrons is denoted by  $\nu$ , which appears in the  $Z$  and thus the  $U$  terms. Finally, in Section 2.3, I will discuss the implications of Earth's magnetic field,  $\vec{B}$ , and the significance of the  $Y_T$  and  $Y_L$  terms, which are the ratios of the gyrofrequency,  $\omega_c$ , to the angular frequency of the radiowave, in the transverse and longitudinal directions with respect to the geomagnetic field. These directions are denoted by the  $\sin \theta$  and  $\cos \theta$  terms, respectively, where  $\theta$  is the angle between the direction of wave propagation and the geomagnetic field.

I shall focus on some limiting cases to build up the necessary knowledge for the propagation phenomena relevant to my research. In Section 2.1.3, I will ignore the effects of Earth's magnetic field as well as collisions, hence,  $Z = 0$ ,  $U = 1$ , and  $Y_T = Y_L = 0$ , to obtain

$$\boxed{n^2 = 1 - X = 1 - \frac{\omega_p^2}{\omega^2}}. \quad (2.9)$$

This simple result implies a cutoff threshold for which radiowaves with frequencies lower than the cutoff can no longer penetrate the ionosphere. This result holds even when collisions and Earth's magnetic field are incorporated.

In Section 2.2, I incorporate collisions into the analysis but not the geomagnetic field, such that  $Y_T = Y_L = 0$  but  $U = 1 - iZ$ , and

$$\boxed{n^2 = 1 - \frac{X}{U} = 1 - \frac{\omega_p^2}{\omega^2 \left(1 - i\frac{\nu}{\omega}\right)}}, \quad (2.10)$$

where, now, the imaginary term implies that besides refraction, there is attenuation of the radiowave as it propagates through the medium. Thus collisions act as frictional forces, impeding the propagation of the wave.

Finally, I discuss some implications of the full Appleton-Hartree equation in Section 2.3. Specifically, I focus on the condition where  $\theta \approx 0^\circ$ , where  $Y_T = 0$ , and we have

$$\boxed{n^2 = 1 - \frac{X}{U \pm Y_L}}. \quad (2.11)$$

This condition is highly relevant for my research since the radio receivers employed in my analysis are situated at high latitudes where, for the radiowaves considered,  $\theta \approx 0^\circ$ .

### 2.1.3 Dispersion Relation

Being partially ionized, the ionosphere can be viewed as a dielectric. This medium will allow for electromagnetic wave propagation, with varying propagation properties for different wave frequencies, analogous to a prism – a phenomenon known as dispersion. The following section details the dispersive properties of the ionospheric medium.

## Dielectric Medium

For the moment, let us ignore the effects of frictional forces and Earth's magnetic field on the propagation of radio waves. We shall include such effects later in Sections 2.2 and 2.3, respectively. This discussion regards the free electrons as the main wave propagators, since the ions are much heavier. An electron bound between ions starts oscillating, much like a spring, if displaced from its equilibrium position.

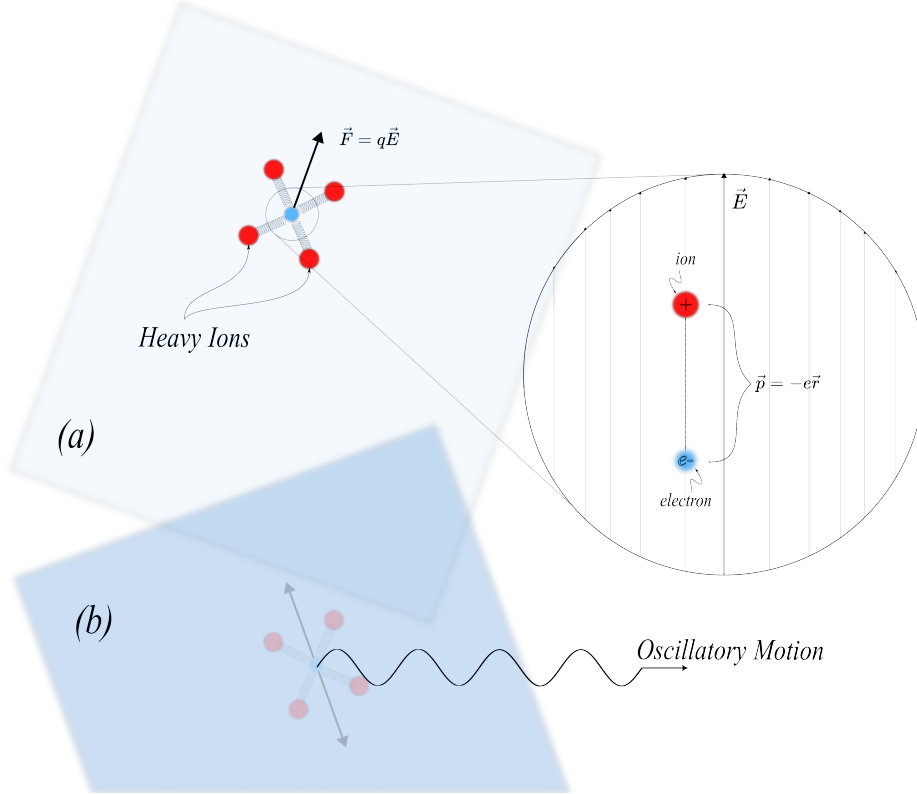


Figure 2.2: The electrons are bound to the relatively stationary ions. Any electrostatic disturbance (a) polarizes the medium, and leads to an oscillatory motion (b).

To characterize the motion of the electrons, consider a thin layer of the plasma, where the electron is bound to the heavy ions, as in Figure 2.2. An electrostatic force would polarize the medium (by disrupting the distribution of electrons relative to the ions), thus inducing electric dipole moments,

$$\vec{p} = -e\vec{r},$$

where  $e$  is the fundamental charge and  $\vec{r}$  is the separation distance. The net polarization,  $\vec{P}$ , is the sum of all those dipole moments. Assuming quasi-neutrality,

$$\vec{P} = -N_e e \vec{r}, \quad (2.12)$$

where there are  $N_e$  charge pairs per unit volume, polarized some distance  $r$ , perpendicular to the surface of the sheet. Therefore, the charge per unit area,  $\sigma_b$ , over the sheet is equal to the magnitude of the polarization:

$$\sigma_b = \|\vec{P}\| = -N_e e r. \quad (2.13)$$

This separation must be proportional to the electric field,  $E$ , causing it, and one can show that the field takes the form

$$E = -\frac{\sigma_b}{\epsilon_0},$$

where  $\epsilon_0$  is the permittivity of free space. For a rigorous derivation, see **Appendix A.1**. In turn, the polarization must be proportional to the electric field. The constant of proportionality is referred to as the electric susceptibility (sometimes called the polarizability),  $X$ , and

$$\vec{P} = -\epsilon_0 X \vec{E}. \quad (2.14)$$

Deriving the susceptibility will enable us to deduce the properties of the dielectric medium.

### Plasma Oscillation

To find a relation between the electronic polarization and the electric field, consider the Lorentz force law on an electron,

$$m_e \frac{\partial^2 \vec{r}}{\partial t^2} = -e \vec{E} = -\frac{N_e e^2}{\epsilon_0} \vec{r}, \quad (2.15)$$

where  $m_e$  is the mass of the electron. Rearranging, we retrieve a second-order partial differential equation of motion:

$$\frac{\partial^2 \vec{r}}{\partial t^2} = -\frac{N_e e^2}{m_e \epsilon_0} \vec{r}.$$

This motion is an oscillation, with angular frequency (just as in equation 2.3),

$$\boxed{\omega_p^2 = \frac{N_e e^2}{m_e \epsilon_0}}$$

called the **Plasma Frequency**. Thus, any perturbations from the equilibrium position,  $\vec{r}$ , will cause the electron to oscillate harmonically at an angular frequency,  $\omega_p$ . This frequency is crucial in determining the reflective and refractive properties of the ionospheric medium for radio-waves propagating through it, as it signifies the natural mode of oscillation for the electrons in the medium. As I shall describe, the plasma

oscillation frequency serves as a critical cutoff for radiowaves with frequencies  $\omega < \omega_p$ . This dispersive behavior is key to understanding how radiowaves propagate to the radio receivers used in this study. Below, I shall quantitatively describe how these plasma oscillations, which are purely a function of electron density, give rise to three propagation modes highly relevant to my research.

## Index of Refraction

Driving the electron motion with a radio wave transiting that region of plasma will excite the electrons to oscillate at the same frequency of the wave ( $\omega$ ), and the electric field,  $\vec{E}$ , in equation 2.15 becomes the total field. Since the resulting oscillation, in practice, cannot be sustained indefinitely due to collisions, as explained in the following section (2.2), we shall manually impose this transience condition here, allowing us to employ the Fourier Trick (see **Appendix A.3** for a detailed explanation), where  $\frac{\partial}{\partial t} \rightarrow i\omega$ , in solving the differential equation of motion. Equation 2.15 now reads

$$\begin{aligned}\frac{\partial^2 \vec{r}}{\partial t^2} &= -\frac{e}{m_e} \vec{E} \\ i^2 \omega^2 \vec{r} &= -\frac{e}{m_e} \vec{E} \\ \vec{r} &= \frac{e}{m_e \omega^2} \vec{E},\end{aligned}$$

and we arrive at a relationship between the electric field and the displacement from equilibrium,  $\vec{r}$ . Multiplying by  $\frac{N_e e}{\epsilon_0}$  and substituting for the plasma frequency and polarization vector (equations 2.3 and 2.12), we get

$$\begin{aligned}\frac{N_e e}{\epsilon_0} \vec{r} &= \frac{N_e e^2}{\epsilon_0 m_e \omega^2} \vec{E} \\ \vec{P} &= -\epsilon_0 \frac{\omega_p^2}{\omega^2} \vec{E},\end{aligned}$$

where, now, the electric susceptibility is that described in equation 2.2:

$$X = \frac{\omega_p^2}{\omega^2}.$$

From here we can use the displacement vector,  $\vec{D}$ , where

$$\vec{D} = \epsilon \vec{E} = \epsilon_0 \vec{E} + \vec{P}, \quad (2.16)$$

to solve for the electric permittivity or dielectric constant,  $\epsilon_r$ , which encodes the properties of the medium, and is defined as the ratio of the permittivity of the medium,  $\epsilon$ , to that of free space:

$$\epsilon_r = \frac{\epsilon}{\epsilon_0}. \quad (2.17)$$

Using equation 2.16, we can write

$$\epsilon_r \epsilon_0 \vec{E} = \epsilon_0 \vec{E} - \epsilon_0 X \vec{E}$$

$$\epsilon_r = 1 - X.$$

Since the index of refraction,  $n$ , is given by the square root of the dielectric constant,  $n = \sqrt{\epsilon_r}$ , this leads to the dispersion relation given in equation 2.9

$$n^2 = \epsilon_r = 1 - \frac{\omega_p^2}{\omega^2},$$

This result highlights the dispersive properties of the medium: lower frequency radiowaves exhibit more refraction and radiowaves with frequencies below the plasma frequency have an imaginary index of refraction, and thus cannot propagate their energy into the medium. Three propagation modes arise from this relation. I discuss them below as they form the basics for radiowave propagation in the ionosphere, which are needed to interpret the results in later sections and chapters.

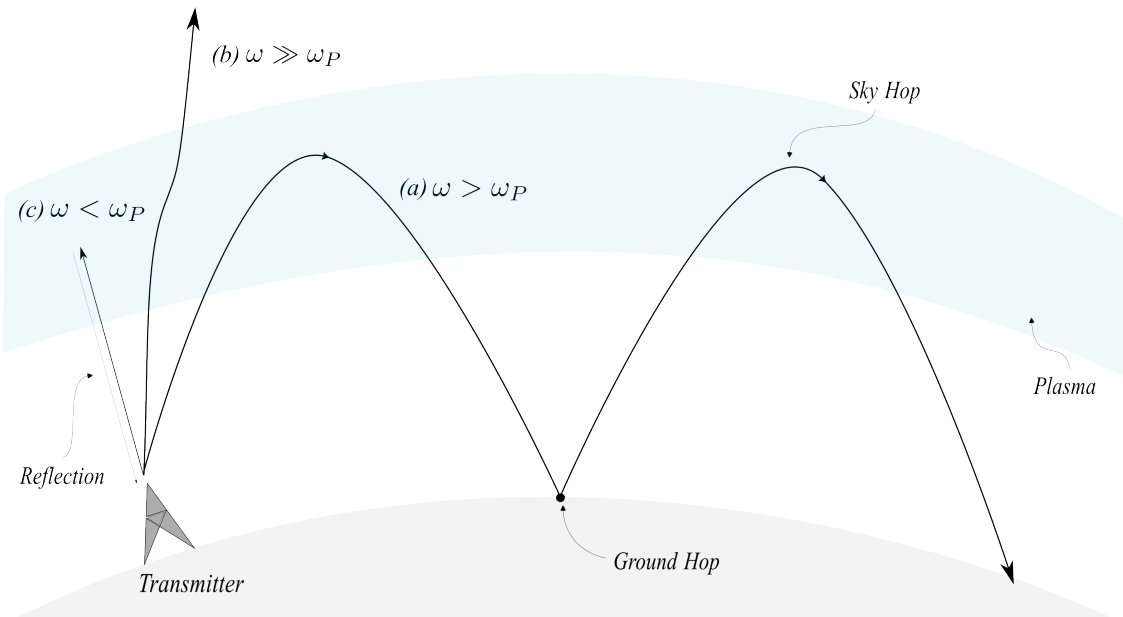


Figure 2.3: Illustration of (a) skywave- and (b) transionospheric- propagation, and (c) evanescent waves.

## 1. Total Internal Reflection

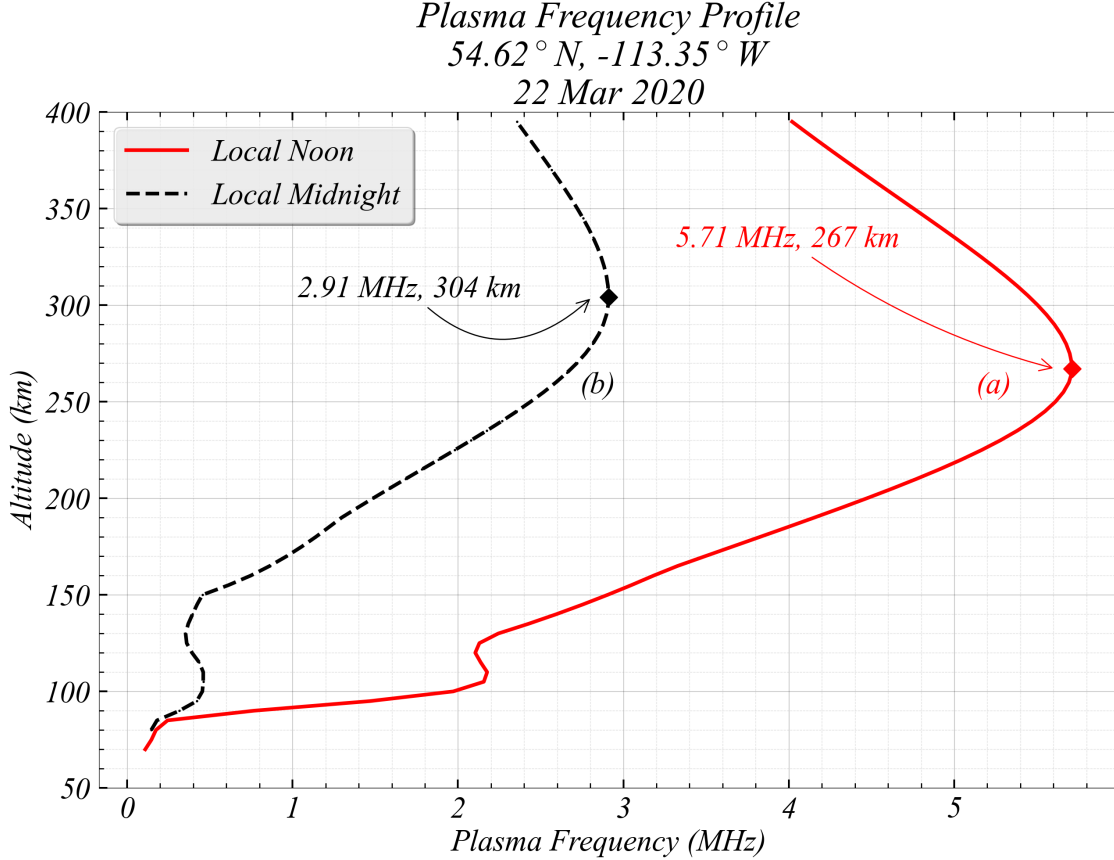


Figure 2.4: The plasma frequency profiles derived from the electron density profiles in Figure 2.1. The maximum frequencies correspond to the peak electron densities, which occurs in the F-region.

For radio frequencies less than the plasma frequency,  $\omega < \omega_p$ , the index of refraction, and thus the wave vector, are purely imaginary. In such cases, the wave's energy does not propagate through the material. These waves are evanescent and exhibit total internal reflection (see [Appendix A.2](#) for more details). Such a wave, if sent vertically upward, will be reflected back as in Figure 2.3 (c). Consequently, there is a lower limit on what frequencies can propagate through the ionosphere imposed by the plasma frequency.

Therefore, the ionosphere mirrors back waves with frequencies  $\omega < \omega_p$ . If, for instance, a radiowave with frequency  $f = \frac{\omega}{2\pi} = 1$  MHz were to approach the simulated ionosphere in Figure 2.1 (either at noon or midnight) on 22 Mar 2020 from outer space, its energy would not penetrate through. This reflection happens because the peak electron density of the profiles showed in Figure 2.1, which occur at the F-layer, correspond to plasma frequencies ( $f_p = \frac{\omega_p}{2\pi}$ ) of 5.71 MHz and 2.91 MHz for local noon and midnight, respectively—both higher than 1 MHz. The plasma frequency profiles calculated from the electron density profiles for the same

day are shown in Figure 2.4. For local noon, waves with  $f < 5.71$  MHz from extraterrestrial sources above  $\sim 270$  km are reflected back. For this reason, the peak plasma frequency is known as the critical or penetration frequency of the ionosphere. I shall refer to this result later in Section 3.2, when discussing cosmic signals in relation to the operation of the instruments used in this study.

Total internal reflection also models the mechanism by which a wave, incident at an oblique angle relative to the ionosphere, can exhibit multiple successive refractions that it bends back towards Earth. This propagation mode is referred to as ***Skywave*** and is described below.

## 2. Skywave Propagation

Skywave propagation is a mode by which terrestrial transmitters can send signals over the horizon, covering huge distances further than would be possible via line-of-sight propagation. The frequency band for skywave propagation is in the HF range, covering some of the upper-end medium frequencies ( $\sim 2\text{--}30$  MHz) (see e.g., Hunsucker & Hargreaves, 2003). Such signals from various transmitters in Canada and the United States are utilized in this research. These transmitters will be introduced in Section 3.3 and their utilization will be discussed in Chapters 4 and 5.

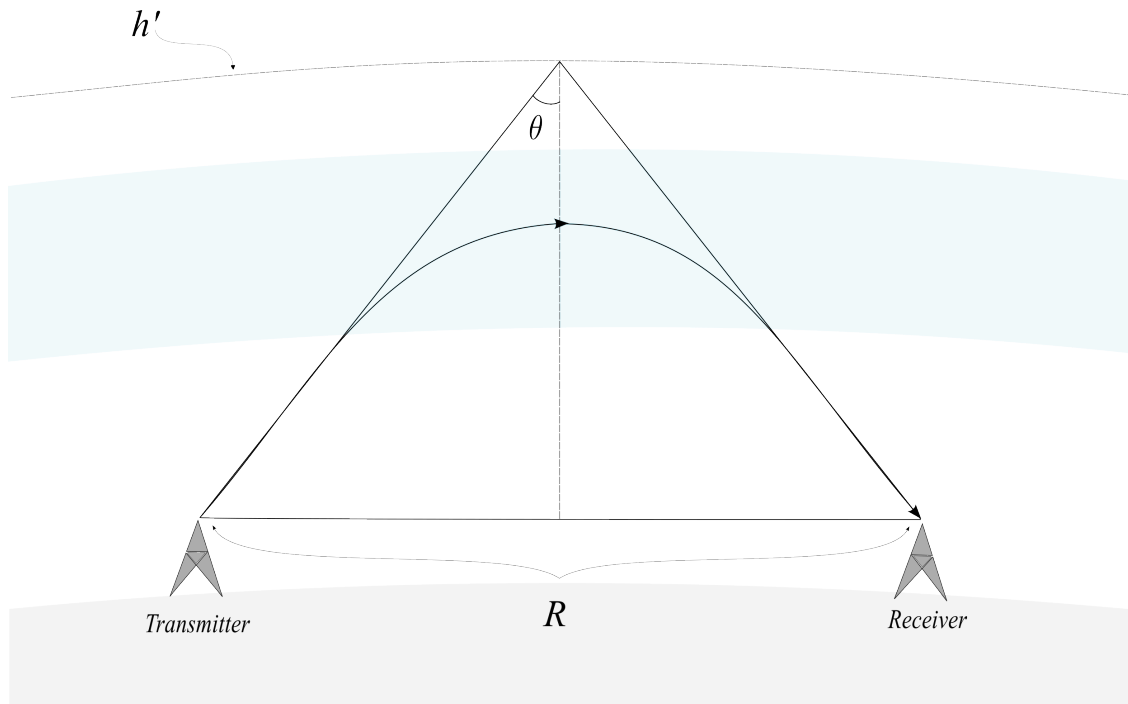


Figure 2.5: A plane ionosphere can be illustrated as a mirror, where the wave, incident at an angle  $\theta$  will reflect at some virtual height  $h'$ , covering a ground range distance  $D$ .

At first glance, equation 2.9 implies radio waves with frequencies above the plasma frequency are refracted. The degree of refraction varies with altitude, as per the variation in electron density profile, or, alternatively, the plasma frequency,  $f_p$ . Successive refraction may cause the signal to revert direction Earthward, effectively “hopping” between the Earth and the ionosphere, as illustrated in Figure 2.3 (a). A wave incident at an oblique angle on the ionosphere must have a sufficiently high frequency to successively bend enough, eventually reaching the critical angle necessary for total internal reflection (described in more detail in **Appendix A.2.2**). Using Snell’s law, for successive refractions, we can write this condition as

$$n_i \sin(\theta_i) = n_2 \sin(\theta_2) = \dots = n_c \sin(\theta_c), \quad (2.18)$$

where the angles between the ionospheric layers and their respective surface normals are denoted by  $\{\theta_i, \theta_2, \dots, \theta_c\}$  for layers with indices of refraction going from the initial layer,  $n_i$ , to the critical layer,  $n_c$ , where total internal reflection occurs and  $\theta_c = 90^\circ$ . Since the wave enters from the neutral atmosphere,  $n_i = 1$ , it follows that

$$\sin^2(\theta_i) = n_c^2.$$

Using the trigonometric identity and substituting for the dispersion relation (equation 2.9), we get

$$1 - \cos^2(\theta_i) = 1 - \left(\frac{\omega_p}{\omega}\right)^2 = 1 - \left(\frac{f_p}{f}\right)^2,$$

where  $f$  is the frequency of the radio wave, and  $f_p$  is the plasma frequency, as defined above. Therefore, besides the condition for normal incidence discussed above, for an obliquely incident wave to reflect back towards Earth (propagating via skywave), it must have an even higher frequency than that of the plasma, scaling with the angle of incidence as

$$f = f_p \sec(\theta_i). \quad (2.19)$$

The geometry of the situation is illustrated in Figure 2.5. Successive refractions can be modelled via a mirror ionosphere, where the virtual reflection height is denoted by  $h'$ . The ground distance covered for a wave incident at an angle  $\theta$  is denoted by  $R$ . The secant of the angle  $\theta$  can be rewritten so that equation 2.19 now reads

$$f = f_p \sqrt{1 + \left(\frac{R}{2h'}\right)^2}. \quad (2.20)$$

Figure 2.6 shows the frequency needed for skywave propagation for various angles of oblique incidence and plasma frequencies. The higher the angle of incidence, the higher the frequency required for reflection off the same ionospheric layer. For example, at  $60^\circ$ ,  $\csc(60^\circ) = 2$ , and double the plasma frequency will result

in reflection. This result implies that waves of higher frequencies, incident at higher angles, can be used to establish HF links between two fixed locations.

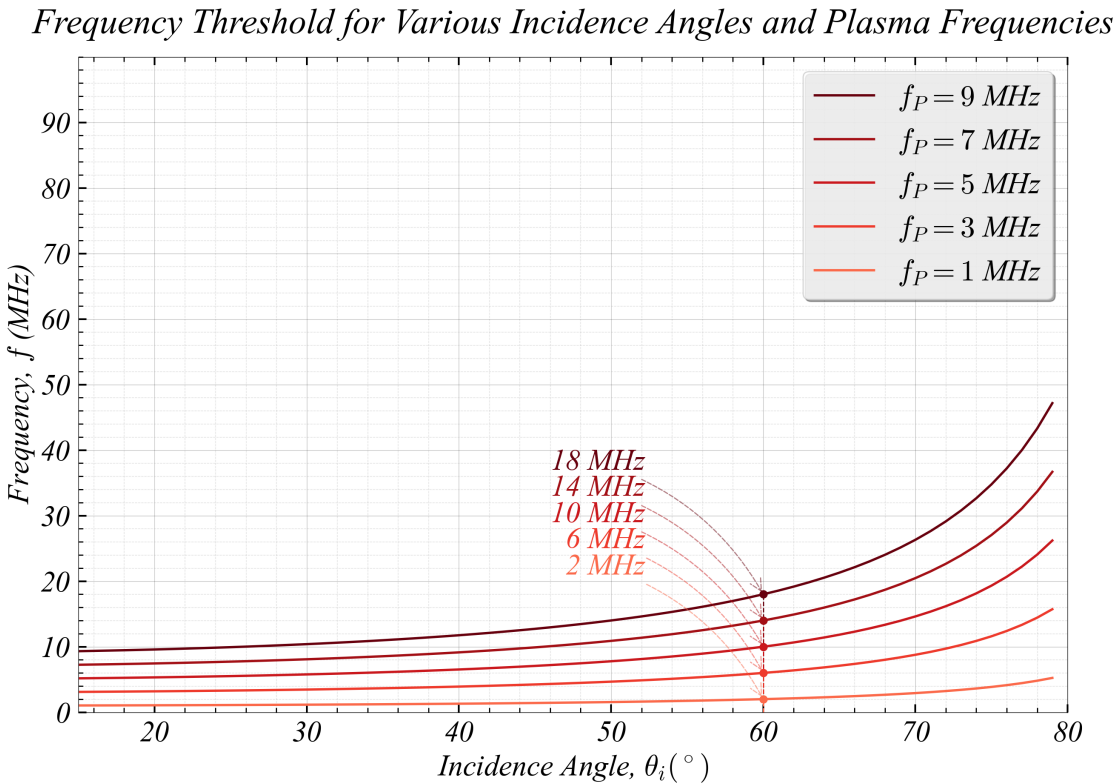


Figure 2.6: A wave reflecting off a layer with frequency  $f_p$  will have to have a higher frequency if it were incident at the same layer but via a higher incidence angle.

In practice, there is an upper limit on the angle of incidence, given by the lower limit on the height of the critical layer the wave is reflecting off of. This will in turn dictate the highest frequency that can be used to establish a link between two locations, known as the ***Maximum Usable Frequency*** (MUF). For example, employing the plasma profile used in Figure 2.4, and focusing only on the region above 150 km altitude, one can derive the ground distance covered by signals of different frequencies incident at different angles, such as shown in Figure 2.7.

For two HF radios, separated by 2000 km, several frequencies can establish a link. However, the 23.5 MHz signal sets the threshold for the MUF. Any alteration to the plasma frequency profile, which is a function of the ionospheric electron density, as induced by space weather events, will thus alter the MUF. I shall employ this fact later in Chapter 5.

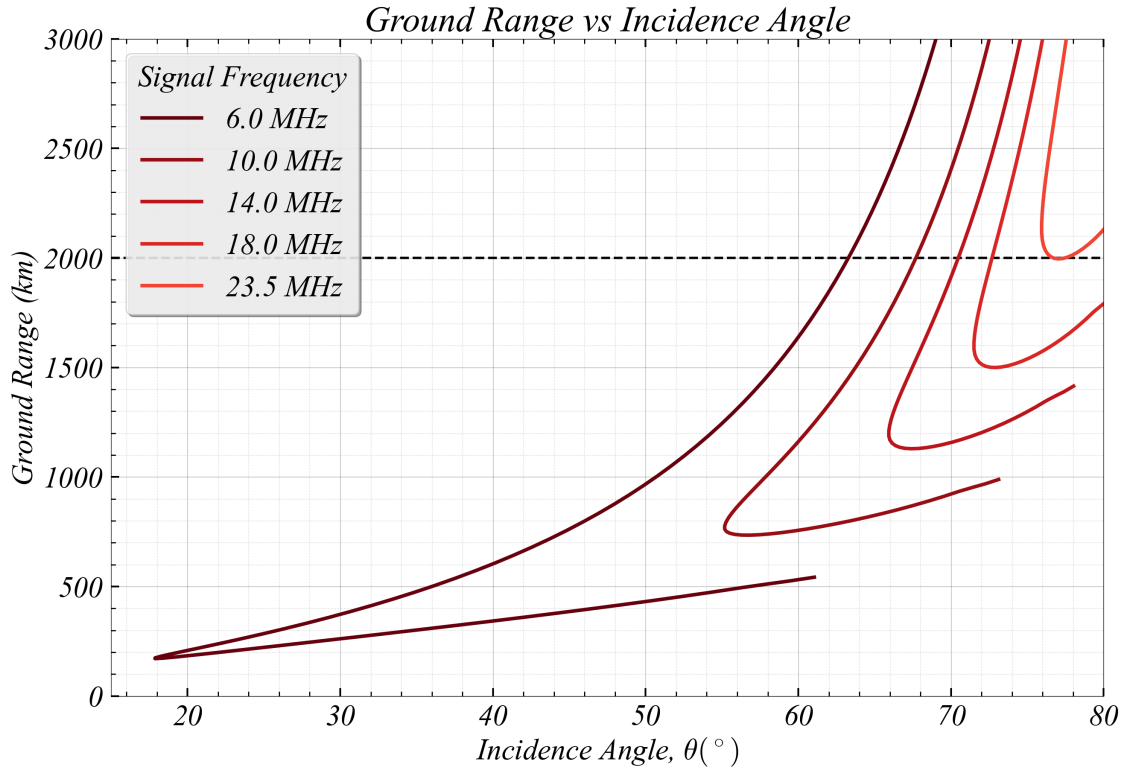


Figure 2.7: Every angle of incidence corresponds to two distinct distances on the ground, as the ray might reflect off of a different height. Alternatively, given a radio frequency one can achieve the same ground range by pointing the antenna at two distinct incidence angles, one high and the other low. The dotted line shows that 23.5 MHz is the MUF for a 2000 km link, given the plasma frequency profile in Figure 2.4

### 3. Trans-ionospheric Propagation

At radio frequencies much higher than the plasma frequency, or  $\omega \gg \omega_p$ , the wave experiences no significant refraction:  $n^2 \rightarrow 1$ . For example, the index of refraction for a 30 MHz signal propagating through ionospheric plasma with an oscillation frequency of 9 MHz is

$$n = \sqrt{1 - \left(\frac{9}{30}\right)^2} = 0.95.$$

The insufficient bending will have the wave penetrate through the ionosphere, as shown in Figure 2.3 (b). Such high-frequency signal, if transmitted from the ground, penetrates the ionosphere into outer space. By the same logic, high-frequency cosmic (extraterrestrial) signals will penetrate the ionosphere from above. The radio receivers used in this study rely on this mechanism to remote sense the ionosphere and shall be described in Section 3.2.

## 2.2 Collisions

In our previous discussion, we ignored the frictional forces that retard the motion of the electron as it tries to re-radiate the energy of the radio wave. In reality, the field of a radiowave cannot excite the electrons to oscillate indefinitely due to the damping effect of collisions. Thus, as the wave propagates it loses some of its energy. Measuring the degree of this attenuation is fundamental to remote sensing the ionosphere (as will be discussed in Section 3.2). Understanding how this attenuation negatively impacts HF radio communication and using it to infer the size of the impact region are the main goals of this thesis. To this end, this section is concerned with explaining the effects of collisions on the propagation of radiowaves.

Here, I start by modifying equation 2.15 to account for collisions:

$$m_e \frac{\partial^2 \vec{r}}{\partial t^2} = -e\vec{E} - m_e\nu \frac{\partial \vec{r}}{\partial t}, \quad (2.21)$$

where  $m_e$  is the mass of the electron,  $\vec{r}$  is its displacement from equilibrium, and  $\vec{E}$  is the electric field. We shall discuss the contribution of the magnetic field in the next section (2.3). Reasons for the form of the collisions term, a more detailed analysis of collisions, as well as a formal definition of the effective collision frequency,  $\nu$ , used here, are detailed in the treatment by Sen and Wyller (1960) and discussed in Budden (1985) and other books (see e.g., Davies, 1990; Hunsucker & Hargreaves, 2003). Again, employing the Fourier trick (see **Appendix A.3**), substituting  $\frac{\partial}{\partial t}$  with  $i\omega$ , we get

$$\begin{aligned} m_e(i\omega)^2 \vec{r} &= -e\vec{E} - m_e\nu(i\omega) \vec{r} \\ \vec{r} &= \frac{e\vec{E}}{m_e\omega^2 \left(1 - i\frac{\nu}{\omega}\right)}. \end{aligned}$$

Using equation 2.12, for polarization, we get

$$\vec{P} = -N_e e \frac{e\vec{E}}{m_e\omega^2 \left(1 - i\frac{\nu}{\omega}\right)}.$$

Using equation 2.16 as we did previously to solve for the dielectric constant, we arrive at equation 2.10:

$$\epsilon_r \epsilon_0 \vec{E} = \epsilon_0 \vec{E} - \frac{N_e e^2}{m_e \omega^2 \left(1 - i\frac{\nu}{\omega}\right)} \vec{E}$$

$$n^2 = \epsilon_r = 1 - \frac{\omega_p^2}{\omega^2 \left(1 - i \frac{\nu}{\omega}\right)}.$$

In the absence of collisions, the term  $\frac{\nu}{\omega}$  vanishes, and we retrieve our previous dispersion relation (equation 2.9). However, in the presence of collisions, the radiowave's energy is attenuated as indicated by the imaginary term. Since my research focuses on investigating the regions in the ionosphere where radiowaves lose their energy, this attenuation is of critical importance, and I shall describe it further below.

## Radiowave Absorption

The index of refraction,  $n$ , taking a complex form

$$n = \eta - i\chi, \quad (2.22)$$

where  $\eta$  and  $\chi$  are the real and imaginary components, respectively, implies that the wave vector,  $\vec{k}$ , is also complex, as given by

$$\vec{k} = \tilde{k}\hat{z} = (k + i\mathcal{K})\hat{z}, \quad (2.23)$$

where I realigned the coordinate z-axis to be parallel to the propagation direction (wave normal). One can do so without loss of generality, and I incorporate this throughout this thesis for all derivations. This complex wave vector, with wave number,  $k = \eta \frac{\omega}{c}$ , and imaginary component,  $\mathcal{K} = \chi \frac{\omega}{c}$ , leads to a vanishing electric field of the form

$$\tilde{E} = \tilde{E}_0 e^{i(\vec{k} \cdot \vec{r} - \omega t)} = \tilde{E}_0 e^{-\mathcal{K}z} e^{i(kz - \omega t)}, \quad (2.24)$$

for a wave travelling along the z-axis, where the focus here is on the vanishing field, as given by the  $e^{-\mathcal{K}z}$  term. Not only is the above condition of vanishing electric field necessary to employ the Fourier trick in the derivation, but it physically must be the case, since the radio wave is only transiting through the local region of plasma over which we are conducting our analysis. As the wave imparts its energy on the electrons, the collisional forces ensure that the wave's energy dissipates. When there is no applied force due to an electromagnetic wave, the plasma cannot sustain the natural oscillation described in Section 2.1.3, and the polarizing field due to any charge buildup must vanish, thus maintaining quasi-neutrality.

As the wave propagates, it loses its energy. The magnitude of the loss will depend on the wave trajectory

and is thus a function of the path a given ray takes. In general,

$$A \equiv \int \mathcal{K} ds, \quad (2.25)$$

where the attenuation,  $A$ , is referred to as ***Absorption***, and I shall make references to it in much of this thesis. This absorption is an accumulation of losses over small distances,  $ds$ , and  $\mathcal{K}$ , gives the decay in amplitude per unit distance, referred to as the ***Absorption Coefficient***. It can be shown (see **Appendix A.4.1** for a derivation) that  $\mathcal{K}$  takes the form

$$\boxed{\mathcal{K} = \frac{e^2}{2m_e\epsilon_0 c} \frac{1}{\eta} \frac{N_e \nu}{\omega^2 + \nu^2}}. \quad (2.26)$$

This result has direct implications for my research for a few reasons, described below.

### 1. D-region Electron Density Enhancements

Equation 2.26 implies that absorption is proportional to the electron density,  $N_e$ . This result alludes to earlier statements in Section 1 about ionization and explains why space-weather events, which enhance ionization in the atmosphere, lead to radiowave absorption. Thus absorption can be used as an indicator for geophysical events that increase the electron density in the ionosphere.

More precisely, absorption is proportional to the product of the number density of free electrons,  $N_e$ , and the collision frequency,  $\nu$ . This product attains a maximum in the D-region ionosphere, where the air density, which scales exponentially with height, is high enough that the electron motion is dominated by collisions with the neutral atmosphere (Davies, 1990). My research is concerned with remote sensing these D-region electron density enhancements and Chapter 4 presents work on estimating the spatial extent of these enhancements. Chapter 5 focuses on the consequences of increased D-region electron density associated with the aurora (such events are described in more detail in Section 2.4.3 and elaborated on in Section 3.2.4), and the impact such events have on HF propagation.

### 2. Frequency Dependence

The second important result of equation 2.26 is that absorption is inversely proportional to the square of the frequency of the radiowave. Thus, higher-frequency radiowaves are less attenuated. Absorption of low-frequency waves in the D-region sets a threshold for the lowest frequency radio operators can use to establish a HF link between two locations– known as the ***Least Usable Frequency (LUF)***. This is why

lower-frequency signals can reach much larger distances during the night, when the D-region disappears due to recombination. Solar and geomagnetic disturbances will generally increase the LUF (S. E. Milan et al., 1998; Uryadov et al., 2019), due to the enhanced D-region ionization. This result is therefore necessary when interpreting the effects these disturbances have on HF propagation, and I shall advert to this result (implicitly or explicitly) in discussing the work in Chapters 4 and 5.

This result is also fundamental to the operation of the instruments used in this study, discussed in Section 3.2, which avoid using low-frequency signals when quantifying absorption, since the absorption can be abnormally high, effectively extinguishing the wave's energy (Hunsucker & Hargreaves, 2003).

Other implications as well as some notes pertaining to this frequency dependence are discussed later in Section 6.2.1, as some complications arise when scrutinizing this relationship.

## 2.3 Effects of Earth's Magnetic Field

Earth's magnetic field contributes to the electron motion significantly. In the context of radiowave propagation, and for this thesis, I limit our discussion to the implications of the geomagnetic field on the dispersion relations derived earlier in Sections 2.1.3 and 2.2, and focus on a special case highly relevant to the instrumentation I use, which I shall describe in more detail in Section 3.2.

### 2.3.1 Anisotropic Medium

When we add the magnetic field contribution to the equation of motion, 2.21, it reads

$$m_e \frac{\partial^2 \vec{r}}{\partial t^2} = -e\vec{E} - m_e\nu \frac{\partial \vec{r}}{\partial t} - e \frac{\partial \vec{r}}{\partial t} \times \vec{B}, \quad (2.27)$$

where  $\vec{B}$  represents the geomagnetic field. This modification leads to a new dispersion relation, characterized by anisotropy— i.e., different properties in different directions with respect to the magnetic field. The index of refraction, given by the Appleton-Hartree equation is quoted below, but is fully derived in **Appendix A.5**. The equation reads

$$\boxed{n^2 = 1 - \frac{X}{U - \frac{Y_T^2}{2(U-X)} \pm \sqrt{\frac{Y_T^4}{4(U-X)} + Y_L^2}}},$$

where  $U = 1 - iZ$ ,  $Z = \frac{\nu}{\omega}$ , and  $X$  is the previously derived electric susceptibility, defined in equation 2.2 ( $X = \frac{\omega_p}{\omega}$ ).  $Y_T$  and  $Y_L$  correspond with components of Earth's magnetic field in the traverse and longitudinal directions with respect to direction of wave propagation, respectively. These quantities are defined more precisely below. For now, I want to note that the introduction of the geomagnetic field allows for two modes of propagation, as indicated by the  $\pm$  sign, referring to the ***Ordinary (O-mode)*** and ***Extraordinary (X-mode)***, respectively. Each mode has a distinct wave phase that changes differently over time, and the plus sign refers to the O-mode.

Figure 2.8 gives an interpretation of the longitudinal and traverse directions. Aligning our propagation axis with the  $\hat{z}$  direction, we can orient our coordinate axes such that the magnetic field lies in the  $xz$ -plane. In this frame,

$$Y_L = \frac{\omega_c}{\omega} \cos \theta$$

$$Y_T = \frac{\omega_c}{\omega} \sin \theta,$$

where  $\theta$  is the angle between the wave normal and the geomagnetic field, and  $\omega_c$  is the electron ***Gyrofrequency*** given by equation 2.8

$$\boxed{\omega_c = \frac{e \|\vec{B}\|}{m_e}}.$$

(2.28)

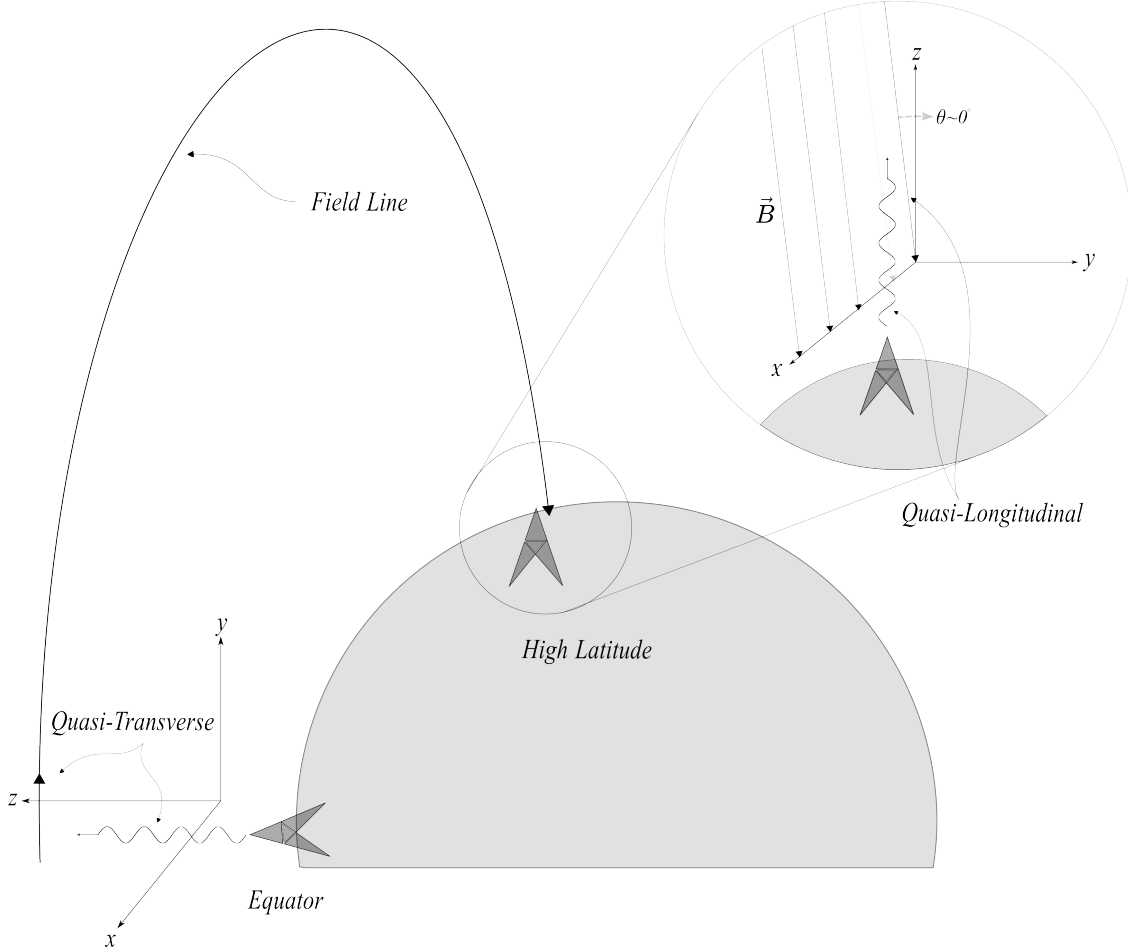


Figure 2.8: Illustration showing the geomagnetic field, which is roughly horizontal at the equator, and roughly vertical at high latitudes. The propagation dynamics of the radiowave depend on how the wave normal is oriented with respect to the geomagnetic field—whether it is perpendicular (transverse) or parallel (longitudinal) to the field. For high latitudes, orienting the wave normal with the  $z$ -axis of our coordinate system, with the geomagnetic field in the  $xz$ -plane, trans-ionospheric waves line up with the field such that  $\theta \approx 0$ .

### 2.3.2 Quasi-Longitudinal Approximation

This introduced notation not only simplifies the computations but has a geometric interpretation. At the equator, the magnetic field is roughly horizontal. Near the poles, the opposite is true, with the geomagnetic field lines having an approximately vertical orientation, as shown in Figure 2.8. For vertical radio waves at high latitudes  $\theta \approx 0^\circ$  and  $Y_T \approx 0$  ( $\sin(180^\circ) = 0$ , and one may switch the  $z$ -axis orientation to point with the field not against it), allowing us to simplify equation 2.1 to 2.11:

$$n^2 = 1 - \frac{X}{U \pm Y_L}$$

As we shall see in Chapter 3, most of the data used in this thesis comes from instrumentation at high latitudes, which motivates a discussion of a special case of propagation when  $Y_T = 0$  in equation 2.1 also known as the quasi-longitudinal approximation. This is the case for trans-ionospheric waves at high latitudes, where the magnetic field lines are roughly vertical, as shown in Figure 2.8.

### 2.3.3 Trans-ionospheric Propagation

An important implication of this aforementioned approximation is that the absorption coefficient is only slightly modified. For trans-ionospheric rays that exhibit no significant bending (i.e.,  $\eta \rightarrow 1$ ),

$$\mathcal{K} \approx \frac{e^2}{2m_e\epsilon_0c} \frac{N_e\nu}{(\omega \pm \omega_c)^2 + \nu^2}, \quad (2.29)$$

where  $c$  is the speed of light. Refer to **Appendix A.4.2** for the full derivation. For a wave with frequency  $f \geq 30$  MHz, one can ignore the electron gyrofrequency (Hunsucker & Hargreaves, 2003), and instead use

$$\mathcal{K} \approx \frac{e^2}{2m_e\epsilon_0c} \frac{N_e\nu}{\omega^2 + \nu^2}. \quad (2.30)$$

For reference,  $f_c = \frac{\omega_c}{2\pi} \approx 1.56$  MHz at  $60^\circ\text{N}$ ,  $95^\circ\text{W}$ , and 85 km altitude. In summary, if the wave's frequency is much greater than both the gyrofrequency and the plasma collision frequency, the absorption, in decibels, is given by

$$A(dB) = 4.611 \times 10^{-5} \int \frac{N_e\nu}{\omega^2 + \nu^2} dh, \quad (2.31)$$

where  $dh$  is the differential height element, since the wave is trans-ionospheric. At frequencies  $\geq 30$  MHz, the collision term is small in comparison with the wave's frequency, and absorption becomes proportional to the inverse of the frequency:

$$A(dB) \propto \frac{1}{\omega^2} \int N_e\nu dh. \quad (2.32)$$

These results will be employed for the high-latitude instrumentation used in this thesis (Section 3.2), where the propagation of trans-ionospheric waves is fundamental to remote sensing.

## 2.4 Relevant Absorption Phenomena

The focus of this thesis is on phenomena pertaining to radiowave absorption in the ionosphere, which I have shown is proportional to the density of free electrons in Section 2.2. To that end, it is worth discussing some of the major sources of electron density enhancements, especially at high latitudes where the geomagnetic field and its interaction with the solar wind allow for energetic particle precipitation, and where the instruments I use are located. In the following, I describe each major event, its spatial and temporal signature, and describe how it is identified using indicators.

### 2.4.1 Short Wave Fadeout

Following a solar flare, radiation from the Sun ionizes the entire sun-lit ionosphere. Radiation with wavelengths in the 1–8 Angstroms ( $\text{\AA}$ ), corresponding to X-rays, ionizes the D-region— sometimes up to tenfold the pre-flare electron density (e.g., Davies, 1990), resulting in radiowave absorption. The X-ray Flux (XRF), as measured by near-Earth satellites, is therefore an indication of the level of impact. The division of flares into classes according to XRF is shown in Table 2.1. Each letter corresponds to an order of magnitude increase in flux, with numbers serving as sub-levels, adding an extra digit (further subdivisions might be needed for strong X flares). An M5 or higher level flare (and some lower-level flares) will incur significant attenuation for radiowaves in the HF range, hence the name ***Shortwave Fadeout (SWF)***. The Space Weather Prediction Center (SWPC), operated by the National Oceanic and Atmospheric Administration, issues warnings when the Geostationary Satellite (GOES) measures flux at M5 or higher levels (see <https://www.swpc.noaa.gov/products/goes-x-ray-flux>).

Flare Class	X-ray Flux ( $W/m^2$ )
A	$\geq 10^{-8}$
B	$\geq 10^{-7}$
C	$\geq 10^{-6}$
M1	$\geq 10^{-5}$
M5	$\geq 5 \cdot 10^{-5}$
X	$\geq 10^{-4}$

Table 2.1: Solar flares and their classification according to X-ray flux.

SWF is characterized by an abrupt onset, about 8.3 minutes after a solar flare erupts (the time it takes light to reach Earth), followed by a gradual recovery to pre-flare conditions— the entire process lasting up to several hours. The degree of radiowave absorption depends on the solar-zenith angle, with radiowaves closest to the subsolar point having the highest absorption levels. Chapter 4 uses a SWF event to illustrate

the methodology by which we can remote sense electron density enhancements in the D-region.

### 2.4.2 Polar Cap Absorption

Some large flares are accompanied by ejections of energetic protons. When these protons reach the magnetosphere, they travel down open field lines close to the poles, in a region called the ***Polar Cap***. Nominally, the lower-latitude polar cap boundary marks the transition from closed to open field lines, as shown in Figure 2.9.

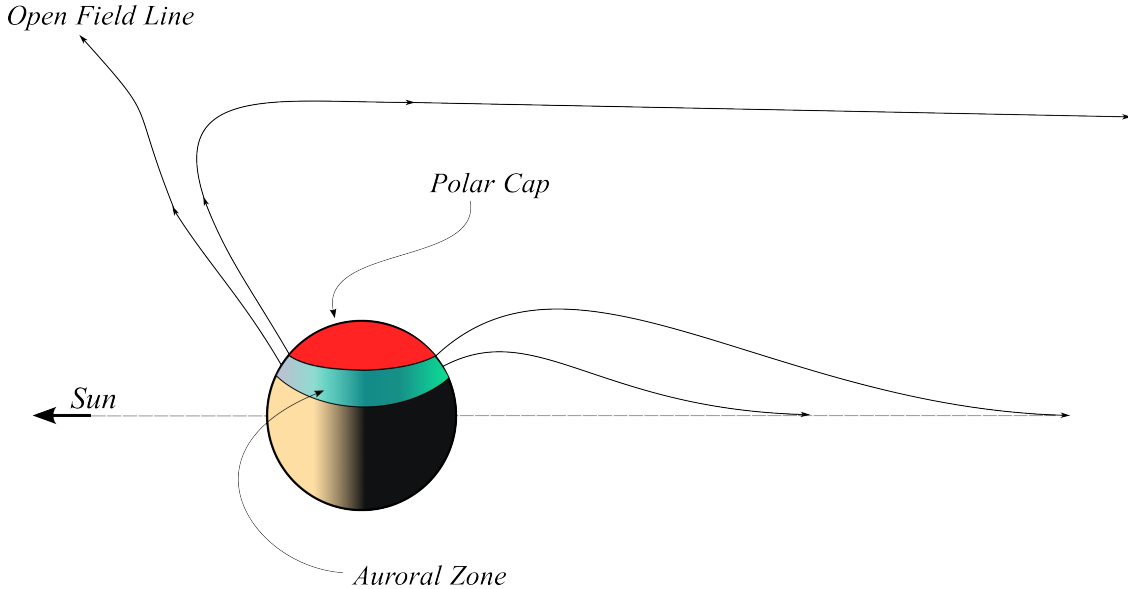


Figure 2.9: Illustration of the polar cap and auroral zone.

The ejected protons can have energies of hundreds of MeVs. Most of the ionization produced by these protons occurs as they slow down near the end of their path, deep into the atmosphere (Hunsucker & Hargreaves, 2003). A 30 MeV proton can penetrate up to 50 km altitude, and produce enough ionization to cause absorption (Davies, 1990). Proton flux measured by satellites can serve as an indicator for such an event, referred to as ***Polar Cap Absorption (PCA)***. When the detectors on the Geostationary Satellite (GOES) measure an integrated flux of more than 10 protons per  $cm^2 \cdot s \cdot sr$  (or 10 proton flux units- pfu) with  $\geq 10$  MeV energy, SWPC issues a warning (see <https://www.swpc.noaa.gov/products/goes-proton-flux>). 1 pfu at  $\geq 100$  MeV also prompts a warning, with higher-level warnings for more integrated flux at these energy channels.

Although relatively infrequent, such events can cause radio blackouts (complete disruption of HF circuits) and cover a large area. The proton precipitation area will mark the boundary of the polar cap and is therefore

related to the area impacted by radiowave absorption. Temporally, these events can last days on end. While not the focus of this thesis, PCA events signatures require modifications to the methodology outlined in Chapter 4 as discussed in Section 4.6. Moreover, I intentionally filter out times where PCA is taking place in the analysis presented in Chapter 5.

### 2.4.3 Auroral Absorption

Surrounding the polar cap is a zone of closed field lines called the ***Auroral Zone***, where the luminous aurora take place. A rough illustration is shown in Figure 2.9. The display of light is a consequence of energetic particles from within the magnetosphere trickling down the atmosphere, colliding with its constituents and exciting them to higher energy states. Subsequent relaxation produces emissions of different wavelengths (seen as colors when in the visible part of the spectrum).

Energetic electrons penetrating the atmosphere will ionize more particles as they slow down due to the increasing density with lower altitudes. These electrons might rapidly decelerate upon colliding with the neutral constituents, releasing X-rays in the process– a phenomenon called Bremsstrahlung Radiation, which ionizes much deeper layers of the atmosphere (e.g., Hunsucker & Hargreaves, 2003). The enhanced ionization in the D-region due to the auroral energetic electrons leads to ***Auroral Absorption (AA)***. The mechanisms by which energetic electron precipitation takes place originate in the magnetosphere and are out of the scope of this thesis. It suffices to say that many mechanisms allow for precipitation, making it difficult to distinguish between different AA events. These events appear to be sporadic, with high spatial and temporal variability between events.

These events are a direct consequence of the magnetosphere’s interaction with the solar wind. The range of variation of magnetic field measurements from magnetometer stations spread across the auroral zone is therefore a good indicator of the overall geomagnetic disturbance. This range is called the Auroral Electrojet (AE) index, where the term electrojet refers to the stream of electric current resulting from such disturbances. An AE index of more than 400 nT indicates high levels of auroral activity, serving as proxy for AA.

# Chapter 3

## Data and Instrumentation

### 3.1 Solar and Geomagnetic Indices

Introduced briefly in the previous section (2.4) were indicators for each of the mentioned absorption phenomena. Proton and X-ray Flux from GOES serve as indices for PCA and SWF, respectively. Data from GOES will be used in this chapter to supplement the illustration of PCA and SWF signatures and later in Chapter 4) to supplement the analysis of the result. In Chapter 5, GOES data is used as the work requires filtering out PCA and SWF events to target only AA events. The AE index, indicative of AA events, obtained from the Canadian Array for Realtime Investigations of Magnetic Activity (Mann et al., 2008) is used in this chapter for illustration, and that obtained from National Aeronautics and Space Administration's OMNI (not an acronym) data set (King & Papitashvili, 2020) is used in Chapter 5.

### 3.2 Riometers

The *Relative Ionospheric Opacity Meter for Extra-terrestrial Radiation* (**RIOMETER**) is the main instrument used throughout this thesis. Therefore, this chapter is dedicated to explaining its operational principles and give a basic foundation for the results derived in Chapters 4 and 5.

Soon after Shain (1951) had discovered the ionospheric absorption of galactic background noise, the riometer was introduced (Little & Leinbach, 1959). The riometer is a radio receiver designed to measure the degree of *Cosmic Noise Absorption* (**CNA**). A picture of a riometer installation is shown in Figure 3.1. The antenna feeds to a nearby storage containing the actual receiver.



Figure 3.1: Picture showing a riometer site.

These radio receivers became the standard for measuring radiowave absorption, especially at high latitudes where the attenuation can be high during extreme space-weather events, like SWF, often causing blackouts in the HF range. Riometers were used to verify AA and helped distinguish PCA as a separate type of event (Hunsucker & Hargreaves, 2003).

This instrument is designed for passive monitoring of ionospheric absorption. Two main aspects of this design allow for continuous remote-sensing of the D-region: the operating frequency and antenna radiation pattern.

### Operating Frequency

The riometer operates at the upper end of the HF range- and some at the lower end of the Very High Frequency (VHF) range, overall somewhere between  $\sim$ 20 to 50 MHz (Hunsucker & Hargreaves, 2003). Terrestrial transmissions in that range, even if transmitted at an oblique angle, are likely (though are not guaranteed) to penetrate the ionosphere without significant refraction (see Figure 2.3 (b)). Extra-terrestrial signals in that frequency range will also penetrate the ionosphere, though entering from outer space. Therefore, the signal measured by riometers is not affected significantly by refraction (i.e., the signal is trans-ionospheric). These cosmic signals' energy is mainly absorbed in the D-region, due to collisions. Attenuation due to other

factors such as scattering or partial reflection is insignificant in comparison with that due to collisions, and thus can justifiably be ignored (Appleton & Piggott, 1954).

Operating at a relatively high frequency ensures some measurements are made during extreme space weather events, when the absorption is quite significant, since absorption is proportional to inverse square of the frequency. For reference, 3 dB absorption (about half the power lost) at 30 MHz roughly corresponds to 12 dB at 15 MHz (about  $17\times$  reduction in power):

$$\frac{A(15 \text{ MHz})}{A(30 \text{ MHz})} \propto \frac{(1/15)^2}{(1/30)^2} \Rightarrow A(15 \text{ MHz}) \propto \frac{30^2}{15^2} \cdot 3 \text{ dB} = 12 \text{ dB},$$

where we are using the quasi-longitudinal approximation, and assuming that the collision frequency of the electrons is smaller than the frequency of the radiowave ( $\omega \gg \nu$ ).

A riometer will typically operate at, or above, 30 MHz, since, at lower frequencies, the receiver might be susceptible to interference from terrestrial, skywave transmissions, while, at higher frequencies, the sensitivity to absorption decreases, making it harder to detect events representing low or moderate geomagnetic/solar activity. The specific mention to skywave signals is made to distinguish them from line-of-sight signals, which are large sources of noise but could occur at any frequency. Some sources are airport beacons and local repeaters but could be any electrical system that produces radiation. Since shielding is not an option, mitigation usually involves placing the riometer in isolated environments with minimal radio pollution. Choosing the operating frequency is a form of mitigation. A survey of the local environment can inform the operator, for the region of deployment, what frequency to use; though, there will always be the occasional (though less likely) interference from signals at unregistered frequencies.

### Antenna Radiation Pattern

Although the choice of frequency ensures minimal interference from ionospherically propagating signals, the riometer requires an antenna with a sensitivity maximum at zenith to ensure the reception of signals from extra-terrestrial sources. The antennae radiation pattern varies by installation. A standard riometer will use an antenna with a radiation pattern (the gain sensitivity in different directions) maximizing at zenith, with  $\sim 60^\circ$  between half-power points- herein referred to as the nominal ***Field-of-View (FOV)*** of the instrument. This setup is referred to as a widebeam riometer, since, at D-region altitudes of about 85 km, the FOV corresponds to a diameter of  $\sim 100$  km; a schematic illustration is presented in Figure 3.2. The power is therefore an average of all radiation in this FOV, analogous to a very large pixel in an optical

system. It is therefore hard to detect distinct radio sources using riometers.

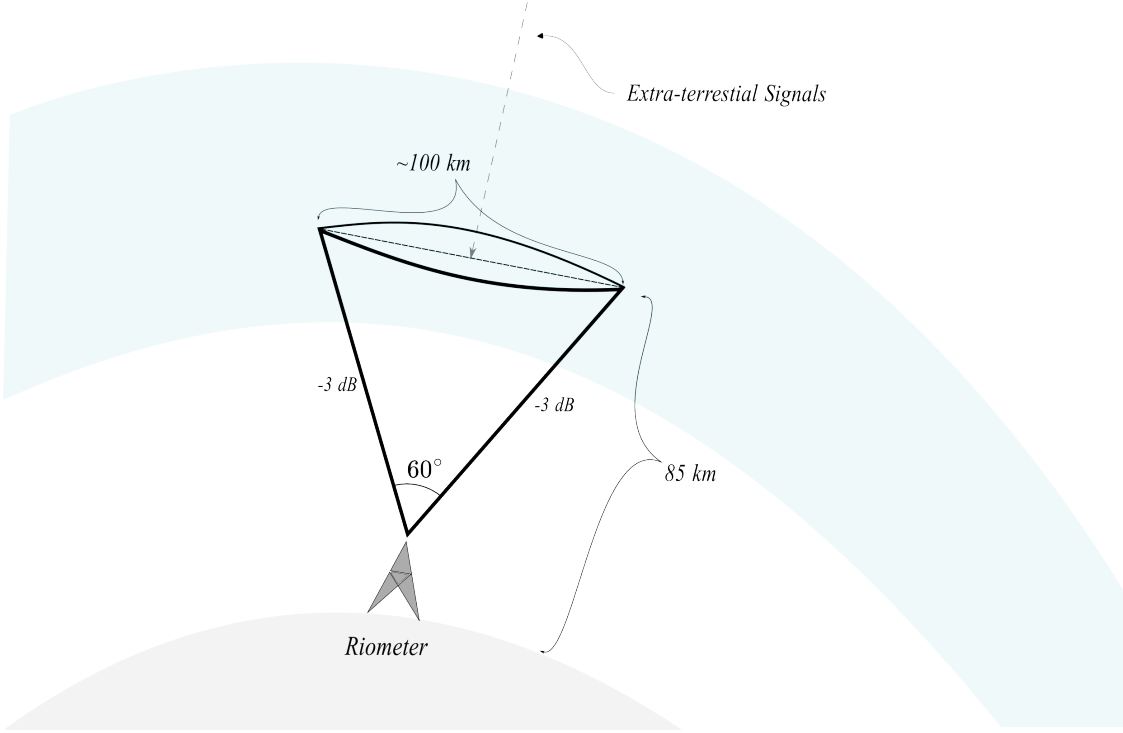


Figure 3.2: Illustration of the nominal riometer FOV, defined as the cone encapsulating the half-power points when projected to D-region altitudes of  $\sim 85$  km.

A newer version of the riometer uses multiple antennae to generate multiple, narrower beams, able to detect radiation on a finer spatial scale (Detrick & Rosenberg, 1988). While such an instrument is not used in this thesis, some reference will be made to such system, herein called an ***Imaging Riometer***, due to the relevant results it lends to the field of study.

In summary, the riometer antenna is designed to be most sensitive to radiation arriving at zenith. Operating much above the plasma critical frequency, riometers are less susceptible to skywave signals that ionospherically propagate to the receiver. The riometer, therefore, receives mostly trans-ionospheric, extra-terrestrial radiowaves, originating from the galaxy, the Sun, and other celestial sources.

### 3.2.1 Baselines

In the final results presented in Chapters 4 and 5, absorption measurements are used. Here I outline how baseline riometer measurements are generated in order to quantify absorption via deviations from the baseline.

#### Sidereal Day

As the Earth spins about its own axis, the riometer's FOV will sweep out a portion of the galactic plane with a period of one sidereal day. Galactic radio sources and any distant star will revolve around an observer's zenith at that period. Simply put, a sidereal day is the time it takes Earth to complete one rotation with respect to the distant stars, as shown in Figure 3.3. The distant stars move faster than the Sun across the sky, hence a sidereal day is 3 minutes and 56.56 seconds shorter than a solar day. As shown in Figure 3.3 (though exaggerated), in one sidereal day the Earth rotates as it orbits around the Sun, moving about  $1^\circ$  of arc along its orbit. The Earth would have to further turn by an angle  $\Delta\theta < 1^\circ$  in order complete a solar day. The flow of sidereal time depends on the constancy of Earth's rotation which is changing at a negligible rate over the period of weeks.

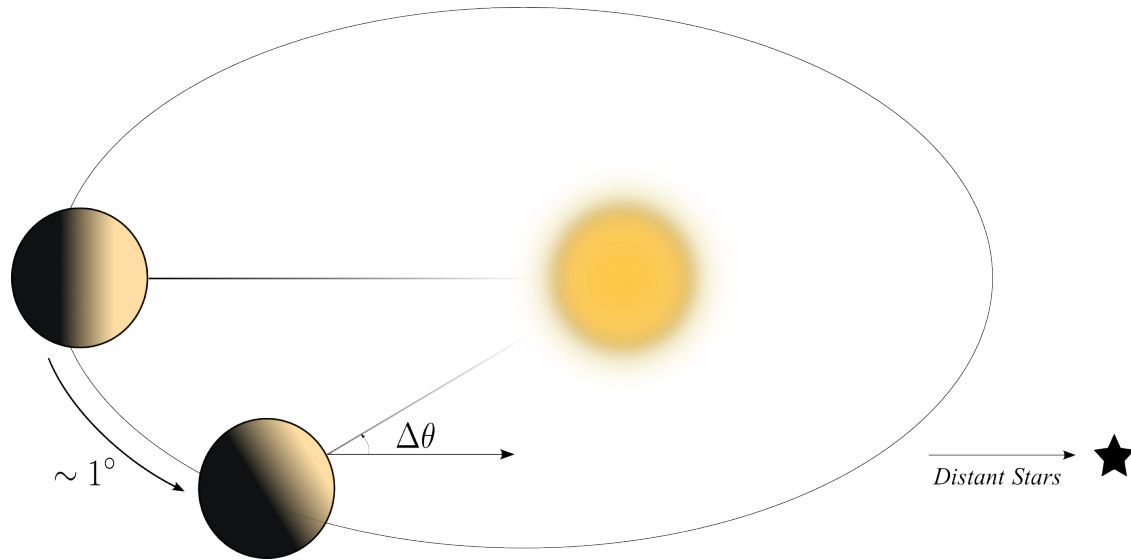


Figure 3.3: As the Earth completes one full rotation about its orbital axis, traveling the  $\sim 1^\circ$  of arc greatly exaggerated in the figure, it faces the distant stars. A further rotation of  $\Delta\theta$  (much exaggerated) is required to face the Sun again.

### The Quiet Day Curve

In the absence of solar and geomagnetic disturbances, such as those defined in Section 2.4, the signal traced out by a riometer is governed by two main factors: the cosmic background, tied to the portion of the Galactic plane coinciding with the riometer’s FOV, and the diurnal variation of ionospheric electron density affecting radiowave absorption in the D-region. Example data from a quiet day is shown in Figure 3.4. The cyclic curve reflects the riometer’s geographic position as it relates to what portion of the Galactic plane it sweeps (as a function of time) and at what time the Sun rises and sets on the riometer. In the figure, the voltage is a function of Coordinated Universal Time (UTC), which is coordinated with solar time. For a discussion about sidereal time, universal time, as well as conversions between the two, the reader is referred to Karttunen, Kröger, Oja, Poutanen, and Donner (2017).

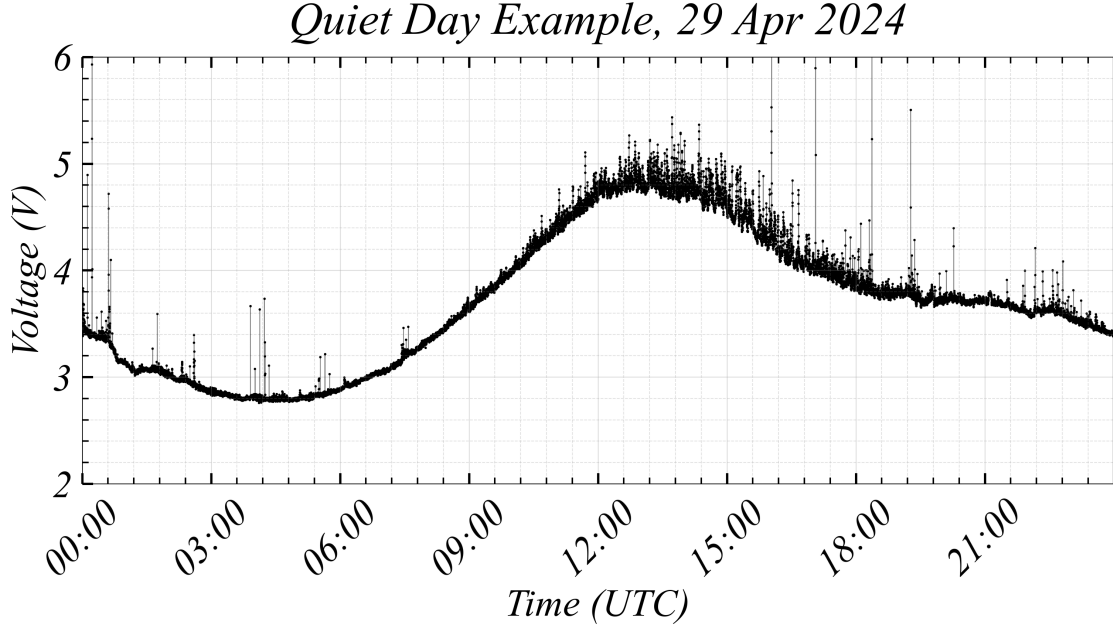


Figure 3.4: Data from a quiet day. Signal voltage level is recorded as a function of Coordinated Universal Time (UTC) for a riometer operating at 30 MHz. Data taken from a riometer at Prince George.

Quiet days form a baseline for the cosmic signal levels. Riometers quantify absorption via deviation from that baseline— called the ***Quiet Day Curve (QDC)***. To calculate the QDC, one must aggregate data over many quiet days (typically weeks), to effectively characterize both the galactic signal and the background ionospheric conditions. A quiet day (a day void of geomagnetic or solar activity), by this definition, may be contaminated by noise. Noise, in this context, is any form of instrumental, terrestrial transmission, or other interference that clouds the galactic background signal. One serious limitation to the riometer technique is

solar radio bursts observed in the daytime due to the more-active parts of the Sun referred to as sunspots. Figure 3.5 shows an example of a solar burst as observed in riometer data. Immediately after the Sun flares, it releases bursts of radio noise, which is picked up by the riometer, seen as huge positive excursions of signal voltage levels. These bursts can cloud the subsequent reduction in signal level which the riometer aims to measure. In this particular case, the strong flare around 17 UTC caused the riometer to saturate. Besides bursts, the almost regular downward excursion in signal level showcases calibration spikes.

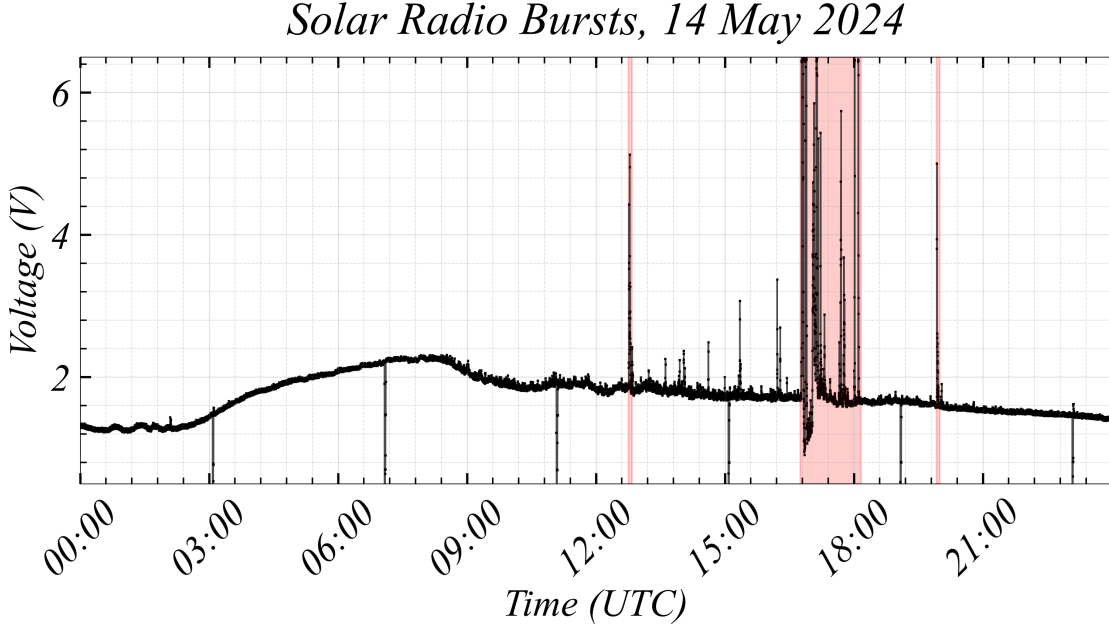


Figure 3.5: The signature of solar radio bursts in riometer data. Shown is signal voltage as a function of time. Radio burst signatures are highlighted in red. The regular downward spikes in signal levels are simply calibration spikes. Data taken from a riometer at Rankin Inlet.

Typically, a one-month QDC is used to study events, as that period strikes a fine balance between having sufficient data to statistically represent the galactic background signal without introducing any seasonal variation. However, data aggregates of a week can also be used, and are sometimes preferred, when instrumental or environmental noise varies significantly over the month. For example, the noise floor of the receiver can start to drift over the month. Additionally, while instrumental noise can be mitigated or corrected, the same cannot always be done for the radio environment surrounding the instrument. For example, interference from local sources is often elusive and unpredictable, making it difficult to model and rectify.

Once the data is collected and filtered for noise and times with high solar or geomagnetic activity, it is binned in sidereal time. Once binned, the data is put through an averaging algorithm to generate a smooth

baseline curve (QDC), that is continuous over a sidereal day period. These algorithms vary in complexity, and the reader is referred to (Drevin & Stoker, 1990, 2003; He et al., 2014; Krishnaswamy et al., 1985) for more information. Care is to be taken regarding the units used (voltage as opposed to power), as there is a non-linear relationship between decibels and volts (Krishnaswamy et al., 1985). Using units of power, the absorption measured is given by

$$A(dB) = 10 \log_{10} \left( \frac{P_0}{P} \right), \quad (3.1)$$

where  $P$  is measured power, and  $P_0$  is that of the QDC. Finally, the algorithm converts the absorption measurements (or the QDC) from sidereal to UTC time bins. For an algorithm that shows conversions between and sidereal time and UTC, please refer to Meeus (1991).

My work on baselining is detailed in **Appendix B**, though the reader is advised to visit this appendix last (after reading Chapter 6 to be specific, as I wrote these chapters with topic transition in mind), or after reading this chapter, to get a sense of riometer data first.

### 3.2.2 Prototype Hyperspectral Riometers

This thesis uses data from the newly developed Space Weather Adaptive Network (SWAN) of multi-frequency riometers, herein referred to as *Hyperspectral Riometers (HSRs)*. These new digital systems operate in the range of  $\sim 12.24$  kHz – 50 MHz, and are planned to replace the Geospace Observatory (GO)-Canada network of analog riometers. A map showing all riometers used in this thesis is provided in Figure 3.6, with riometers belonging to the GO-Canada network to be discussed in the next section (Section 3.2.3). Exact locations of these instruments is given in Table 3.1.

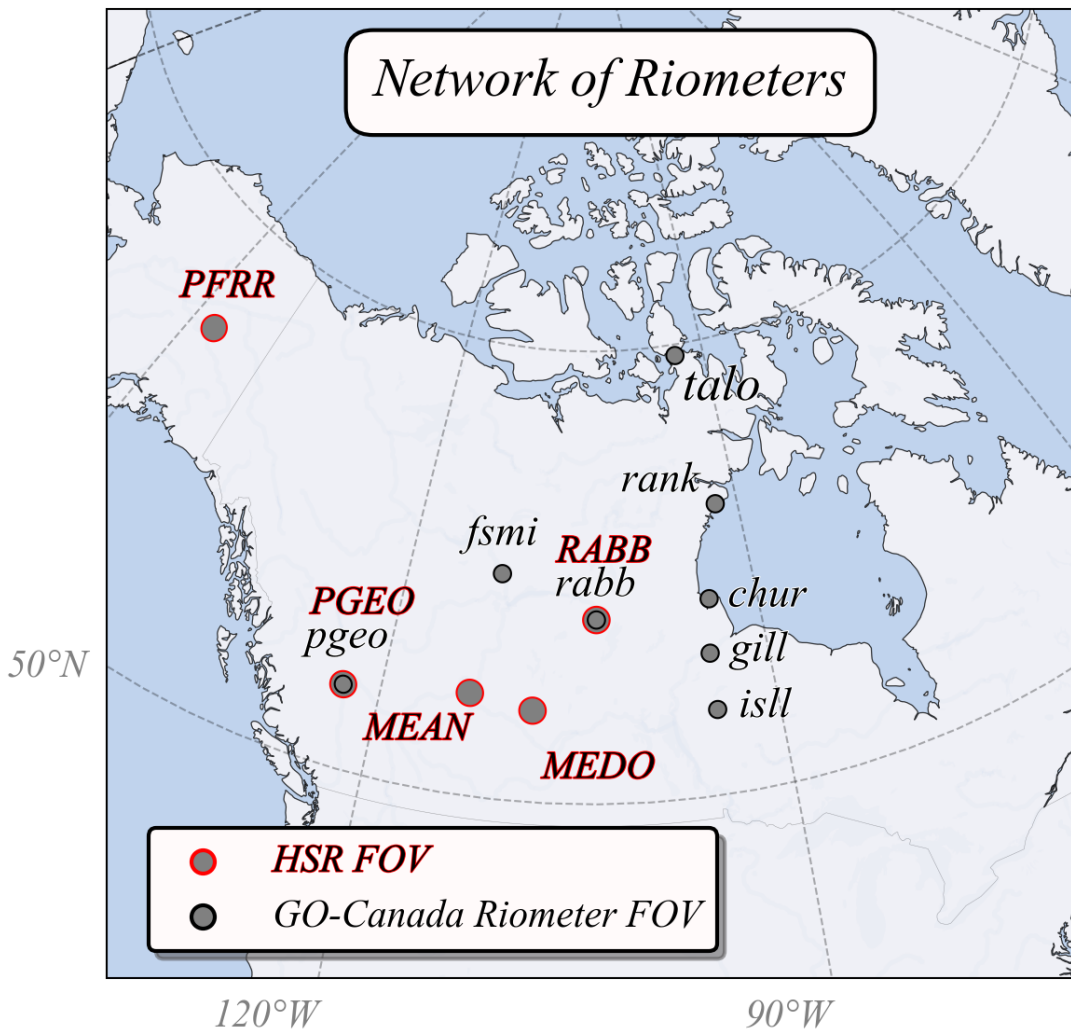


Figure 3.6: A map of riometers used in this study. The HSRs are shown as gray circles with red boundaries, indicating the nominal FOV as projected to 85 km altitude, covering  $\sim 200$  km in diameter across. The GO-Canada riometers FOVs are indicated via gray circles with black boundaries, covering  $\sim 100$  km in diameter. To note is an HSR colocated with a GO-Canada riometer at Rabbit Lake (RABB) and Prince George (PGEO), with uppercase denoting the HSR. For each HSR and their site code, refer to Table 3.1.

The HSRs use the same antennae as those of the Long Wavelength Array – a cross-dipole, inverted V, antenna (see [https://www.reeve.com/RadioScience/Antennas/ActiveCrossed-Dipole/LWA\\_Antenna.htm](https://www.reeve.com/RadioScience/Antennas/ActiveCrossed-Dipole/LWA_Antenna.htm)). The radiation pattern exhibits a nominal FOV of  $\sim 100^\circ$  between the 3 dB points, which would span  $\sim 200$  km across the sky when projected to 85 km altitude. This FOV projection is approximated with a gray circle with red borders in Figure 3.6.

## Hyperspectral Riometers

Site Code	Location	Geodetic Latitude ( $^\circ$ )	Geodetic Longitude ( $^\circ$ )
PFRR	Poker Flat, Alaska	65.13	-147.50
RABB	Rabbit Lake, Saskatchewan	58.23	-103.68
MEAN	Meanook, Alberta	54.62	-113.35
MEDO	Meadow Lake, Saskatchewan	54.13	-108.51
PGEQ	Prince George, British Columbia	53.76	-122.85

Table 3.1: Site abbreviation code, location, and geodetic coordinates for HSRs used in this thesis.

Data from the HSRs used here date back to 2021, though I make mention of one event during the earliest prototype testing stages in Section 6.2.1. Part of my work with these instruments was to curate data for the public, using frequency bins that are not contaminated with noise (for examples on noise, see **Appendix B**). These data are publicly available at [https://data.phys.ucalgary.ca/sort\\_by\\_project/SWAN/hsr/10/](https://data.phys.ucalgary.ca/sort_by_project/SWAN/hsr/10/), and is derived from the full spectrum data (currently not available to public). An example showing the full-spectrum as well as single-band data is shown in Figure 3.7.

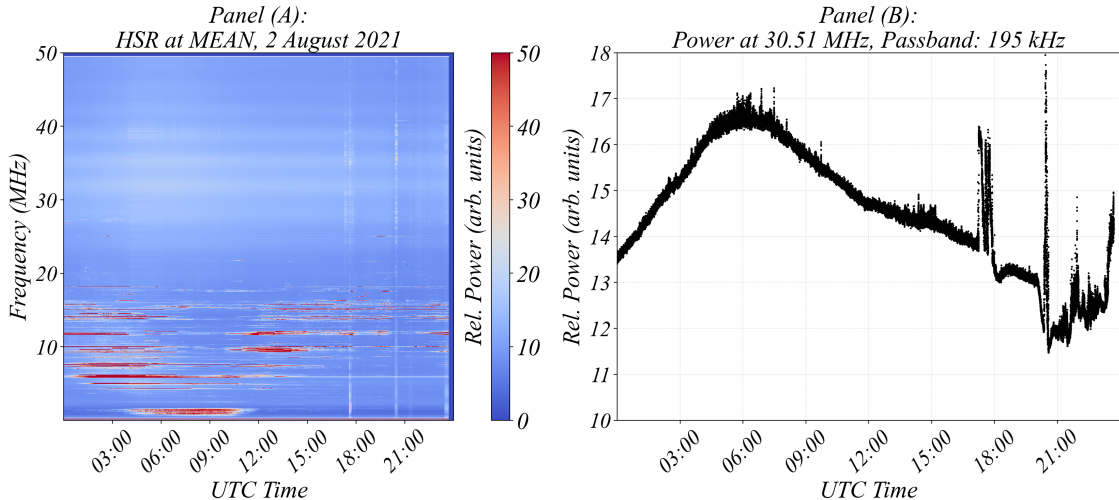


Figure 3.7: Panel (A) (left) shows full spectrum data for signals in the range 0.01–49.50 MHz from an HSR at Meanook (MEAN). Panel (B) (right) shows observed power in a 195 kHz (16 bins) passband centered around 30.51 MHz as a function of time.

Data for a single day from the HSR at MEAN is shown in Figure 3.7. As discussed earlier, signals in the 20–50 MHz range are mainly extra-terrestrial, and the low power of those signals can be contrasted with the high-power terrestrial transmissions below  $\sim 20$  MHz. While the higher frequencies serve the purpose of quantifying CNA, the lower frequencies provide the added benefit of characterizing the HF propagation environment. One notable propagation feature is the decay of the LUF, the lowest-frequency signal which can be operationally used to establish an HF link between a receiver and transmitter, seen as the lower envelope of the observed signals' frequency, during the night. Higher absorption in the D-region ionosphere during the day has a higher impact on the lower-frequency signals, hence less absorption during the night allows for lower-frequency HF links to be established.

The opposite is true for higher-frequency signals, though absorption is not the only factor at play. Since the higher frequencies are less affected by absorption, the decrease in MUF is not attributed to D-region effects. Instead, the lower ionization during the night decreases the peak plasma frequency of the F-layer (lifted to higher altitudes), which decreases the MUF. Thus, the decrease in LUF is matched with a decrease in MUF as the Sun goes down on the HSR, due to the subsiding ionization effectively lowering the plasma frequency profile (see Section 2.1.3. The opposite effect is observed as night turns to day; then, the MUF increases mainly due to higher ionization in the F-region.

The HSRs' extended bandwidth of frequencies below 30 MHz aids in examining skywave signal propagation, which is atypical for a multi-frequency riometer. These signals can hop multiple times between the Earth and the ionosphere (as in Figure 2.3 (a)) and reach the HSR at various angles of arrival. This extended bandwidth allowed for the development of a methodology for estimating the spatial extent of D-region electron density enhancements, discussed further in Chapter 4.

### 3.2.3 The GO-Canada Riometer Network

Other data used in this thesis is from the Geospace Observatory Canada (GO-Canada) riometer network, managed by the University of Calgary. These riometers operate at 30 MHz with a passband of  $\sim 250$  kHz. Their locations and coordinates are listed in Table 3.2.

Figure 3.6 shows the GO-Canada riometers' FOV as projected to 85 km altitude. The half-power points of their antennae spans  $\sim 30^\circ$  on either side of zenith, as illustrated in Figure 3.2. Projected to the D-region, at about 85 km, the FOV is  $\sim 100$  km across the sky. GO-Canada riometers used in this study have their locations, coordinates, and site code abbreviations (which are used herein to refer to them) summarized in Table 3.2. Riometer data is publicly available at [https://data.phys.ucalgary.ca/sort\\_by\\_project/GO-Canada/GO-Rio](https://data.phys.ucalgary.ca/sort_by_project/GO-Canada/GO-Rio) and dates back to 2005.

#### Go-Canada Riometers

Site Code	Location	Geodetic Latitude ( $^\circ$ )	Geodetic Longitude ( $^\circ$ )
<i>talo</i>	Taloyoak, Nunavut	69.54	-93.56
<i>daws</i>	Dawson City, Yukon	64.05	-139.11
<i>rank</i>	Rankin Inlet, Nunavut	62.82	-92.11
<i>fsmi</i>	Fort Smith, Northwest Territories	60.03	-111.93
<i>chur</i>	Fort Churchill, Manitoba	58.76	-94.09
<i>rabb</i>	Rabbit Lake, Saskatchewan	58.23	-103.68
<i>gill</i>	Gillam, Manitoba	56.38	-94.64
<i>isll</i>	Island Lake, Manitoba	53.86	-94.66
<i>pgeo</i>	Prince George, British Columbia	53.76	-122.85

Table 3.2: GO-Canada riometer site abbreviation code, location, and geodetic coordinates.

Data from GO riometers was showcased in Section 3.2.1. The riometer at *pgeo* was used to showcase a quiet day's data, shown in Figure 3.4, while that at *rank* was used to showcase solar radio bursts in Figure 3.5. The analog GO riometers are used to aid in the analysis in Chapter 4 and to perform the statistical analysis in Chapter 5.

### 3.2.4 Event Signatures in Riometer Data

There is great variability in the temporal and spatial signatures of different geomagnetic and solar disturbances in terms of their effects on HF radio propagation. To familiarize the reader with events relevant to this research, I here present a detailed description of two of the major event types and their signature in riometer data. The spatial structure of different events, and specifically that of SWF, is important for the work presented in Chapter 4. The temporal evolution and spatial variability of AA events is relevant to both Chapters 4 and 5.

#### Short Wave Fadeout

SWF, previously described in Section 2.4.1, has a distinct short-lived signature in riometer data, typically lasting some tens of minutes after the radiation had reached the Earth. Figure 3.8 shows an example of a class M flare, which occurred on 7 May 2024, as observed in the HSRs at PFRR and PGEO as well as the GO-Canada riometers at *daws*, *rank*, and *gill*. The XRF reached  $8.3 \times 10^{-5}$  W/m<sup>2</sup>, indicating an M8.3 level flare. The 30 MHz signal from the HSRs is used in tandem with that of the analog, GO riometers to explore the signature of the ensuing SWF.

The signal attenuation is abrupt, followed by gradual recovery. Absorption is coincident at all riometers and follows the same temporal structure. However, the magnitude of the absorption decreases with proximity to the solar terminator. In other words, higher solar-zenith angles (the angle from zenith to the Sun) correspond with lower absorption at the time of the event. PFRR and *daws* incur the least absorption, while *gill* incurs the maximum absorption, having the lowest solar zenith angle, as indicated by the reduction in raw signal levels. To note is the difficulty in comparing HSRs to GO riometers, if one inquires about the relative magnitude of absorption, since these are raw signal levels. However, one can compare, say, the raw signal at PGEO relative to that in PFRR, or that at *daws* relative to that at *gill*, to get a sense of the relative absorption.

#### Auroral Absorption

There is a high degree of variability in the signature of AA in riometer data, as many mechanisms allow for high-energy particle precipitation from the magnetosphere (Baker et al., 1981; Berkey et al., 1974; Clilverd et al., 2008; Pudovkin et al., 1968). Additionally, the precipitating particles can be further energized via acceleration mechanisms, the dynamics of which are still being studied at the time of this writing (Akasofu, 1981; Baker et al., 2019). These particles can reach relativistic energies, penetrating to deeper altitudes,

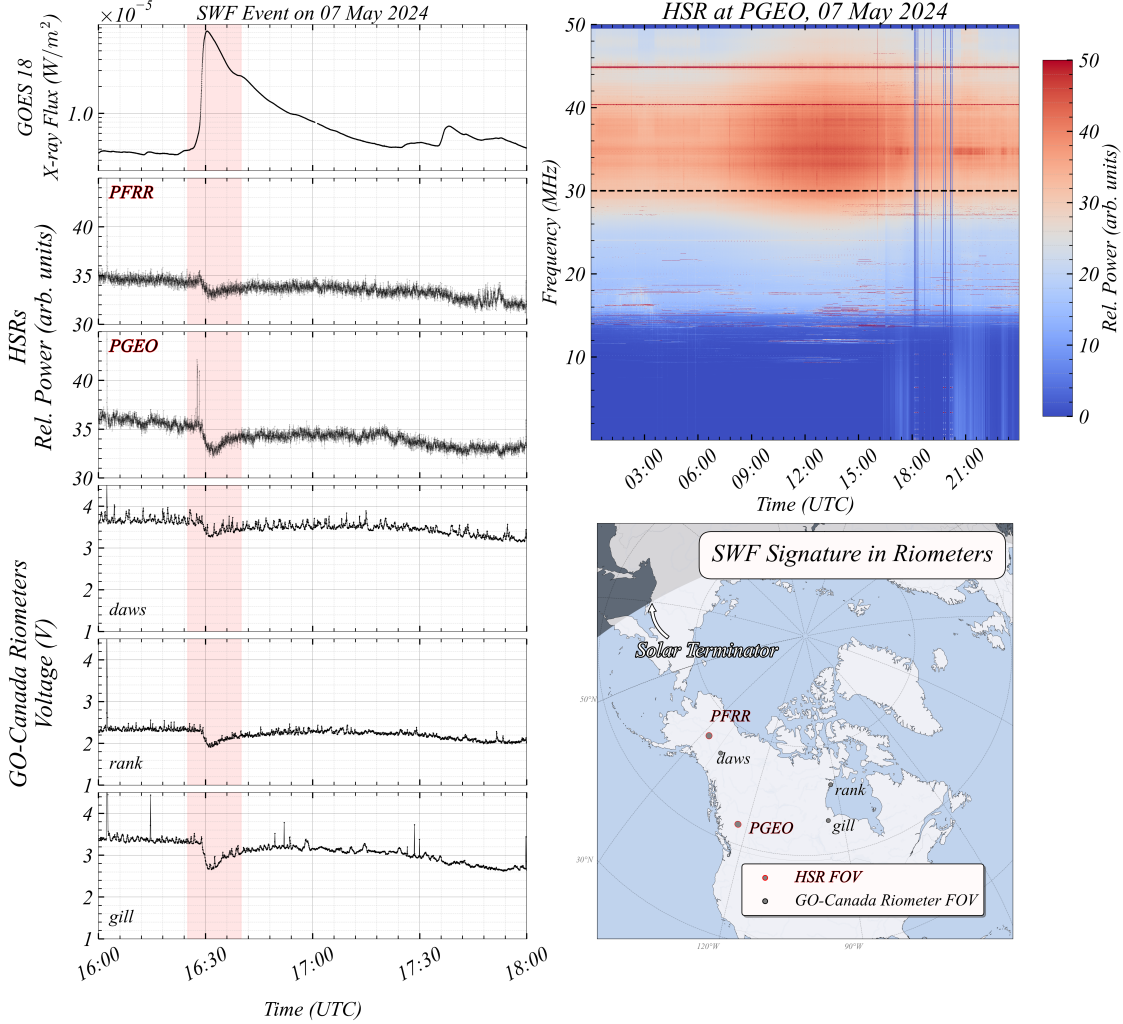


Figure 3.8: The signature of SWF in riometer data. The top right panel shows the HSR full spectrum data from 7 May 2024. On the left, from the top down are plots for solar X-ray flux from GOES, the 30 MHz signal levels for the HSRs at Poler Flat (PFRR) and Prince George (PGEO), followed by the GO-Canada riometer voltage levels at Lake Dawson (daws), Rankin Inlet (rank) and (gill), for a period of time surrounding the SWF event, highlighted in red. The 30 MHz signal for PGEO is indicated by a dashed line on the full spectrogram. In the bottom right is a map showing where each riometer is located in relation to the solar terminator.

effectively decreasing the lowermost boundary of the D-region.

CNA events have traditionally been distinguished based on their occurrence in different Magnetic Local Time (MLT) sectors. Magnetic midnight would be the point on Earth corresponding to  $180^\circ$  of magnetic longitude away from the subsolar point. In other words, when the magnetic pole (which is not colocated with the geographic pole) is directly between an observer and the Sun, the observer's location corresponds to magnetic midnight, or 0 MLT. 6, 12, and 18 MLT correspond to magnetic dawn, noon, and dusk, respectively.

tively. For a detailed explanation of magnetic coordinate systems, see Laundal and Richmond (2017) and references therein.

Many CNA events occur near magnetic midnight, as that is often where electrons are injected into the ionosphere (Berkey et al., 1974; J. Hargreaves, 1968, 1969). These injected electrons drift eastward due to the geomagnetic trap and may gain energy during transport. Though, there are some CNA events where absorption expands westward instead of eastward (Berkey et al., 1974; Birch et al., 2013; J. Hargreaves, 1968; Jones et al., 2011; Kainuma et al., 2001). Expansion velocities of absorption patches (patches of enhanced electron density may appear at different radar or riometer sites with a characteristic time-delay, which can be inverted into velocities) are sometimes inconsistent with gradient-curvature drifts expected of the trapped electrons—serving as evidence to the energization of the drifting particles (Berkey et al., 1974; Birch et al., 2013; Burns et al., 1990; Kainuma et al., 2001; Kikuchi et al., 1990).

Riometers on the dayside ionosphere may observe different signatures, due to the hardened spectra of the precipitating electrons there (Abdu, 1971; Kavanagh et al., 2002). Furthermore, there tends to be more pulsating auroral structures closer to the dawn rather than the dusk sector (Jones et al., 2011; Oguti, 1981). Some studies report that absorption patches on the dayside are observed to expand poleward, on the average, as opposed to equatorward on the nightside (Kainuma et al., 2001; Kikuchi et al., 1990). However, grouping events in different MLT sectors still shows great variability (Kainuma et al., 2001). The dependence of AA on geomagnetic and solar wind parameters (Kavanagh et al., 2004) further complicates the issue of categorizing events.

While we can classify many events, some are outliers (Berkey et al., 1974; Collis et al., 1996). One peculiar outlier event, showcased in a study by Collis (Collis et al., 1996), shows a co-rotating absorption patch that lingered for about two hours within the riometer’s FOV. Using radar measurements, the authors confirmed electron density enhancements peaking at 67 km altitude, which is unusually low, and that 50% of the total radiowave absorption occurred below 73 km.

The above literature highlights the difficulty in categorizing AA signatures as observed in riometers, with the exception of what came to be known as the “spike” event (Aminaei et al., 2006; J. K. Hargreaves, 1980; J. K. Hargreaves et al., 2001; Spanswick et al., 2005). Night-time spike events are perhaps the most understood and delineated as highly localized and elliptical, with roughly 200 by 80 kilometers in the major and minor axes, respectively (J. Hargreaves et al., 1979; J. K. Hargreaves et al., 1991, 1997). In addition

to the riometer spike, isolated injection signatures have been clearly identified Spanswick, Donovan, Friedel, and Korth (2007). Spanswick et al. (2005) offers a comprehensive study on spike and injection signatures in riometer data. The difficulty arises when distinguishing between events. Interpretations of the event depends on the feature being studied (e.g., whether one is looking at the absorption onset or individual peaks that follow) and it is often difficult to distinguish between individual events versus intensifications that resemble continuing activity (J. Hargreaves & Devlin, 1990). Finally, absorption can come in patches that cross the FOV of riometers, and which could be separated by hundreds of kilometers (Birch et al., 2013).

An example of the signature of AA is illustrated in Figure 3.9, for an event on 13 May 2024. The abrupt increase in riometer absorption signifies high-energy electrons injected into the ionosphere at 3:00 UTC at (or near) *gill*, followed by *chur*, *rabb* and *fsmi*. No activity appears to be taking place at PFRR nor *daws*, and very minor activity is present at the PGEO HSR or *pgeo*, the colocated GO riometer. The absorption seems not to reach that far. For the affected sites, more absorption follows the initial onset– that is the sporadic nature of AA. A spike at *rank* seems isolated from the initial absorption. Another spike occurs at *fsmi*, though much later. A spike at *gill* is also observed, albeit hidden within the overall injection. The reader is referred to Spanswick et al. (2005) for a comprehensive interpretation of these signatures. Here, I would like to emphasize a few points relevant to the work in later chapters:

1. AA is sporadic, both temporally and spatially.
2. A riometer detects the event onset via large reductions in signal level (or large absorption after baselining).

These signatures delineate the complicated nature of AA and the variability between different AA events, which I shall make reference to in the work presented in later chapters.

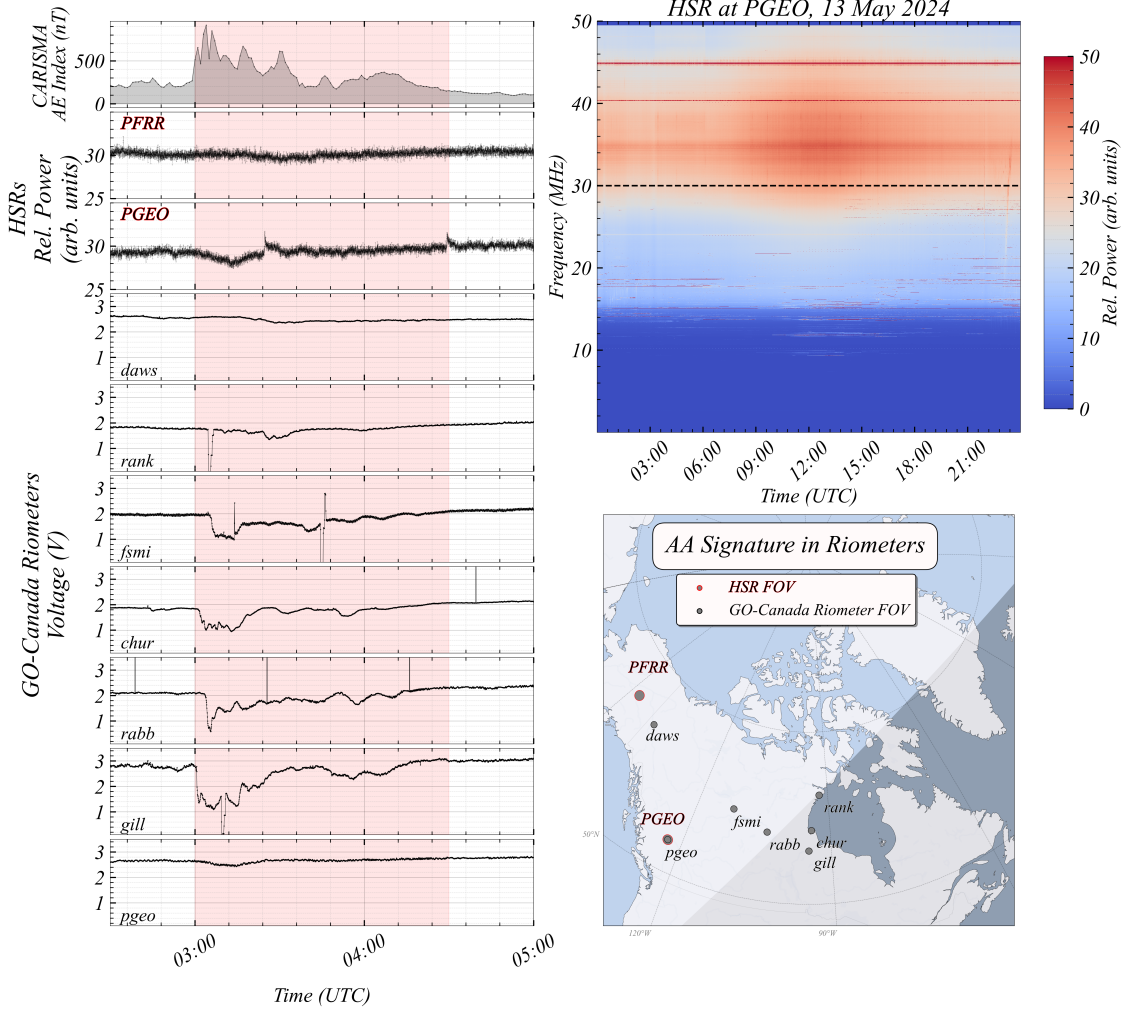


Figure 3.9: The signature of AA in riometer data. On the top right is the PGEO HSR full spectrum data, with power at 30 MHz indicated using the black dashed line. On the left, from the top down are the CARISMA AE index values, then the PFRR and PGEO HSR signal levels at 30 MHz, followed by the 30 MHz voltage levels for the GO riometers at *daws*, *rank*, *fsmi*, *chur*, *rabb*, *gill*, and *pgeo*, in that order, for the time of the event. The rise in AE index correlates with the activity, as indicated by the event time, highlighted in red. At the bottom right is a map to facilitate an understanding of the temporal and spatial signatures of the AA. The solar terminator is marked by the shaded region.

### 3.3 High-Frequency Radio Transmitters and Receivers

In addition to riometers, this thesis leverages the existence of multiple transmitter networks. In this section, I introduce all transmitters and receivers employed in the analysis. A map of all the transmitters and receivers used is shown in Figure 3.10. I shall introduce the instrumentation belonging to Natural Resources Canada (NRCan), National Institute for Standards and Technology (NIST), and National Research Council (NRC), in that order.

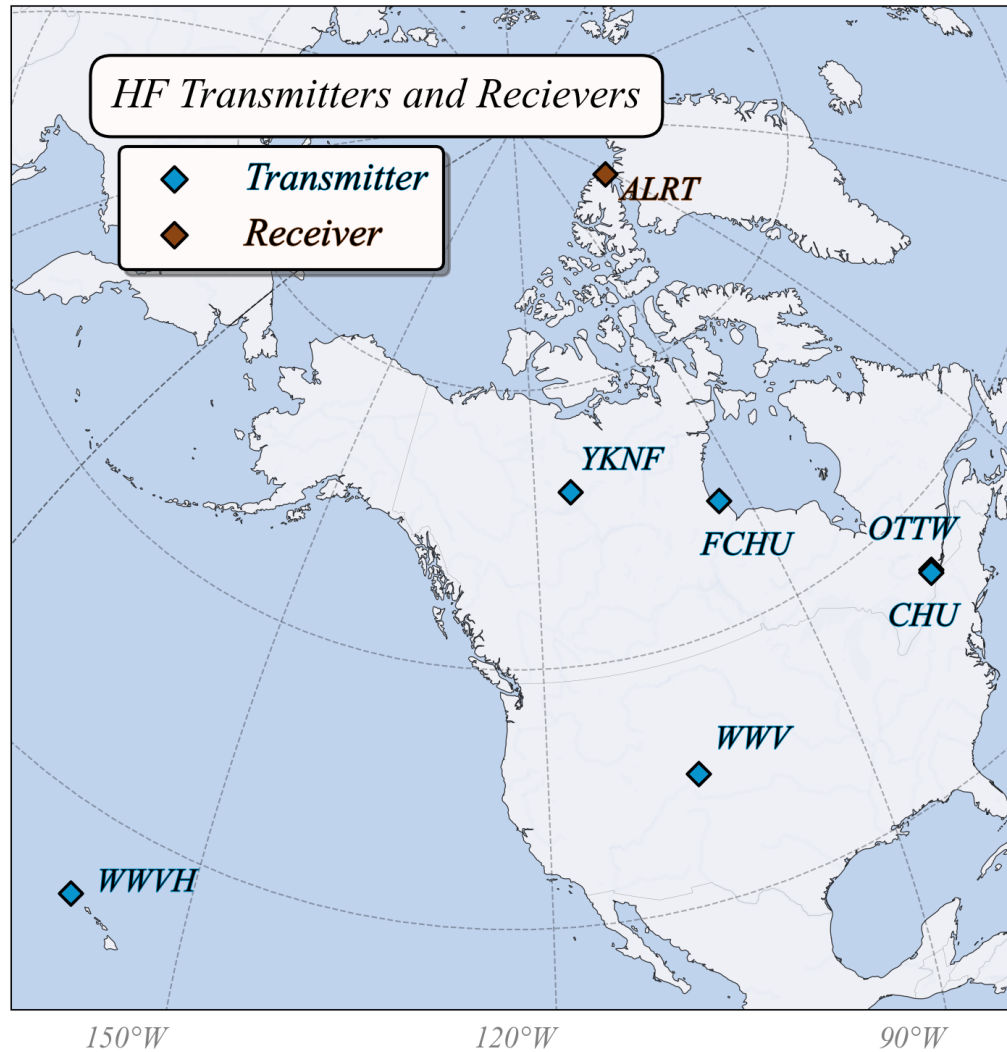


Figure 3.10: Map showing all HF transmitters and receivers used. Exact locations of the corresponding site codes, shown here, are listed in Tables 3.3, 3.5, and 3.4. NRCan's transmitter at Ottawa (OTTW) is close to NRC's CHU transmitter, hence they overlap on the map due to proximity.

### 3.3.1 Natural Resources Canada Network

A few transmitters have been used in this thesis. First is a network of low-power (500 W), omni-directional transmitters operated by Natural Resources Canada (NRCan), located in Ottawa (OTTW), Yellowknife (YKNF), and Fort Churchill (FCHU). Details about the location of these transmitters is provided in Table 3.3. These transmitters operate at 5.3820, 6.9285, 8.0995, 10.4220, 11.1070 and 14.3644 MHz, cycling through all 6 frequencies on a prearranged schedule that repeats every 7.5 minutes (Cameron et al., 2021). Having a staggered schedule allows confirmation of signal reception at a given frequency.

#### Natural Resources Canada (NRCan) Instrumentation

Site Code	Location	Geodetic Latitude (°)	Geodetic Longitude (°)
<b>Transmitters</b>			
YKNF	Yellowknife, Northwest Territories	62.48	-114.48
FCHU	Fort Churchill, Manitoba	58.74	-93.82
OTTW	Ottawa, Ontario	45.41	-75.55
<b>Receiver</b>			
ALRT	Alert, Nunavut	82.51	-62.35

Table 3.3: NRCan network of transmitters and their receiver at Alert. Given are each instrument's site code, location and coordinates.

#### Alert Receiver Data

Data from the receiver at Alert, Nunavut has also been used in this thesis. The radio data includes parameters such as elevation, azimuth, Signal-to-Noise Ratio (SNR) and time of flight. An example of the SNR data is shown in Figure 3.11. One clearly observes the diurnal variation of LUF and MUF as the 8.0995 MHz transmissions represent a transition from night-time propagation to day-time propagation. 10.4220 MHz (or higher-frequency) transmissions are strictly daytime.

The ALRT data used here spans December 2013 to October 2019. Figure 3.12 shows the data availability for the year 2014. A day with available data is shown in orange. Within a day, a reception is marked as a dark brown dot. Dots closer to 0 UTC are at the bottom of the day. Since dawn at ALRT occurs at about 11 UTC, one can see the diurnal variation of signal reception and even seasonal variation can be gleaned from this data. More signal loss for the lower frequency (5.382 and 6.0995 MHz) transmissions occurs near the summer solstice (from either end), closer to July. Because each reception implies that the Binary Phase Shift Keying (a type of modulation) signal from OTTW has been successfully decoded (demodulated) at

*Signal-to-Noise Ratio: Ott-Alert Link, 2019-09-21*

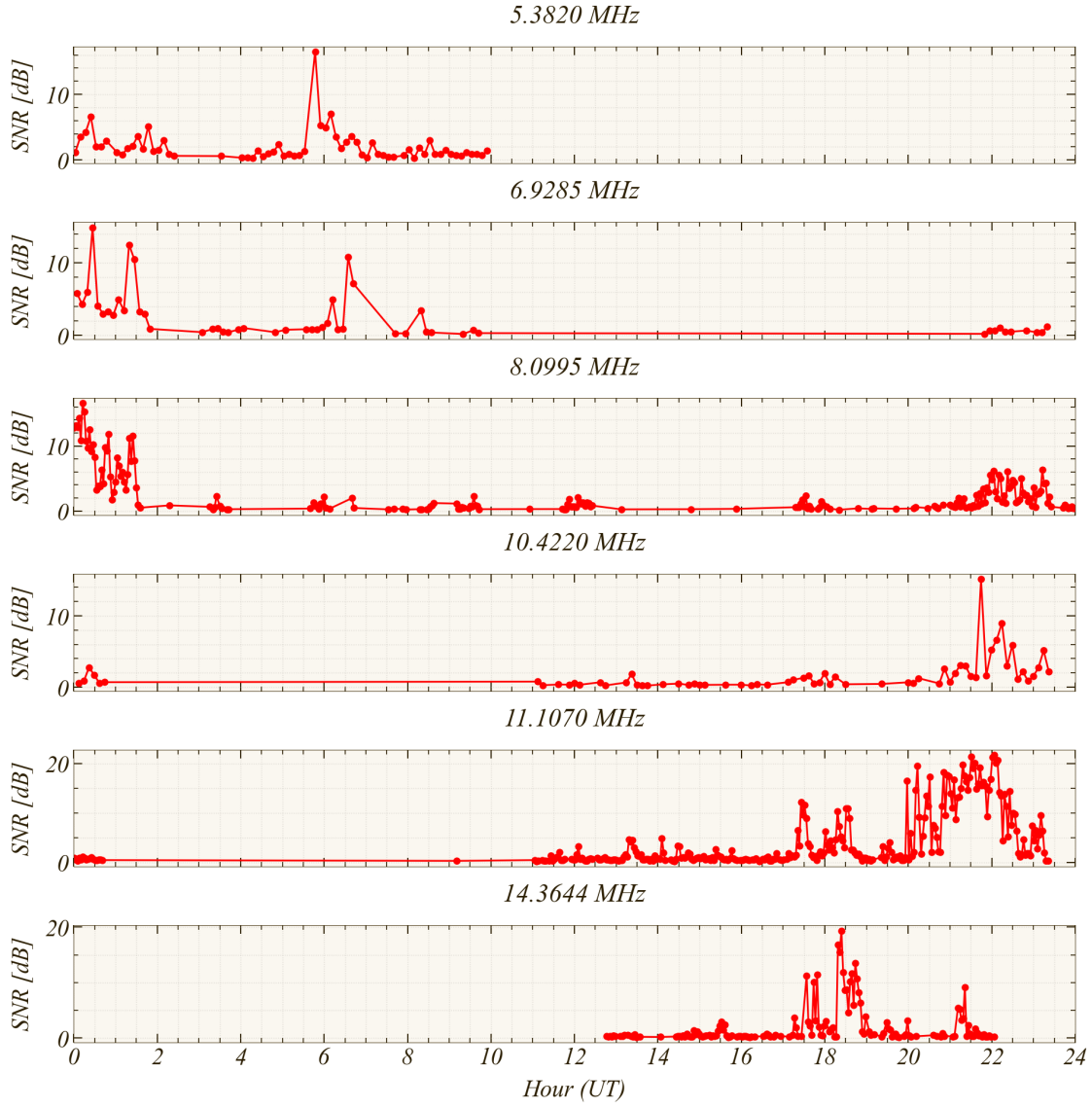


Figure 3.11: Figure showing the SNR for the NRCan transmission frequencies as a function of time, as observed in the ALRT receiver data for the 21<sup>st</sup> of September, 2019.

ALRT, this data availability plot shows receptions, which I shall rely heavily on in my analysis in Chapter 5.

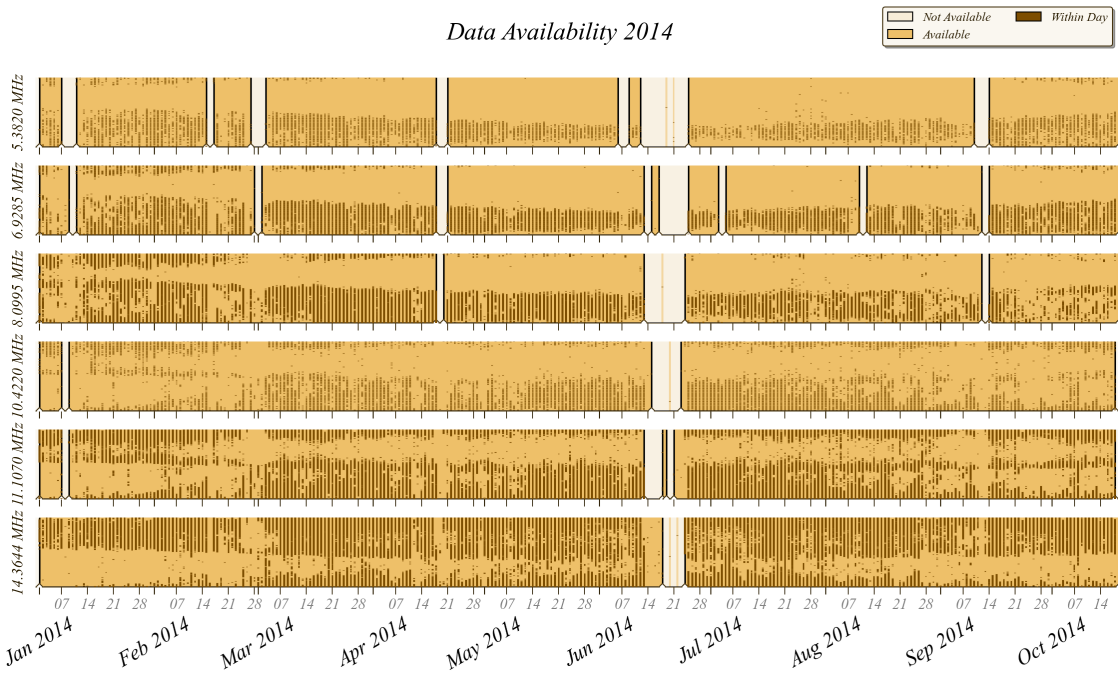


Figure 3.12: Data availability for the HF radio dataset for the OTTW to ALRT link for the year 2014. Brown dots within each day imply a signal was received and successfully decoded. If a day is totally missing data, it is marked by white. A day with even one reception is marked orange. Receptions vary by frequency, time of day, and season.

### 3.3.2 Timing-Signal Transmitters

Timing-signal transmitters were also utilized in this thesis. The National Research Council's (NRC) CHU transmitter (Canada, 2019) is located close to NRCan's OTTW transmitter. The CHU transmitter (where CHU is simply the call sign) operates at 3.33 and 14.67 MHz at 3 kW and at 7.85 MHz at 5 kW.

#### National Research Council (NRC) Transmitter

Site Code	Location	Geodetic Latitude (°)	Geodetic Longitude (°)
CHU	Ottawa, Ontario	45.30	-75.76

Table 3.4: NRC's Transmitter site code, location, and coordinates.

In addition, the National Institute of Standards and Technology (NIST) has two high-power transmitters sending timing signals, located in Boulder, Colorado (call sign WWV) and Kauai, Hawaii (call sign WWVH) (Nelson et al., 2005). Both WWV and WWVH operate at 5, 10, and 15 MHz at 10 kW. WWV additionally transmits at 2.5, 20, and 25 MHz, albeit at 2.5 kW radiated power, and WWVH transmits at 2.5 MHz at 5 kW (see <https://www.nist.gov/pml/time-and-frequency-division/time-distribution/radio-station-wwv>).

These high power transmitters are discussed in more detail in Section 4.4.1.

#### National Institute of Standards and Techonology (NIST) Transmitters

Site Code	Location	Geodetic Latitude (°)	Geodetic Longitude (°)
WWV	Boulder, Colorado	40.43	-105.68
WWVH	Kawai, Hawaii	21.98	-159.75

Table 3.5: NIST Trasnsmitter site codes, location and coordinates.

# Chapter 4

## Remote Sensing Electron Density Enhancements

This chapter contains the results and methodology published in (Ghaly et al., 2024). Here, I represent a more narrative form of this analysis with additional information for the reader.

### 4.1 Motivation and Goal

The HSRs, introduced in Section 3.2.2, contained a wealth of information regarding terrestrial transmissions that propagate to the instrument (via skywave), which presented an opportunity for studying CNA events from a different perspective. During the testing phase of the prototype HSRs, some CNA events, characterized by absorption in the 25–50 MHz band, were observed to occur simultaneously with loss of terrestrial transmissions in the lower frequencies, under  $\sim 25$  MHz. One such example is presented in Figure 4.1. The onset of the absorption event, indicated by the large reduction in signal level at 30 MHz (panel B in Figure 4.1), and marked by the dashed lines, is coincident with loss of terrestrial transmissions as shown in the inset axis, spanning signals in the 1–21 MHz range. Signals of different frequencies and origin should, in theory, be affected differently. However, the broad range of frequencies impacted at the riometer site indicates some local processes responsible for the loss. Furthermore, the presence of many such events, at different levels of solar and geomagnetic activity, observed across the prototype HSR network, motivated an investigation of the spatial extent of the local areas impacted electron density enhancements. Examples of these events are presented in Figure 4.2. The times highlighted in gray indicate CNA coincident with loss of terrestrial transmissions.

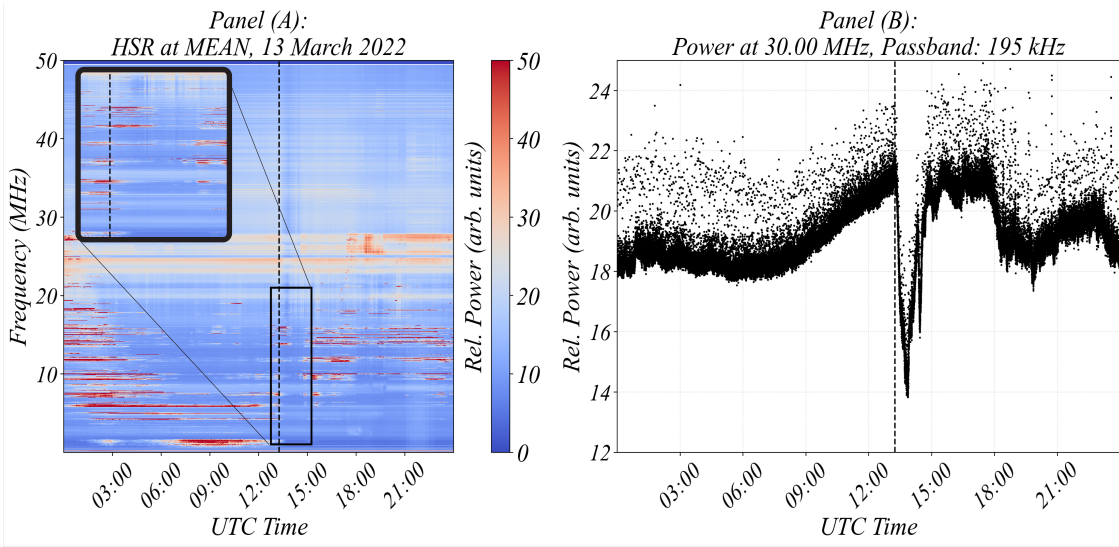


Figure 4.1: Riometer measurements from Meanook (MEAN) on 13 March 2022. Panel (A) (left) shows the full spectrum, from 0.01–49.50 MHz. An absorption event (loss of HF power) marked with a vertical dashed line begins at approximately 13:15 UT. The sub-panel shows the distinct loss of terrestrial HF signals at the dashed line. The inset axis shows power for signals with frequencies ranging from 1 to 21 MHz. Panel (B) is the equivalent riometer signal of a 30 MHz, single channel riometer, derived from the multi-frequency data. The cosmic absorption is marked with the same dashed line.

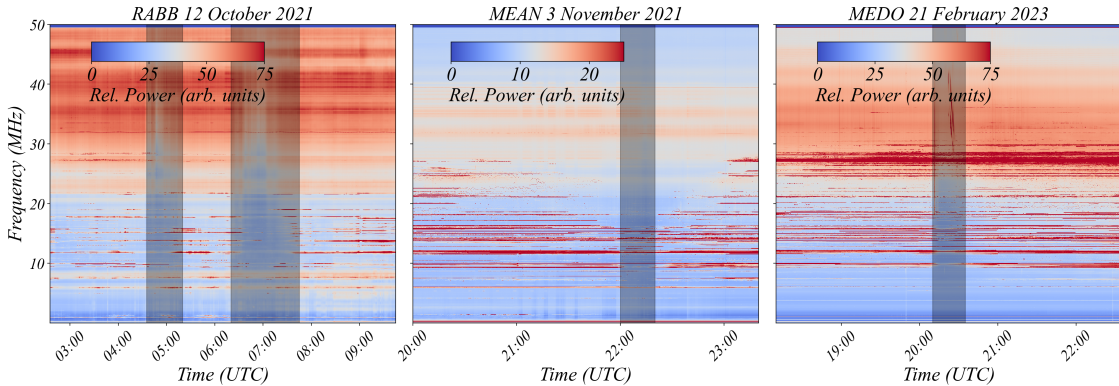


Figure 4.2: Example events from each of the HSRs from the prototype network. Highlighted in gray are times when CNA was simultaneous with loss of terrestrial signals. I focus on MEDO 21 February 2023 (right-most plot) for applying our methodology.

Such events indicate an ionospheric reconfiguration where the lower-frequency, sky-wave, terrestrial, signals are impacted at the same time as the higher-frequency, cosmic signals, emanating from the Galaxy. This correlation had been previously documented and reported in the literature (J. Hargreaves, 1969; Hunsucker & Hargreaves, 2003; S. Milan et al., 1994; S. E. Milan et al., 1998; Uryadov et al., 2019). Here, I aim to utilize the simultaneous absorption to estimate the size of the absorbing region in the proximity of the HSR.

## 4.2 Sources of Electron Density Enhancements

As discussed in Section 2.4, D-region electron density enhancements, leading to radiowave absorption, can be driven by ionization due to radiation (for example due to a strong solar flare or Bremsstrahlung radiation) or precipitation mechanisms associated with the magnetospheric particle population.

Following a solar flare, radiation in the Extreme Ultra-Violet and X-ray bands ionizes the sun-lit D-region, leading to SWF. The magnitude of the resulting radiowave absorption will depend on operating frequency, solar-zenith angle, and the magnitude of the flare (Davies, 1990). Thus, areas further away from the subsolar point are less impacted. During some strong flares, protons ejected from the Sun are allowed to precipitate into the ionosphere, leading to PCA. The precipitation starts at the poles and expands to cover the polar cap. The polar cap itself will expand equator-ward, with the flux and energy of the protons determining the precipitation area (Yakovchuk & Wissing, 2023). However, at the end of the PCA event, auroral electrons are likely to incur AA (Hunsucker & Hargreaves, 2003), the spatial extent of which depends on the kind of event being studied. Early observations summarized by Hunsucker and Hargreaves (2003) show no general consensus on the size of the absorption region across different events, with results ranging from 10 to 800 km and 90 to 800 km in the North–South and East–West directions, respectively, as well as high variability between the results. Furthermore, there are finer structures of absorption, on the order of a few 100 km, in both the North–South and East–West directions. The plethora of magnetospheric precipitation mechanisms convolved with magnetospheric energization and transport leads to significant variability between events in terms of signatures observed in riometers (Berkey et al., 1974; Jones et al., 2011), even when grouped by their occurrence in different Magnetic Local Time (MLT) sectors (Kainuma et al., 2001). Even within the morning sector, there seems to be high variability in terms of absorption patch shape, elongation dimension, and drift direction (Makarevitch et al., 2004). The complexities and variability of absorption events highlight the importance of observations that can resolve spatial structuring in D-region electron density enhancements.

A recent study by Bland, Tesema, and Partamies (2021) probing the area impacted by D-region enhancements via attenuation in Super Dual Auroral Radar Network (a network of radars that relies on backscatter) echoes at 10–11 MHz indicates a spatial extent of over at least  $4^\circ$  magnetic latitude, and on average, 4–5 hours of MLT. Bland, Bozóki, and Partamies (2022) extended this analysis in a case study using a multi-instrument approach and showed that the region impacted by D-region electron density enhancements can extend much further in latitude range ( $\gtrapprox 10^\circ$ ). These studies showed that the latitudinal limits of the absorption region extend much further both poleward and equatorward than previously predicted by models

(Cresswell-Moorcock et al., 2013; van de Kamp et al., 2018).

### 4.3 Project Outline

The goal of this project is to map the geographic area of the absorbing layer. To that end, I start by analyzing events such as the ones described above, where CNA is simultaneous with HF signal loss. I then leverage the existence of some known HF transmitter networks and identify their signals in our data (Section 4.4.1). After confirming signal reception, and given that the signal is lost at the onset of the absorption event, I perform ray tracing simulations to find where the signal was lost (Section 4.6). The points where the signal loss occurs are called the pierce points (where the ray enters the assumed D-layer responsible for the absorption). These pierce points constitute a map of the area impacted by D-region enhancements and causing HF terrestrial signal loss.

## 4.4 Methodology

### 4.4.1 Identifying the Source of Terrestrial HF Signals

The presence of CNA indicates enhanced D-region electron density within the vicinity of the HSR. Since the terrestrial transmissions are absorbed simultaneously, I assume that both are impacted by the same D-region absorption. The absorption region can thus extend beyond the nominal FOV of the HSR, to where the terrestrial signals were lost. Since the origin of a terrestrial transmission limits the paths by which a signal can reach the HSR, identifying that source is a first step towards extending our map of the absorbing region. Utilizing the available frequency allocation information for transmitters in Canada and the United States (see [https://sms-sgs.ic.gc.ca/eic/site/sms-sgs-prod.nsf/eng/h\\_00010.html](https://sms-sgs.ic.gc.ca/eic/site/sms-sgs-prod.nsf/eng/h_00010.html) and <https://www.ntia.doc.gov/category/spectrum-management>, respectively) and analysis of the temporal behavior of the acquired power (matching chirp patterns of known transmitters), it is possible to confirm some signal sources within the lower frequency riometer data, facilitating the study presented here.

#### Natural Resources Canada Network of Transmitters

First, I leverage the existence of the NRCan network of transmitters, introduced in Section 3.3, with installations (at the time of this analysis) in Ottawa (OTTW), Yellowknife (YKNF) and Fort Churchill (FCHU). Exact locations as well as a map of those transmitters is provided in Table 3.3 and **3.10** in Section 3.3.1. These transmitters operate at 5.3820, 6.9285, 8.0995, 10.4220, 11.1070 and 14.3644 MHz, cycling through all 6 frequencies on a prearranged schedule that repeats every 7.5 minutes (Cameron et al., 2021). I can identify these signals in HSR data based on their transmission schedule. For 5 March 2022, the schedule is given in Table 4.1.

Frequency (MHz)	Transmission Start Time (UTC)							
	YKNF			FCHU			OTTW	
5.3820	01:55			02:05				
6.9285	04:25			04:35				
8.0995	00:00	02:30	05:00	00:10	02:40	05:10	00:15	02:45
10.4220	06:55			07:05				
11.1070	00:35	03:05	05:35	00:45	03:15	05:45	00:50	03:20
14.3644	01:10	03:40	06:10	01:20	03:50	06:20	01:25	03:55

Table 4.1: NRCan transmission schedule active during 5 March 2022. The transmission start times are staggered. Yellowknife (YKNF) is always ahead of Fort Churchill (FCHU), which is ahead of Ottawa (OTTW). This schedule starts at the beginning of each hour and repeats every 7.5 minutes (resulting in 8 cycles every hour). During this time OTTW was not transmitting at both 5.3820 and 6.9285 MHz.

Figure 4.3 shows 22.5 minutes of HSR data from RABB for a single frequency bin, 5.37–5.39 MHz taken on 5 March 2022. The only listed active transmitters in this frequency band are associated with the NRCan transmitter network. During this timeframe, the YKNF and FCHU transmitters were active with offset transmission schedules. The transmission schedule active during 5 March 2022 is shown in Table 4.1. YKNF and FCHU start transmitting at 01:55 and 02:05 at the start of every UTC hour, repeating every 7.5 minutes and resulting in 8 cycles every hour. Within each cycle the YKNF transmitter produces two half-second pulses, two seconds apart, followed, 6 seconds later, by the FCHU transmitter, which transmits a single, half second pulse followed by a two-second Barker code transmission one second later. I note the FCHU transmitter clock was not GPS locked during this interval, so the timing of the pulse is less precise than YKNF. The times of the known transmissions are indicated in Figure 3 with dashed vertical lines (black lines indicate the schedule of YKNF and red indicates the schedule for FCHU). Individual power levels in the 5.37–5.39 MHz band (one per second) recorded by the HSR are shown as black dots.

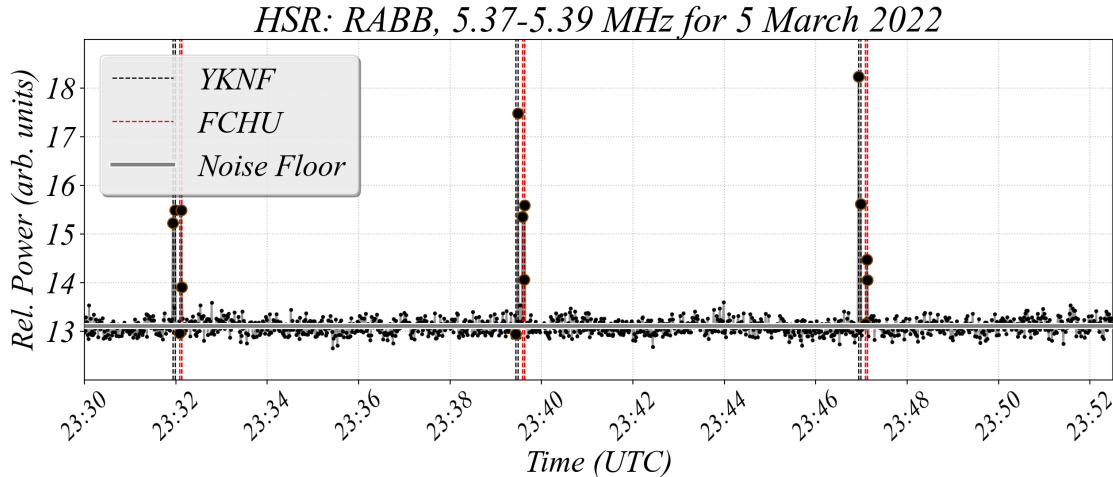


Figure 4.3: One-second power measurements from the HSR at Rabbit Lake (RABB) in the 5.37–5.39 MHz frequency range (black dots). Times of the 5.382 MHz transmissions from the NRCan transmitters at Yellowknife (YKNF) and Fort Churchill (FCHU) are shown as vertical lines (black and red, respectively). The noise floor at this frequency, for this period, is indicated with the horizontal gray line.

HSR power measurements in this band are seen to increase well above the noise floor (indicated with a gray line and calculated as the 10th percentile of power measurements during the 22.5-minute period shown) during the times the YKNF and FCHU transmitters are scheduled to transmit. If the riometer measures an increase in power consistent with the known transmission schedule (as shown above), I argue that this is evidence that the riometer is, in fact, receiving the skywave mode transmission from (in this case) YKNF and FCHU. I note that the exact timing and length of the pulses is limited by the riometer data acquisition

cycle, which integrates over one-second periods. If the 0.5s pulse is misaligned with the acquisition cycle, the riometer power increase will be observed across two temporal samples and in general have less power in each sample.

To further explore the HSR response to the known NRCan signals, I perform a superposed epoch analysis of the HSR power, relative to the known transmission time. In Figure 4.4, 4 hours of riometer data are analyzed. The data are time-shifted so that each transmission cycle (as shown in Table 2) starts at the YKNF transmission (second 00:00 in Figure 4.4). This was done to examine all the pulses from the NRCan transmitters during this time and confirm that each transmission was received at the appropriate time. Over the 4-hour period shown, 32 transmission cycles are considered. Figure 4 shows distinct peaks in average riometer power from 0–1 s and 3–4 s following the known NRCan pulse transmissions from YKNF, followed by a lower power peak associated with the FCHU transmission cycle. The average (mean) power in this case is taken across transmission cycles.

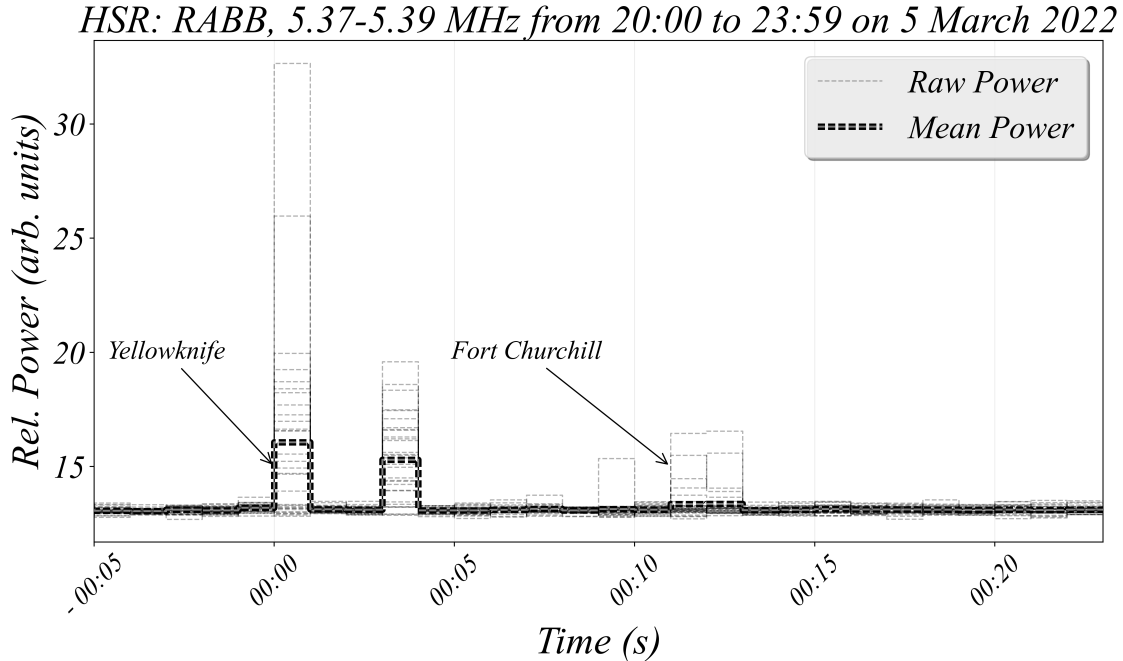


Figure 4.4: Superposed epoch analysis of riometer power at Rabbit Lake (RABB) in the 5.37–5.39 MHz band for 32 successive NRCan transmission cycles. Zero time is the time of the Yellowknife transmission. The timing of the Fort Churchill transmissions within the cycle is also shown. Churchill transmits 10 seconds after Yellowknife (1st transmission).

The above analysis shows that the riometer response in terrestrial bands associated with the NRCan transmission cycle matches the transmission schedule. The peaks in observed power align with the prescribed NRCan transmission cycle (see Table 4.1). This provides confidence for interpreting the geographic origin of

signals based on timing. Based on this, I assert that the temporal match between enhanced riometer power within a single riometer frequency bin, and the known schedule for transmissions within that frequency band is evidence that the riometer received a signal from that source location. In the case highlighted in Figure 4.4, I argue that the HSR at RABB received the YKNF and FCHU transmissions. If the transmitter sequence is unknown, then the argument for conclusive reception of a signal becomes weaker. In these cases, I solely rely on the list of registered transmitters and their self-declared transmission power. Such is the case for high-power, timing signals.

### High-Power Timing Signals

I also utilize some high-power timing-signal transmitters located in Canada and the United States, introduced previously in Section 3.3.2. Exact locations of these transmitters is listed in Tables 3.4 and **3.5**, and shown in a map in Figure 3.10. These timing-signal transmitters encode a sequence of tones that can be decoded, given a sufficiently high sampling rate at the receiver. Since the HSRs are limited to a  $\sim 1$  s measurement cadence (integration time of power measurements), we must solely rely on signal power as a function of time. Fortunately, these transmitters have high radiated power and their signals are observed almost continuously in HSR data during their expected times (e.g., the diurnal variation explained in Section 3.2.2). Furthermore, any absorption due to solar or geomagnetic events decreases the received power substantially such that signal loss can be easily distinguishable.

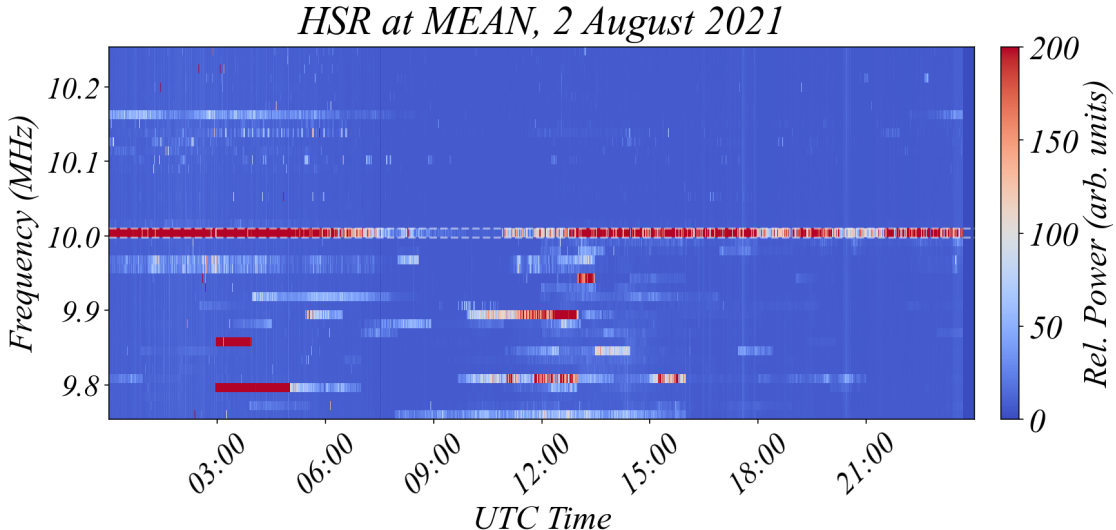


Figure 4.5: Example riometer spectrum from Meanook (MEAN) for, 2 August 2021, showing the frequency range 9.75 to 10.25 MHz. The WWV/WWVH transmission at 10.00 MHz is identified (bordered by white dashed lines)

Figure 4.5 shows an example for the continuous, high-power, WWV/WWVH transmissions in the 10 MHz band, for which the HSR at MEAN observe near-continuous power above the noise floor. Around local midnight (6 UTC), the 10 MHz band is no longer supported and ceases to propagate to the HSR. Fluctuations in signal level towards the end of the day are due to absorption, occurring around 18 and 20 UTC.

#### 4.4.2 Ray Tracing

As described above, it is possible to identify the status of a few HF links within the HSR data. For NRCAn transmitters, we identify the signal based on the known transmission schedule and frequencies. For other transmitters, namely WWV, WWVH and CHU, I rely on monitoring the power within an appropriate frequency band.

I note that while a matching signal sequence (meaning riometer power mimics the transmitter schedule) is argued here as conclusive evidence of an available HF link, the reverse is not necessarily true. A lack of signal acquisition in the riometer, in general, cannot be strictly interpreted as an unavailable link. There are many reasons why the riometer would not receive a particular HF signal, most notably that the signal was not transmitted. Since I cannot confirm that signals are transmitted, I restrict myself, here, to times in which the riometer has acquired the signal, then lost the signal, then reacquired the signal. In these cases, I argue that the loss was not due to lack of transmission, but rather changes to the HF propagation environment.

In this study I am concentrating on events in which terrestrial signal loss is observed simultaneously with CNA. Under these conditions, the CNA provides critical information about the state of the D-region. The subsequent enhancement of D-region electron density is nominally assumed to be at altitudes of 70–100 km. During a time of coincident CNA and terrestrial signal loss, I therefore attribute the terrestrial loss to an enhanced electron density layer overhead at the riometer location. We assert this is reasonable due to the simultaneity of the response seen in the data. To note, for NRCAn signals, I am limited by the maximum time between successive transmissions, which is a function of frequency (450 seconds for 5.382, 6.9285 and 10.422 MHz but 210 seconds for 8.0995, 11.107 and 14.3644 MHz—see Table 4.1). The high-power timing signals observed power levels fluctuate significantly at the 1s resolution of the HSRs, similar to the power at 30 MHz, but, when averaged over a minute, both show simultaneous reductions in power level.

The assumption for enhanced electron density overhead the instrument is also supported by the fact that radio wave absorption is proportional to the inverse of the square of the signal frequency (see equation 2.32). For example, if there are 3 dB of absorption at 30 MHz (in the cosmic band), one would expect 108 dB of absorption at 5 MHz if the signals are transiting the same region (our primary assumption). Additionally, while most signals in the 30 MHz band are extra-terrestrial and trans-ionospheric, the double (or multiple) traversal of low-frequency HF signals of the D region, combined with their oblique trajectories in that region on their way to the riometer, results in higher absorption (J. Hargreaves, 1969). The broad frequency range

of the signal losses (see Figure 4.2) also adds credibility to our assumption, since if terrestrial loss were associated with effects further away, we would anticipate some signals remaining in the riometer measurements during the event (since they are coming from other directions).

Under the assumption that a single layer of enhanced electron density is responsible for both the CNA and terrestrial loss, we utilize ray-path simulations to model where the signals encounter this layer. To demonstrate, we perform ray traces for the event on 21 February 2023– rightmost event in Figure 4.2. Figure 4.6 shows an example ray-path simulation for one known signal, the 15 MHz signal from the WWV transmitter observed in the MEDO HSR. Utilizing electron density profiles from the International Reference Ionosphere model (IRI) (Froí et al., 2020) and the Provision of High-Frequency Raytracing Laboratory for Propagation Studies toolbox (see <https://www.dst.defence.gov.au/our-technologies/pharlap-provision-high-frequency-raytracing-laboratory-propagation-studies>), I simulate the pre-event ray-path that facilitated signal reception by the riometer. This is a baseline simulation that identifies the relevant ionospheric path prior to any absorption.

Ray tracing simulations identify the pathways by which a terrestrial transmission (characterized by an initial location, frequency, and azimuth) reaches the HSR. I note that this simulation, since it utilizes IRI (which simulates a quiet ionosphere), is done at a time prior to the onset of any absorption during an event. Our methodology makes the simple assumption that there are two states to the signal propagation, one (modeled) in which the signal can reach the riometer, and one in which the signal cannot reach the riometer. I assume that the only difference between these two states is the absorbing layer. While the evolution of the ionospheric electron density can modify the signal path, for simplicity we assume here that the path is unchanged. I use the pre-absorption ray tracing simulation to identify the intersection (pierce points) of the ray path with the assumed altitude of the absorbing layer, situated at 85 km. This method informs us how far from the riometer the absorbing layer would need to be to impact the ray path.

Different altitudes and their respective absorption distances are shown in **Figure 4.6**. For this HF link, the average difference in absorption distances between 55, 65, 75, 85 and 95 km altitudes for the assumed layer is about 38 km across the sky per 10 km difference in altitude. Shown in Table 4.2 are absorption distance at a given altitude, average difference between absorption distances and range of absorption distances for all HF links used in this study. The choice of 85 km altitude is due to the nature of the event and is discussed in Section 4.6.

This simple method establishes the minimum size of the absorbing region– defined as the extension of the

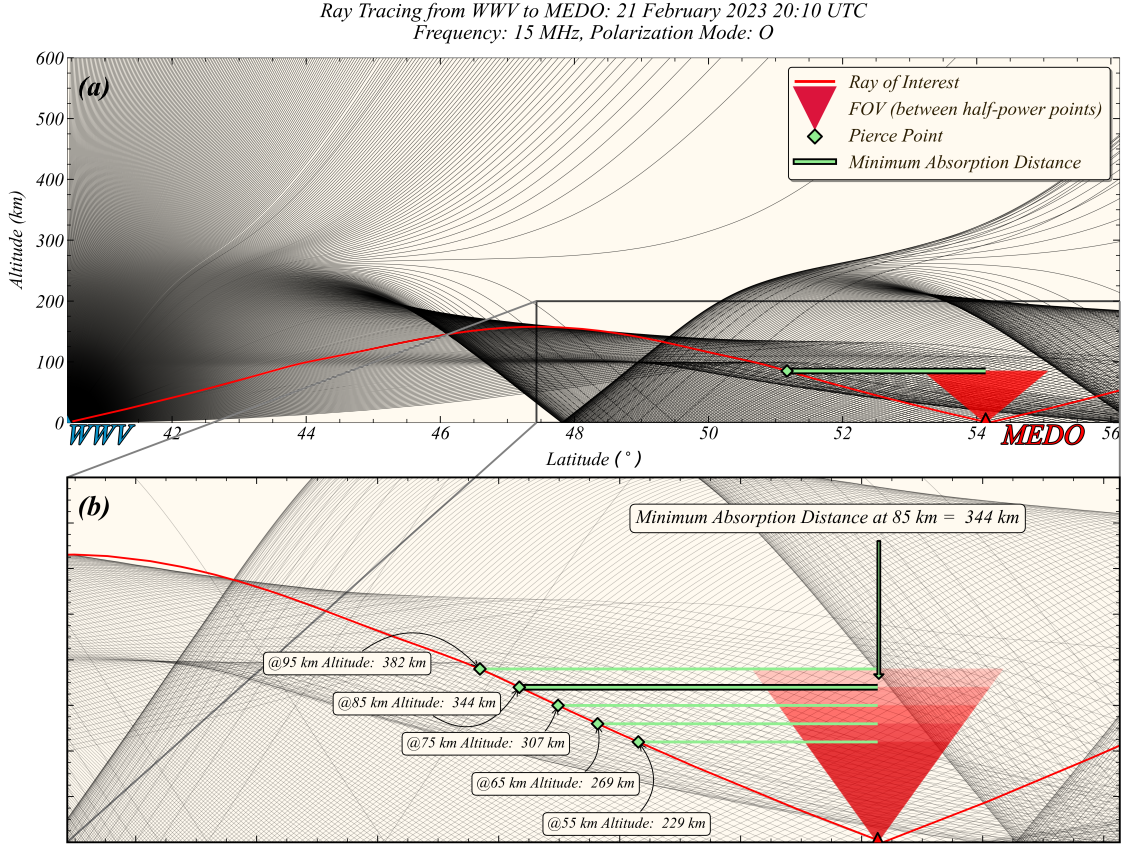


Figure 4.6: (a) Simulation of ray paths for a signal at 15.00 MHz transmitted from WWV at a range of elevation angles along an azimuth towards Meadow Lake (MEDO). The ray-path that reaches MEDO is plotted in red. The FOV, a cone enclosing the half-power points of the antenna's radiation pattern, of the MEDO HSR is shown in red at the HSR site, terminating at the assumed absorbing altitude of 85 km. The minimum size of the absorbing region (shown as a green extension from the center of the cone) is assumed to be the distance from the center of the HSR's FOV to the pierce point of the red ray at 85 km altitude. For comparison, the subfigure (b), a zoomed-in version of (a), shows absorption distances and FOV projections at 55, 65, 75, 85, and 95 km altitudes.

HSR FOV projected to 85 km altitude to the pierce point of the ray and is valid for the direction between the riometer and the transmitter. With multiple riometers and multiple transmitters, there is potential for this method to inform and constrain the size of D-region enhancements. In the following section I detail this methodology for our example event on 21 February 2023, for which two HSRs (MEAN and MEDO) both observed CNA coincident with terrestrial signal loss.

## 4.5 Event Study

Figure 4.7 shows a single day of data from the prototype HSR at MEDO at the 30 MHz single channel, derived from the multispectral data shown in Figure 4.2 (rightmost plot). This day contained multiple absorption

Transmitter	Frequency (MHz)	55 (km)	65 (km)	75 (km)	85 (km)	95 (km)	Average Difference (km)	Range of Distances (km)
<b>HSR at MEAN</b>								
<i>OTTW</i>	11.107	149	174	199	223	248	25	99
<i>WWV</i>	10.000	119	141	163	184	206	22	87
<i>WWV</i>	15.000	96	113	130	148	165	17	69
<i>WWVH</i>	15.000	223	255	286	317	349	31	125
<i>CHU</i>	14.670	215	251	287	322	357	36	143
<b>HSR at MEDO</b>								
<i>OTTW</i>	11.107	94	110	126	142	158	16	64
<i>WWV</i>	10.000	115	135	155	175	195	20	79
<i>WWV</i>	15.000	229	269	307	344	382	38	153
<i>WWVH</i>	15.000	269	314	358	400	443	44	174
<i>CHU</i>	14.670	99	115	131	147	163	16	64

Table 4.2: Absorption distances at 55-, 65-, 75-, 85-, and 95-km altitudes for every Transmitter-HSR link investigated for this event. The average difference is the mean of the differences between absorption distances at the chosen altitudes (e.g., the mean of 40, 38, 37 and 38 km for the WWV-MEDO link at 15 MHz). The range is the maximum minus the minimum of those distances.

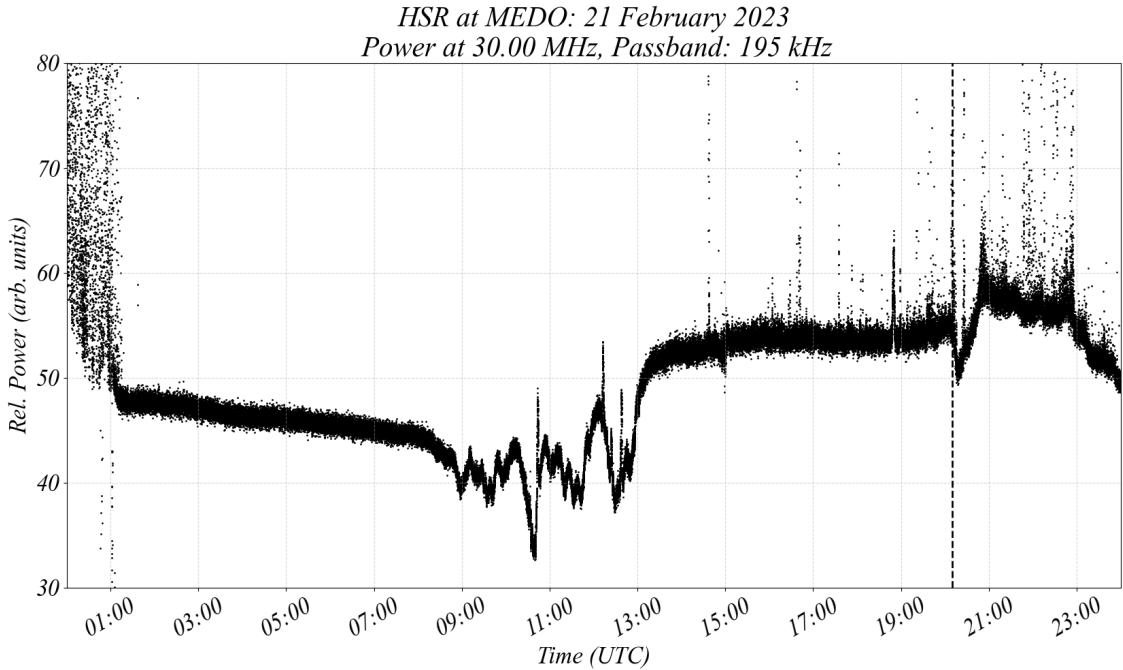


Figure 4.7: An absorption event on 21 February 2023. HSR measurements taken from Meadow Lake (MEDO). Shown is the observed power at 30 MHz, with a passband of 195 kHz. The dashed line indicates the onset used in mapping the absorption region.

events, with associated changes to the terrestrial HF signals acquired by the riometer. While we note the large, dynamic changes occurring in the morning sector, here we choose to focus on the isolated absorption event in the post-noon sector ( $\sim 20$  UTC) due to the simplicity of the absorption signature. The earlier riometer signatures between 8 and 13 UTC are that of AA, marked by their temporal irregularities and may be observed in optical data (not shown here). The latter is a shortwave fadeout event associated with a class-M5 solar flare. The remaining analysis in this section will focus on the shortwave fadeout event, the

onset of which is marked with a dashed line in Figure 4.7.

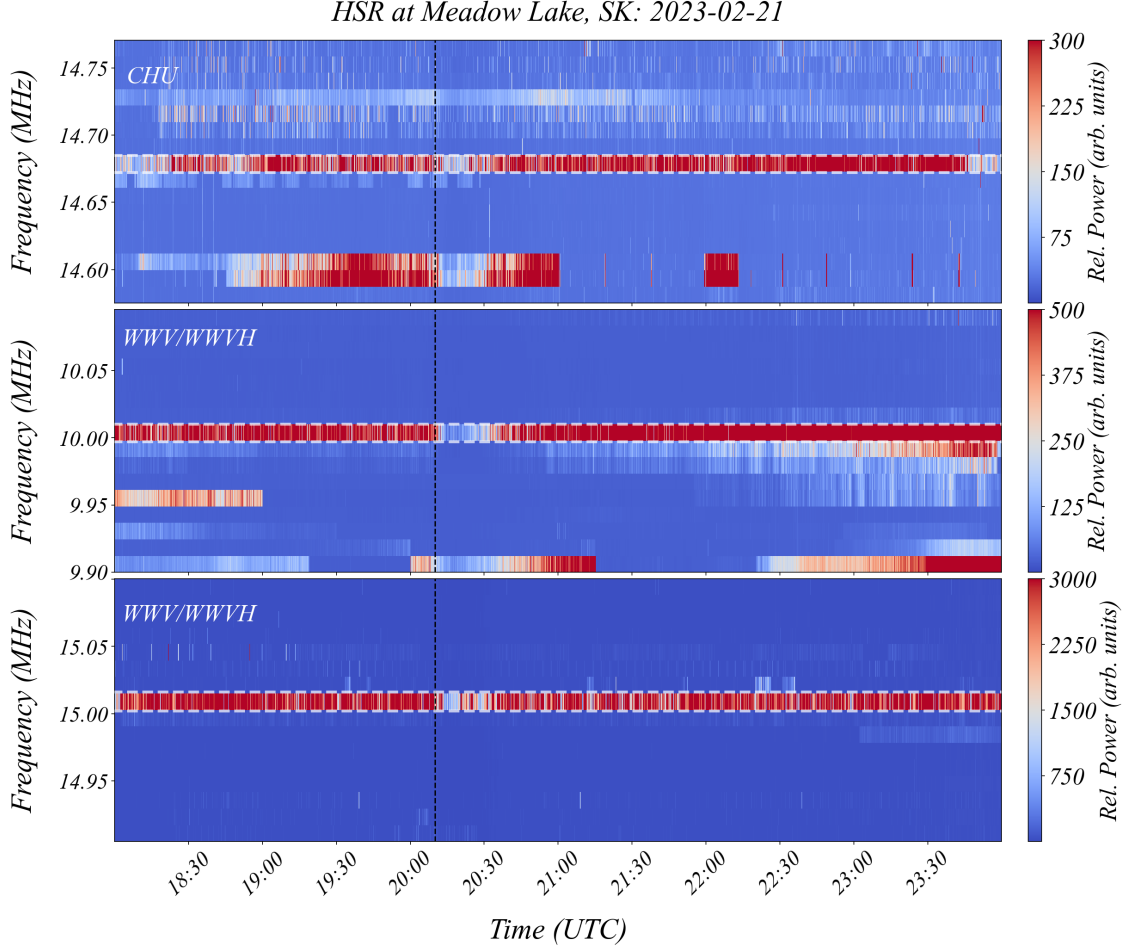


Figure 4.8: Spectra showing terrestrial transmissions for the 21 February 2023 event as observed by the Meadow Lake (MEDO) HSR. In order from top to bottom are plots showing the 14.67 MHz transmission by CHU, followed by 10 and then the 15 MHz transmissions by WWV/WWVH. The appropriate frequency bin is bordered by white dashed lines. Observed is simultaneous reduction of power for these terrestrial transmissions at the onset of absorption marked by the black dashed line.

Coincident with the reduction in cosmic power, is a reduction in terrestrial signals in the lower ( $< 25$  MHz) bands. Figure 4.8 shows the CHU signal from an Ottawa transmitter at 14.67 MHz and the 10 and 15 MHz transmissions from WWV/WWVH. The reduction in observed power from the CHU and WWV/WWVH transmitters is consistent with the onset of the absorption at 30 MHz (dashed vertical line). For our methodology presented here, we are not considering the few minutes around the onset of signal loss and are assuming a binary state of the D-region, quiet (pre-absorption) and enhanced (associated with cosmic absorption). In future work, event-based modeling could utilize finer timing of various HF signal losses to explore ionospheric electron density changes during dynamic events. However, for demonstration of our methodology we here use a binary state, where the two states are a) quiet or b) enhancing or absorbing.

Figure 4.9 shows the coincident loss of the NRCAn signal from OTTW at the 11.1070 MHz band as observed in the 11.1084 MHz bin of the MEDO HSR. For this frequency band, I could not confirm the reception of transmissions from either YKNF or FCHU before the absorption onset – which was also the case for the other NRCAn transmission frequencies.

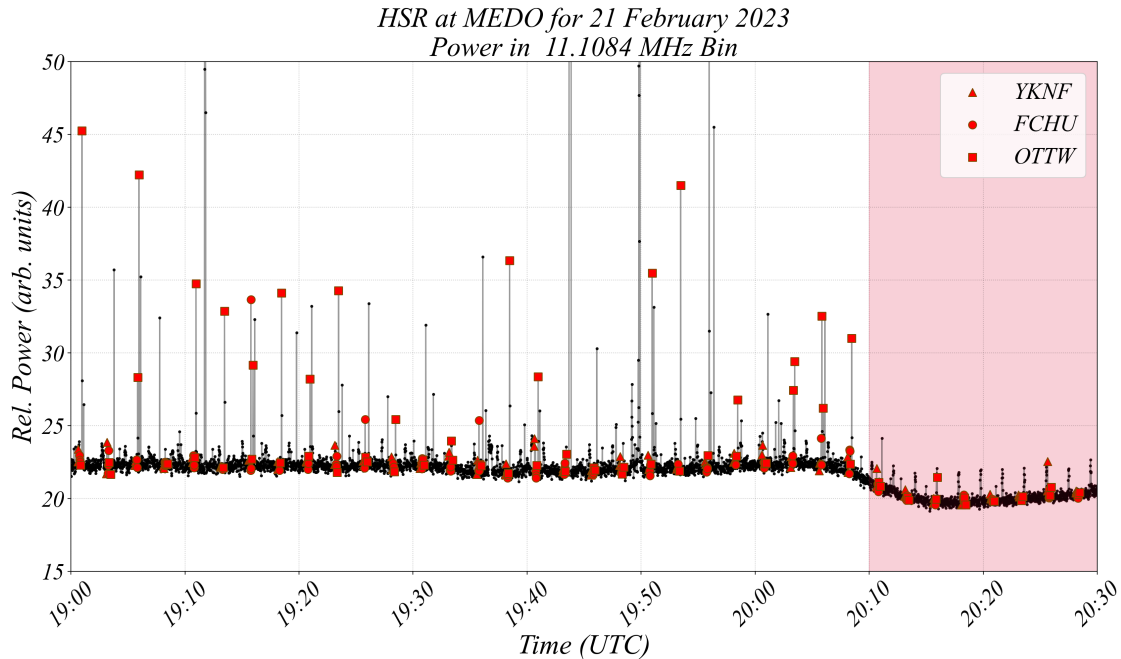


Figure 4.9: The observed power in the 11.1084 MHz bin corresponding to the 11.107 MHz band in which NRCAn transmits. Known transmission times for YKNF, FCHU and OTTW are marked by red triangles, circles, and rectangles, respectively. Observed is an instantaneous loss of the OTTW transmissions at the time of the event, highlighted in red.

Figure 4.10 shows the output of the pierce point analysis for the combined CNA and terrestrial signal loss of the 4 transmitters analyzed in the MEDO data for this event. These are the points where rays from each transmitter intersect the D-region slab at 85 km altitude, on their way down to the riometer, when the ionosphere is modeled to be undisturbed (using the IRI). At the time of the event (20:10 UTC), the HF-link is broken and the pierce point provides an estimate as to where the signal was lost.

Besides the HSRs, I utilized the GO-Canada network of riometers available to us during this event. A baseline was estimated for that day and Figure 4.11 shows absorption measurements from GO-Canada riometers for the day of the event. The GO-Canada riometer at RABB, having the lowest solar zenith angle at the time of the event, shows the highest peak absorption (0.67 dB), while both DAWS and RANK, being

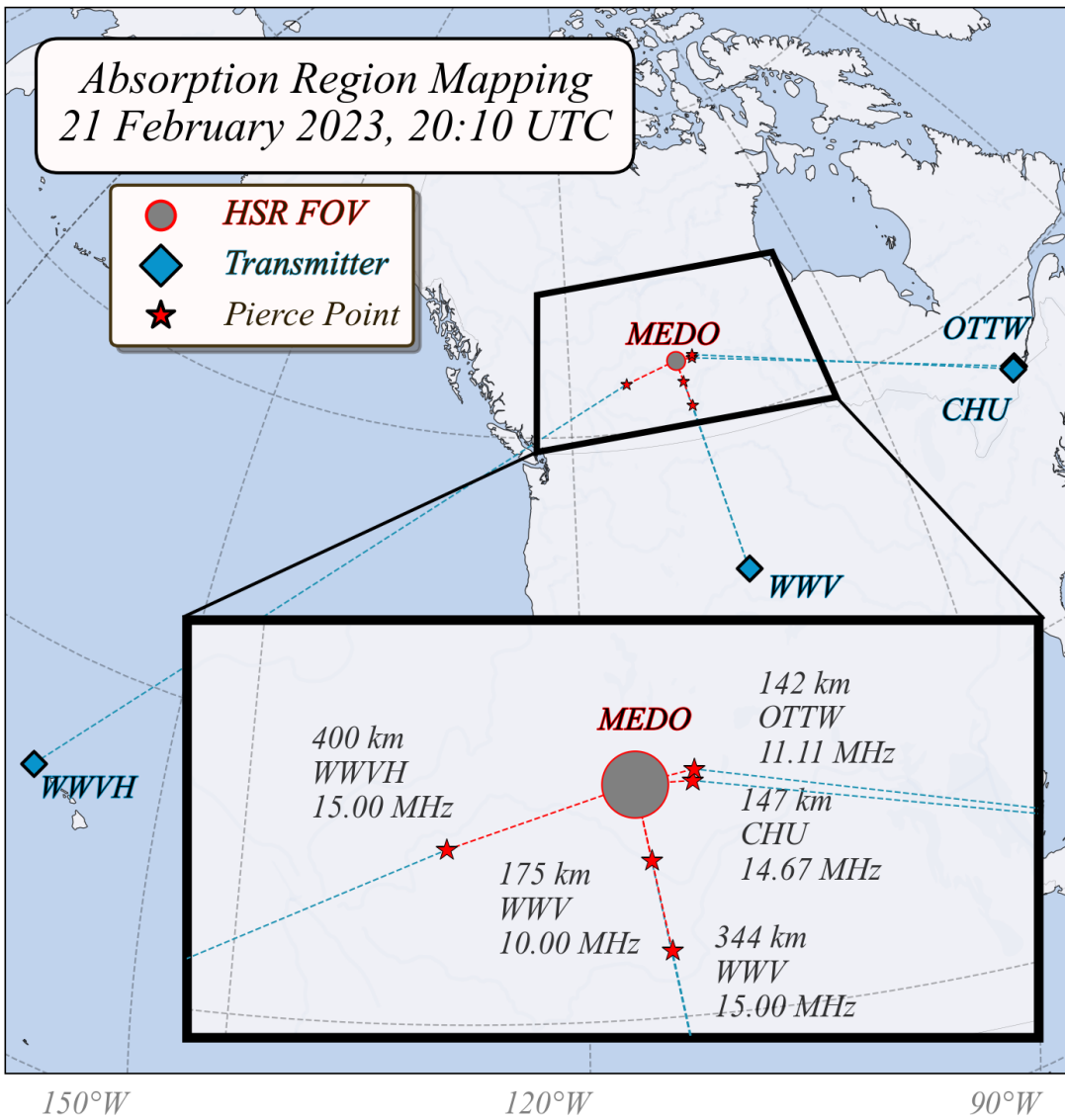


Figure 4.10: Map showing the pierce-point of the rays that reach the riometer prior to absorption onset for the event on 21 February 2023. Ray traces were performed at 20:10 UT and 7.85 MHz for CHU, 10 and 15 MHz for WWV/WWVH, and 11.107 MHz for NRCan's Ottawa (OTTW) and transmitter. The HSR's FOV is projected to 85 km altitude.

the farthest away from the subsolar point, have the lowest peak absorption. GO-Canada riometers with peak absorption higher than or about 0.5 dB have been utilized in the mapping in Figure 14. Figure 14 is the combined MEAN and MEDO pierce point analysis for the available terrestrial links in each of their data. I note the clustering of the pierce points provides confidence as to the boundary of the absorbing layer. More pierce points in close proximity indicate a higher likelihood that the same absorbing region was responsible for the loss of the rays associated with those pierce points.

*Absorption from GO-Canada Riometers*  
21 February 2023

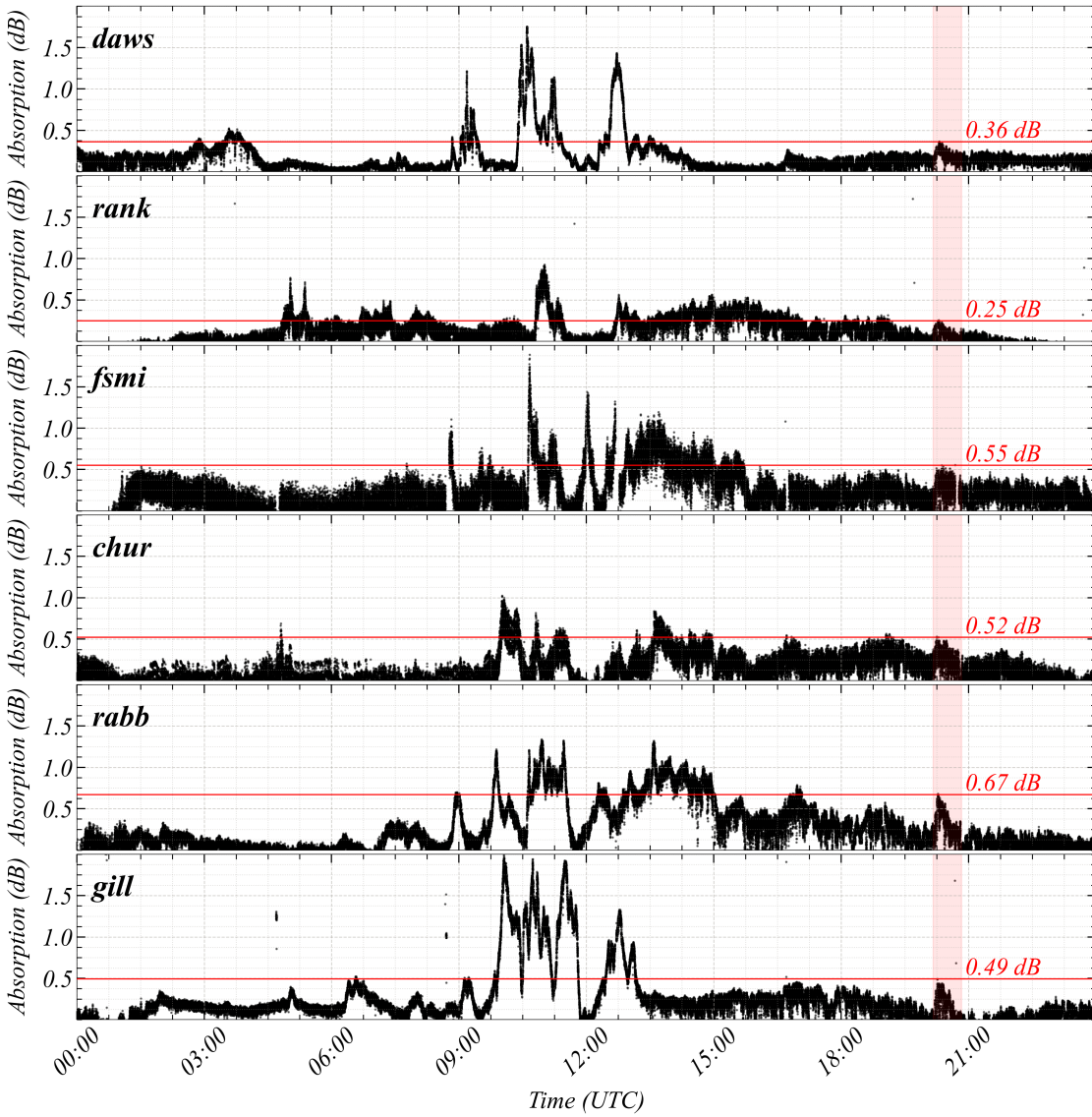


Figure 4.11: Absorption measurements from the GO-Canada riometers for the day of the 21 February 2023. Peak absorption during the time of the event (highlighted in red), is shown by a horizontal red line along with the measurement of peak absorption above it (written in red). The site code is displayed on the top left corner of each plot.

## 4.6 Discussion

I have presented a methodology to leverage terrestrial HF information contained in new Hyper-Spectral Riometers (slated to replace existing GO-Canada single frequency systems in the 2024-2025 timeframe) and provide information about spatial extent of electron density enhancements. Our methodology allows for estimation of the geographic extent of D-region enhancements under certain conditions. I note that,

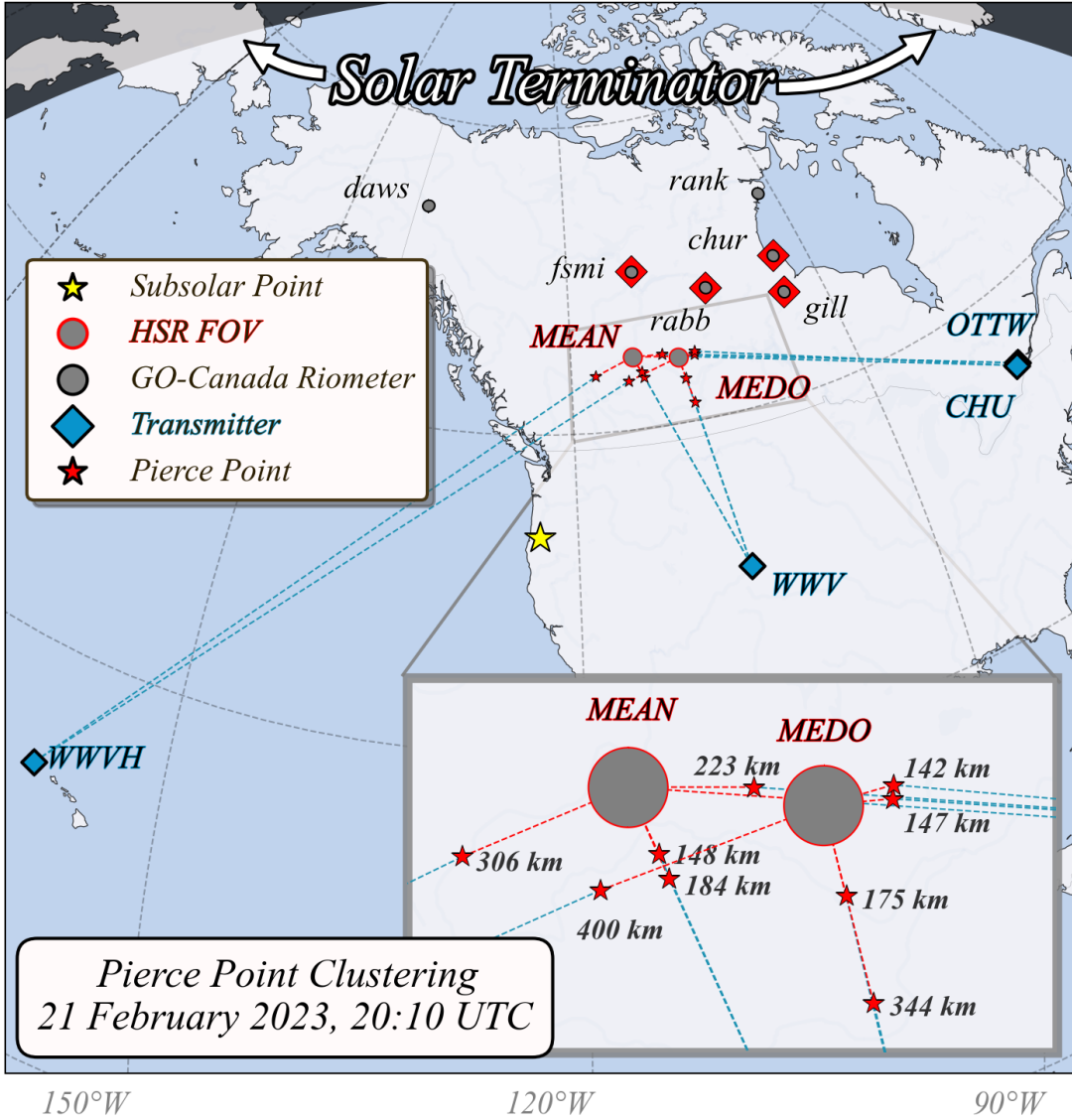


Figure 4.12: Map showing the pierce points extracted via applying our methodology to both the Meanook (MEAN) and Meadow (MEDO) HSRs. The clustering of pierce points defines the boundary of the absorbing region. GO-Canada riometers, shown as gray circles with black boundaries, have been added to the map. Additionally, GO-Canada riometers with peak absorption of 0.5 dB or higher are marked with a red diamond behind the gray circle. The subsolar point is shown as a yellow star and the boundary of the solar terminator is marked by the shaded region. The distance from each riometer to different pierce points (red dashed lines) is indicated next to each pierce point. One pierce point connecting CHU to MEAN is located within MEDO's FoV.

when utilizing the low-power NRCan signals, this methodology does not allow for exploration of the dynamics within the absorbing region, since once the terrestrial signal is lost there is no further information. Therefore, the structuring within the absorbing region, or information about its temporal dynamics are not available. We do however note that information from the initial loss of terrestrial HF signals from within

the riometer data can provide valuable information about instantaneous sizes along multiple axes (e.g., AA precipitation region, boundary of the polar cap). Here we have shown one such example, from the prototype SWAN HSR data, where I utilized information about 4 known HF transmitters to infer the size of an assumed absorbing layer associated with a region of enhanced D-region electron density. I have found that the methodology provided a consistent picture of the extent of D-region electron density enhancements when compared amongst 2 different HSRs. The spatial extent derived is also consistent with expected behavior of riometer spatial scales and impact region for HF dropout due to the solar flare event (Frissell et al., 2014).

For the high-power timing signals, the signal power is significantly diminished, but the signal is not completely lost. Quantifying the signal loss can allow for modeling the D-layer responsible for incurring such loss since the ray tracing toolkit calculates the total absorption as a function of the ray path. For example, the width and depth of the absorbing layer could be simulated to yield absorption levels that match those observed in the data.

An absorbing layer height of 85 km was assumed in the generation of the pierce point map shown in Figure 14. The actual height of peak absorption can vary depending on the absorption mechanism. Studies using radars in conjunction with riometers indicate that the height of peak absorption (AA) typically falls within the 85 to 95 km altitude range, with 50% levels relative to the maximum falling between about 5 and 20 km (Burns et al., 1990; Devlin et al., 1986; J. K. Hargreaves, 1980; J. K. Hargreaves et al., 2007; J. Hargreaves & Devlin, 1990). There are some extreme cases where AA can penetrate much deeper (Collis et al., 1996). For AA, assuming 85 km would be most suitable as it is the minimum of the aforementioned range. However, the assumption for the slab's altitude may differ for different events, for example being lower, between 45 and 65 km, for daytime PCA events (e.g., (J. K. Hargreaves, 2005; Kavanagh et al., 2004)) as compared to AA (Rees, 1963, 1964). For flares, the base of the enhanced D-region is generally below 70 km, decreasing with increasing flare intensity (McRae & Thomson, 2004; Mitra, 1974)

The choice of slab height is critical to the methodology presented here. In general, that decision will be informed by the type of event (as discussed above). For certain events (e.g. nightside auroral absorption or flares), multiple riometers can be employed to elucidate the temporal and spatial nature of the riometer signatures (e.g., (R. a. D. Fiori et al., 2018; Spanswick et al., 2007)), and inform the choice of slab height based on an assumed source of D-region enhancement. In addition, data from other sources can be used to inform the methodology where appropriate. For example, for the event presented here, we confirmed the presence of a flare utilizing the GOES X-ray flux.

The slab height and ionospheric model are the two largest sources of error within this technique. Table 4.2 can be used to estimate the error due to slab height, with an approximate 27 km difference in range determination for every 10 km of altitude difference in the slab height. Some of this can be mitigated by utilizing more than one frequency from a given transmitter. Rays with higher angle-of-arrival generally require more hops and pierce the D-region closer to the riometer. Therefore, the low-angle rays provide the upper limit on the absorption distance. Often, both a range of high-angle and low-angle rays can provide viable links. The clustering of pierce points across frequency can therefore provide confidence for the spatial structure of the absorbing region. Other errors will occur via the modeling of the ray reflection height, which is a function of the modelled ionospheric electron density. I assert it is minimized here since the model is utilized to determine signal reception prior to the disturbance. Other models, such as tomographic data assimilative models, will be utilized in future work. Other mitigation of error will occur as more HSRs and transmitters are added to the network, providing estimates from multiple locations and directions.

Our methodology provides pierce point locations beyond the FOV which could be beneficial for over-the-horizon radars and directional HF systems, particularly because wide-beam riometers would miss absorption patches that have crossed the nominal FOV (Birch et al., 2013). Highly localized enhancements, such as the spike event as observed by riometers ((J. Hargreaves et al., 1979; Spanswick et al., 2005)), can be mitigated via channel change. Although, if the HF circuit passes through the spike region, the absorption can be abnormally high, which is often underestimated by wide-beam riometers (Burns et al., 1990; J. K. Hargreaves, 1980; J. K. Hargreaves et al., 1991, 1997) and there is even evidence that the spatial scales of such structures can be less than that of imaging systems' beam-width over small time-scales (J. K. Hargreaves et al., 2007). While localized absorption can be more-easily mitigated, wide-spread absorption that targets multiple areas simultaneously such as the SWF event discussed in this study, or PCA events, may be harder to mitigate (Frissell et al., 2014; Hunsucker & Hargreaves, 2003). A shift to higher frequencies is advised, since the absorption gradually shifts to enhancement as the operating frequency shifts towards the Very High Frequency range (Mitra, 1974).

# Chapter 5

## Riometer Absorption Thresholds

HF radio wave propagation is highly sensitive to changes in ionospheric conditions. As discussed in the introductory material, this study examines the utility of riometers in developing more accurate nowcasts of radio signal fadeout during space weather events. This chapter presents a collaboration project with Natural Resources Canada on using GO-Canada riometer absorption as proxy for HF terrestrial-link signal loss during AA events. Using 28 AA events, I derive thresholds for riometer absorption at different fadeout levels and discuss the implications of riometer positioning in relation to the HF radio path.

### 5.1 Motivation and Goal

Space weather events such as sudden bursts of radiation called solar flares, or the precipitation of geomagnetically trapped, high-energy particles into the atmosphere act to reconfigure the electron density in the ionosphere (Hunsucker & Hargreaves, 2003; Mitra, 1974). This reconfiguration alters the propagation conditions for HF radiowaves, which might break an HF circuit depending on the locations of the transmitter and the receiver and the time. During times of AA, the enhanced ionization can incur loss of signal by multiple mechanisms. One mechanism, which riometers can remote sense, is D-region absorption, which occurs at 70–90 km altitude, where the electrons collide with the neutral particles.

NRCan actively reports times of disturbance (using data from GOES, OMNI, etc.) as part of their daily protocol, to inform various industries when a geomagnetic or solar event is posing hazards to navigation and communication to name a few (Blagoveshchensky et al., 2006; Cannon, 2009; Ritchie & Honary, 2009; Ruck & Themens, 2021). This study investigates how widebeam riometers can be used as proxies for signal fadeout during AA events, to incorporate them in future alarming systems. Since AA events are sporadic,

both spatially and temporally, and highly variable in terms of their signature in riometer data (see Section 3.2.4 and references therein), the statistical methods I employ divide signal loss into ordinal categories, to elucidate the severity of the event (in terms of signal loss) in connection to the measured riometer absorption.

## 5.2 Project Outline

The main objective of this study is to determine the riometer absorption levels for which significant amounts of HF signals dropout for the OTTW to ALRT link. A clear definition of signal dropout is given in the following and relies on the quiet-time, expected level of signal reception, which I refer to as the \*\*Baseline Occurrences\*\*, where \*\*Occurrences\*\* refers to the number of signals received in an hour at ALRT. Deviations from the baseline quantify dropout (similar to riometer baselining). Once dropouts are defined, I conduct an ordinal analysis using a total of 28 AA events to find the distribution of dropouts as a function of riometer absorption level for 5 riometer sites: *talo*, *rank*, *chur*, *gill*, and *isll*.

My outline is as follows. I start by introducing the data and instrumentation used, how to properly interpret signal reception, and quantify signal loss in Section 5.3, then I perform an ordinal statistical analysis of 28 AA events to show how absorption correlates with loss of signal in Section 5.4, and finally discuss the implications of these results on riometer position and the frequency of the HF link used in Section 5.5.

I must note that the results presented in the following are preliminary as the project timeline was limited. To preserve project continuity, my goal in writing this thesis (for this project) was to document all the necessary information needed to carry on, including technical details, however, at the cost of simplicity of the text. This is done intentionally to help the next individual or team carry on with this work with as smooth a transition as possible.

## 5.3 Data Preparation

This study used data from 5 GO riometer stations combined with HF-link data from NRCan's receiver at Alert (ALRT). The riometers are roughly situated on the great-circle-path connecting NRCan's Ottawa transmitter (OTTW) to their receiver at Alert. A map of the analog GO riometers and details of their locations are provided in Figure 3.2.3 and Table 3.2, respectively. For a map showing both OTTW and ALRT as well as details of their locations, please refer to Figure 3.10 and Table 3.3, respectively.

The combined riometer and HF-link datasets span December 2013 to October 2019. Riometer data has been introduced in Section 3.2.3 and the ALRT dataset has been discussed in Section 3.3.1. I start by discussing riometer data, and how it was downsampled to a cadence suitable for analysis. Then I discuss the HF dataset.

### 5.3.1 Riometer Data

GO riometer absorption data from *talo*, *rank*, *chur*, *gill*, and *isll* was used in this analysis. Absorption measurements are publicly available at [https://data.phys.ucalgary.ca/sort\\_by\\_project/GO-Canada/GO-Rio](https://data.phys.ucalgary.ca/sort_by_project/GO-Canada/GO-Rio). To perform a statistical analysis, the cadence of the two datasets was matched to 1-hr intervals since that choice smoothes out any temporal variability on smaller scales, characteristic of some AA events. To obtain a quantitative measurement for the hour, the peak absorption level must be utilized. Before binning the data to an hourly cadence and using the 99<sup>th</sup> percentile of the distribution of measurements for each hour, the data is convolved with a Kaiser window to eliminate calibration spikes and low-frequency noise. An example of this filtering process is shown in Figure 5.1.

### 5.3.2 HF Link Data

In Section 3.3.1, I have discussed HF receptions at various frequencies, namely 5.382, 6.9285, 8.0995, 10.422, 11.107, and 14.3644 MHz (see Figure 3.12). These transmissions are staggered in time for discernability. Any time a signal is received at ALRT from the OTTW trasnmister, depending on the SNR and other parameters, the the modulation of the signal can be decoded, which implies the signal was successfully received. Otherwise, if the receiver fails to demodulate the signal, then it is lost. This signal loss is what I aim to quantify, and the next few sections discuss the methodology behind that.

To study signal fadeout, I rely on reception ***Occurrences***, or the number of signal receptions within an hour, since a reception implies a transmission's Binary Phase-shift Keying modulation was successfully

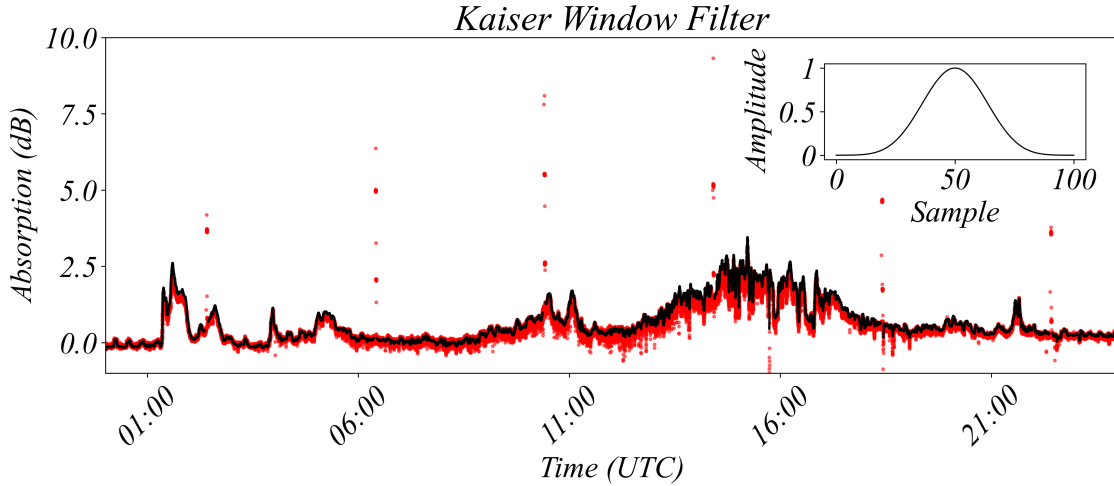


Figure 5.1: Riometer absorption, shown in red, is filtered via the Kaiser window shown in the inset axis, and the filtered absorption is shown in black.

demodulated. Demodulation in this context means detecting the phase changes in the received signal and converting them back to zeros and ones. Demodulation occurs when the received sequence of 0s and 1s matches the originally transmitted sequence (i.e. there are minimal errors introduced as the wave travels from the transmitter to the receiver) (Malik et al., 2014). Such demodulated signal is herein referred to as a reception or an occurrence.

Other parameters pose difficulty for data analysis. For example, using SNR requires establishing an approximation of the receiver’s noise floor, which is impossible to do without (and difficult to do with) calibration data— not available to me. Using the time difference between consecutive receptions, I found the maximum number of transmissions for a given hour. Shown in Table 5.1 is how the maximum varies by frequency and year. The variation by year is due to changes in operational mode. Due to the variability, I restrict myself to data from 2016 and beyond, since that variation can affect any statistical analysis performed on the data, as I shall demonstrate in the following. The distribution of occurrences for 5.382 MHz for the whole dataset is compared with that of data from after 2016 in Figure 5.2 for demonstration. The distribution for the whole dataset has a distinct peak at 4 occurrences, since that is the maximum number of transmissions for data from before 2016, and another peak at 8 occurrences since that is the maximum for data beyond 2016. The trimodal nature of the distribution for the whole dataset could lead one to the misinterpretation that there are two and only two distinct processes by which occurrences (receptions) take place. However, knowing that the maximum number of transmissions changed in 2016 for both 5.382 and 10.422 MHz is evidence to the contrary. Therefore, I shall proceed with data from after 2016 only; later on,

when discussing Figure 5.6, the impact of this shift in maximum occurrences shall become more clear.

	5.3820 MHz	6.9285 MHz	8.0995 MHz	10.4220 MHz	11.1070 MHz	14.3644 MHz
<b>2013</b>	<b>4</b>	8	24	<b>4</b>	24	24
<b>2014</b>	<b>4</b>	8	24	<b>4</b>	24	24
<b>2016</b>	8	8	24	8	24	24
<b>2017</b>	8	8	24	8	24	24
<b>2019</b>	8	8	24	8	24	24

Table 5.1: Maximum Occurrence Look-up Table. The number of maximum transmissions at a given frequency is displayed for each year. Years missing imply no data. Only 5.382 and 10.4220 MHz transmissions are affected by some operational change sometime after 2014, going from 4 to 8 maximum transmissions.

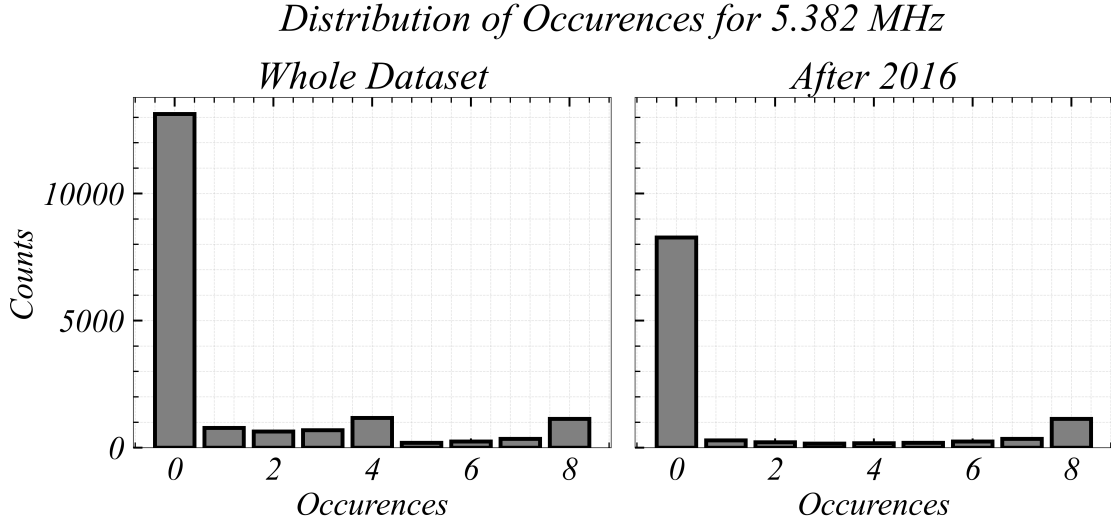


Figure 5.2: The distribution of occurrences for the 5.382 MHz transmissions for the whole dataset (left) and only a subset that included data from after 2016 (right). The peak at 4 occurrences for the distribution on the left is due to the maximum transmissions capped at 4 for data before 2016.

### Time Dependence of Occurrences

To quantify signal loss, one needs a measure of *Dropouts*—the loss of an HF-link. The distribution for occurrences (how many signals were demodulated in a given hour) for data beyond 2016 shown in Figure 5.2 is evidence that one cannot use occurrences to establish such measure for a few reasons. First, the bimodality of the distribution implies two distinct physical processes, one responsible for 0 occurrences and the other for the maximum, 8 occurrences. However, these processes cannot be modelled as Binomial or Poisson, as they are not independent of each other. My attempts at such models failed, even when using a zero-inflated model (e.g., zero-inflated poisson or zero-inflated negative binomial). Losing signal does not occur without some process, which most likely spans more than one hour. For example, many signals are lost during an AA event; these dropouts occur together. Thus, a dropout at a given point in time can be used as a predictor

for a dropout, say, 7.5 minutes later. Furthermore, 0 occurrences in a given hour does not necessarily imply signal dropout. For example, during the day, 5.382 MHz signals cease to propagate mainly due to D-region absorption. We therefore do not expect 5.382 MHz occurrences during the day. There are no dropouts in this case. Instead, we expect these transmissions to arrive mostly when the HF-path is not illuminated by the Sun. As the Sun sets away from the HF path, more signals start to arrive. Thus, having high occurrences is also a process which cannot be modeled without considering time as a conflating variable. Both time of day (i.e., daytime vs. nighttime) and whether an event is taking place (during a given hour) should be considered. To show this time dependency, I calculate the mutual information between the hour of day and the number of occurrences in that hour. Mutual information between two discrete data sets,  $X$  and  $Y$  can provide a measure of the information content one adds to variable  $X$  by introducing another variable  $Y$ . If, for example, there is a higher probability for 0 occurrences at  $h = 16$  UTC than at  $h = 4$  UTC, then one might expect a correlation between the hour of the day and the number of occurrences. I shall examine this correlation here.

If two variables are independent, then it is said that they share no mutual information between them; that is, the information content of both variables,  $S(X, Y)$ , is simply the sum of the information content of the independent variables:

$$S(X, Y) = S(X) + S(Y)$$

where

$$S(X) = - \sum_i p(x_i) \log_2 (p(x_i)), \quad (5.1)$$

in bits, since  $\log_2$  is used, and  $p(x_i)$  is the probability for the  $i^{th}$  observation to occur in the  $X$  dataset. The joint probability is given by

$$S(X, Y) = - \sum_i \sum_j p(x_i, y_j) \log_2 (p(x_i, y_j)) \quad (5.2)$$

and  $p(x_i, y_j)$  is the joint probability, or the probability for both  $x_i$  and  $y_j$  to occur simultaneously. If two variables are related, there is a surpass of information “embedded” or shared between the two datasets, and their joint entropy becomes

$$S(X, Y) = S(X) + S(Y) - I(X, Y), \quad (5.3)$$

where  $I(X, Y)$  is the mutual information shared between  $X$  and  $Y$ . In our case, the sum of the entropies of the hours,  $S(H) = 2.63$  bits, and the occurrences,  $S(O) = 1.85$ , is 4.48 bits, which is 0.12 bits larger than the joint entropy,  $S(H, O) = 4.36$ . That surpass constitutes the mutual information. The mutual information

between the hour of the day,  $h \in H = \{0, 1, 2, \dots, 23\}$ , and the number of occurrences in that hour,  $o \in O$ , is given by

$$I(H, O) \equiv \sum_{h \in H} \sum_{o \in O} p(h, o) \log_2 \left( \frac{p(h, o)}{p(h)p(o)} \right) \quad (5.4)$$

and  $O$  is the set of possible number of occurrences for a given transmission frequency in a given hour (e.g.,  $O_{5.382 \text{ MHz}} = \{1, 2, \dots, 8\}$ ),  $p(o)$  is the probability for a given number of occurrences,  $p(h)$  is the probability of a given hour, and  $p(h, o)$  is the joint probability between the two variables. The mutual information evaluates to 0.12 bits, the deficit which is shared between the two variables. Calculations for the entropies and the mutual information are summarized in Table 5.2.

	$S(H)$	$S(O)$	$S(H, O)$	$I(H, O)$
<b>bits</b>	2.63	1.85	4.36	0.12

Table 5.2: Information entropy of the hour of day,  $S(H)$ , occurrences in the hour,  $S(O)$ , as well as their joint entropy,  $S(H, O)$ , and mutual information shared between the two,  $I(H, O)$ .

This result implies that one cannot simply use occurrences without factoring in the time. To account for this, only a subset of 28 AA events, where dropouts are bound to occur, will be used in the final statistical analysis. Additionally, a method for quantifying dropouts, which factors time as a variable, is needed.

## HF Baselines

In order to quantify signal dropout, a method similar to riometer baselining (**Section 3.2.1**) was employed. This methodology was introduced to me by Dr. Taylor Cameron, as it was emplyed in (Cameron et al., 2021). After downsampling the HF dataset to an hourly cadence, a period of 30 days around any day of interest is considered. Hours associated with significant levels of disturbance are eliminated. Using data from GOES, times with XRF above  $5 \times 10^{-5} \text{ W/m}^2$  and those where the flux of  $> 10 \text{ MeV}$  protons exceeded 10 pfu are considered disturbed. For AA, times where the AE index, obtained from the OMNI dataset, exceeded 400 nT were also eliminated when constructing HF baselines. The occurrences,  $O$ , within each UTC hour are then aggregated and divided by the maximum number of occurrences for that given time and frequency to produce **Normalized Occurences**,  $O_N$ . Finally, the baseline,  $B_N$ , is taken to be the 80<sup>th</sup> percentile of the distribution of the normalized occurences within that hour.

Figures 5.3 and 5.4 showcase this baselining procedure for 18 Apr 2014. The top three plots showcase the OMNI AE Index and GOES proton and X-ray flux, in that order. Times, where these indices exceed their respective thresholds (displayed as a red horizontal line), are highlighted in red. A flagging array of 1s and 0s is plotted below the indices. The only modification to the initial methodology described by Dr.

Cameron is my use of a convolutional algorithm (taking the baselining time of the entire dataset from 2013 to 2019 down to 9 s), which counts the number of flags. For instance, there are 8 thresholds exceeded in the first 24 hour window, highlighted in gray. Hence, there are 8 flags, as shown by the convolution plot below the flag plot. When the flag counter is zero is the beginning of a quiet day, highlighted in green in Figure 5.3. The bottom plot shows the normalized occurrences for the 5.382 MHz signal with the quiet-time occurrences, also highlighted in green, accumulated for each hour separately and plotted in Figure 5.4. The 80<sup>th</sup> percentile for each hour forms the baseline for that hour. The 5.382 MHz baseline shows that no signals are expected during the daytime, highlighted in yellow.

This baselining is necessary due to the diurnal variation of LUF and MUF under quiet conditions. For example, a 5.382 MHz signal is not expected to propagate during the day. Therefore, the lack of occurrences during, say, local noon is not representative of dropout but rather represents the normal propagation conditions for such signal in a quiet ionosphere. Different frequencies are affected differently; hence, for each day, a baseline is made for each frequency. These baselines shed light on the inflation of 0 occurrences in the distributions in Figure 5.2 and show the true meaning of 0 occurrences. First, as shown in Figure 5.5 (left), 0 occurrences can happen even when the baseline itself is 0, which explains the inflation of 0 occurrences as due to the diurnal variation captured in the baselines. Only when the baseline is not zero for 0 occurrences can we say a full blackout occurred in that hour. At the maximum, we expect that we get the baseline to be high almost all the time. Anytime the baseline is less than the maximum, an enhancement occurs. For the plot on the left showing the baseline distribution for the maximum occurrences, this happens about 5.5% of the time (there are other times, when the occurrences are not 8). The inset axis aids in showing this minuscule effect, which we refer to as an *Enhancement*. Enhancements are discussed further in Sections 5.5 and **6.2.1**, but are insignificant here such that they can be ignored.

Since times where we expect no signals ( $B = 0$ ), they offer no information about dropouts. Excluding times with  $B_N \leq 0.1$ , Figure 5.2 is reproduced to show the distribution of occurrences for data with  $B_N \geq 0.1$ , as shown in Figure 5.6. It becomes apparent that most of the 0 occurrence data were at times where the baseline was also 0, not relevant when discussing dropouts. This thresholding for the baseline is necessary, to account for the steep rollover in signal reception between night and day. A threshold of  $B_N \geq 0.75$  was optimal for eliminating points at the rollover, as shall be shown in Figure 5.8.

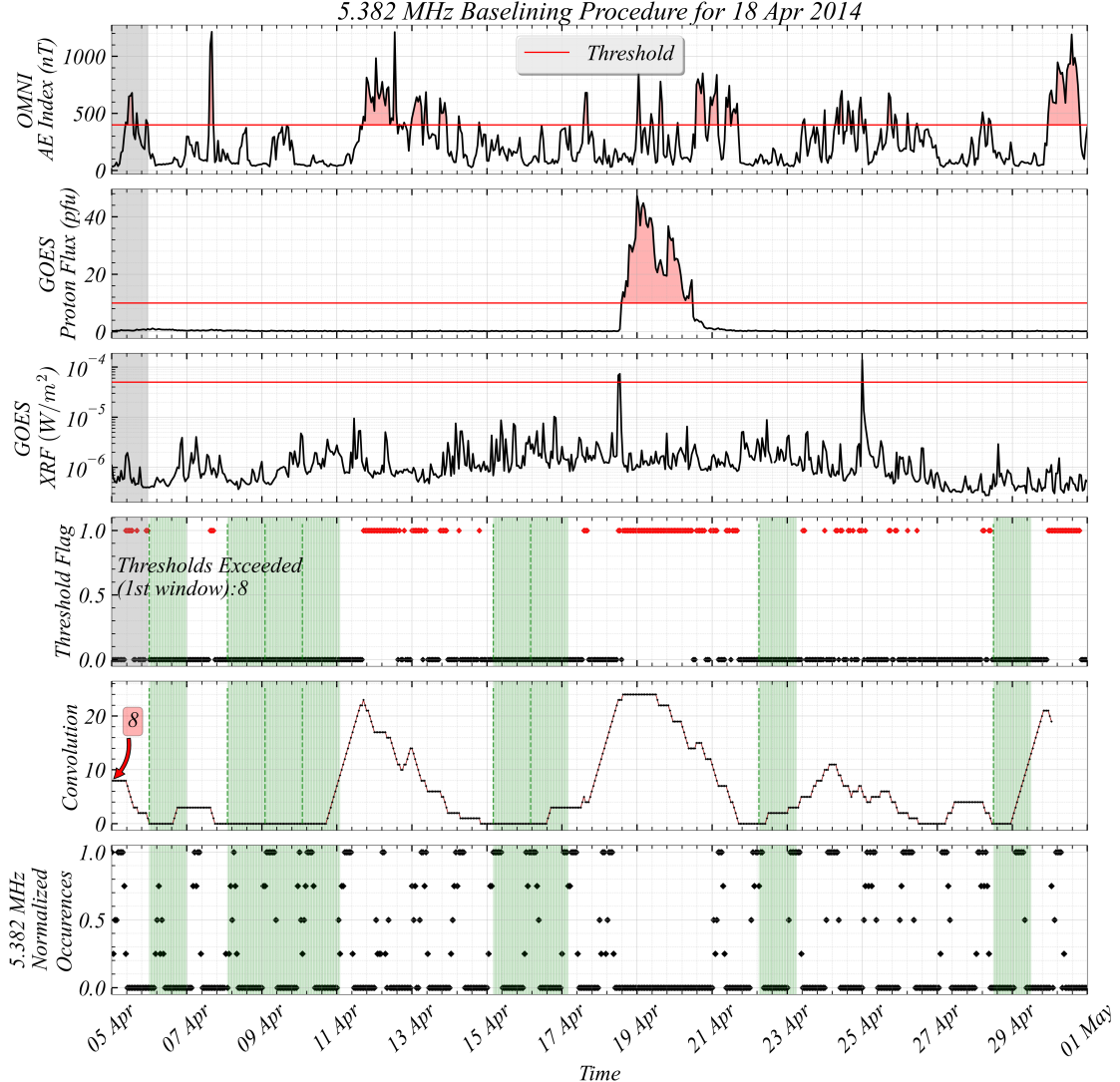


Figure 5.3: Baselineing procedure for April 18, 2014 for the 5.382 MHz transmissions, using OMNI AE Index, GOES proton, and X-ray flux to identify disturbed times. Below these indices, shown in red and marked 1 are these disturbed hours. Below that is a sum, showing the number of disturbed hours in a 24-hour convolutional window. At the bottom are the normalized occurrences within each hour. Highlighted in green are the quiet times used in generating the baseline.

### Quantifying Signal dropout

Finally, to quantify signal dropout,  $D$ , the initial methodology, employed in Cameron et al. (2021), took the difference between the observed number of occurrences,  $O$ , and the baseline,  $B$ , dividing by the normalization factor introduced earlier (i.e., the maximum number of signals in that hour as a function of year,  $y$ , and frequency,  $f$ ,  $O_{max}(f, y)$ , as shown in Table 5.1) to calculate the normalized dropouts,  $D_N$ :

$$D_{N_{w.r.t \text{ Maximum}}} \equiv \frac{B - O}{O_{max}(f, y)}.$$

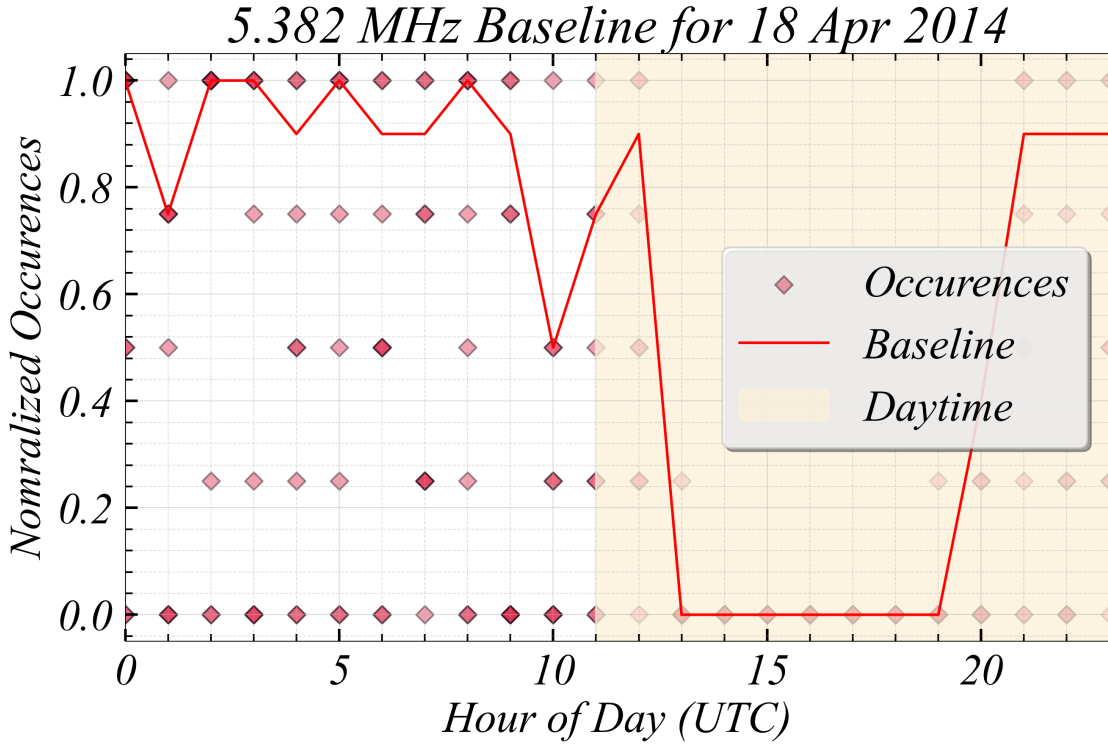


Figure 5.4: Hourly baseline for 5.382 MHz signal derived from quiet-time occurrences via the procedure in Figure 5.3. The daytime, highlighted in yellow, delineates the diurnal variation, as 5.382 MHz signals cannot propagate during the day.

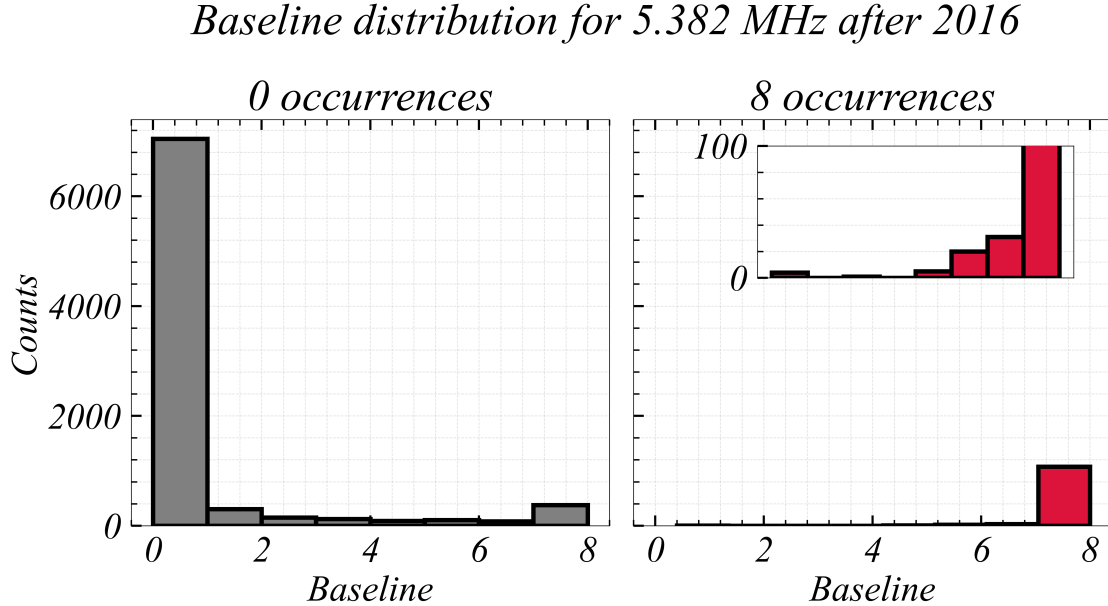


Figure 5.5: The distribution of baseline values for 0 (left) and 8 (right) occurrences (the maximum) for 5.382 MHz. The inset axis shows a few enhancements, indicated by the values of the baseline < 1.

*Distribution of Occurrences for 5.382 MHz*  
*Baseline Threshold:  $B_N \geq 0.1$*

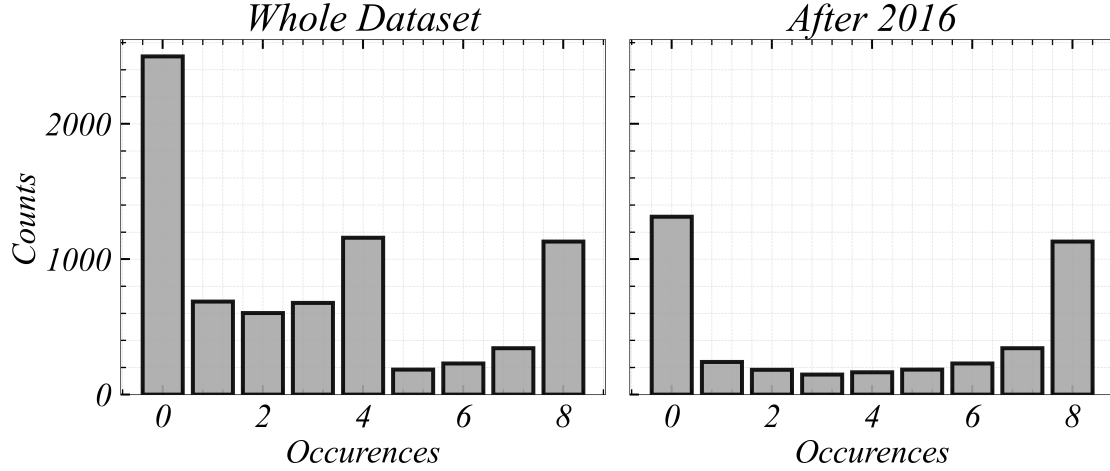


Figure 5.6: Same as Figure 5.2 but after eliminating data with  $B_N \leq 0.1$ .

This definition compares the dropouts to the maximum occurrences to normalize the data, however, at the cost of losing information about the baselines. In order to preserve the information encapsulated within the baselines, I defined a dropout as

$$D_{N_{\text{w.r.t Baseline}}} \equiv \frac{B - O}{B} = \frac{B_N - O_N}{B_N}.$$

To illustrate, if at a given hour, we expect 6 receptions of the 5 MHz signals, but instead the receiver was able to decode (and thus confirm) only 4 signals, then we lost 2 signals in total, or  $\frac{6 - 4}{6} = \frac{1}{3}$ , a third, of the transmissions expected were lost, which is higher than  $\frac{6 - 4}{8} = \frac{1}{4}$  (refer to Table 5.1 for  $O_{max}(y, f)$ , for  $y \geq 2016$ ). Thus, there is an underestimation where

$$D_{N_{\text{w.r.t Maximum}}} < D_{N_{\text{w.r.t Baseline}}}$$

except for when there are enhancements, there are no dropouts (i.e.,  $B = O$ ), or the baseline is equal to the maximum ( $B_N = 1$ ). This underestimation is captured in Figure 5.7. No data point crosses the  $y = x$  line. At  $B_N = 1$ , the data (shown in red) lie on that line. Again, data points with  $B_N \leq 0.1$  have been omitted for clarity of illustration.

To showcase dropouts, an example AA event is shown in Figure 5.8. From dusk till dawn, highlighted in yellow, we expect no receptions at 5.382 MHz, captured in the baselines. This diurnal feature is a byproduct

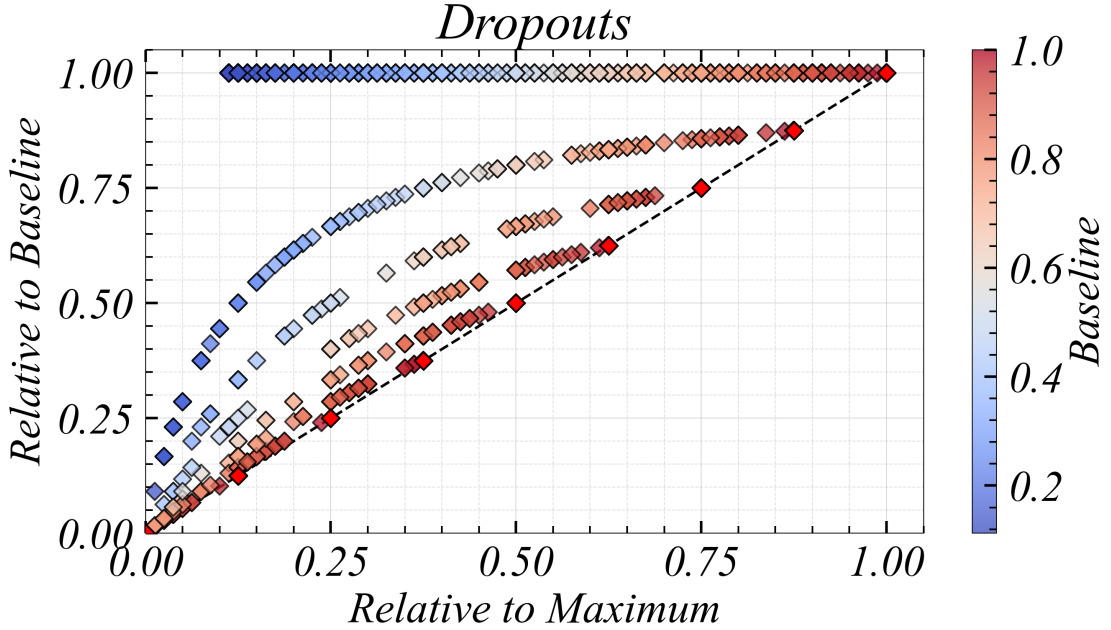


Figure 5.7: The dropouts as measured relative to the maximum (x-axis) versus as measured relative to the baseline (y-axis). The colors as given by the colorbar scale with the baseline value. The dashed black line has a slope of 1.

of the enhanced ionization during the day, causing enhanced absorption for the lower frequencies. The opposite could be said for the higher frequencies, though the signal loss during the night is not in general to absorption. For times when there is activity, we can see that the difference between the baselines and the occurrences (dropouts) are high, almost coincident with absorption though the degree varies between riometer sites. Neither X-ray Flux nor Solar Proton Flux on GOES exceeded their thresholds for this event. Some dropout data points are omitted from the figure. These points constitute times when the baseline was  $B_N \leq 0.75$ . If these points were included, full blackouts would show at times when the absorption is low, simply due to the steep rollover in baseline values between night and day. In the following, I present a statistical analysis for 28 such events.

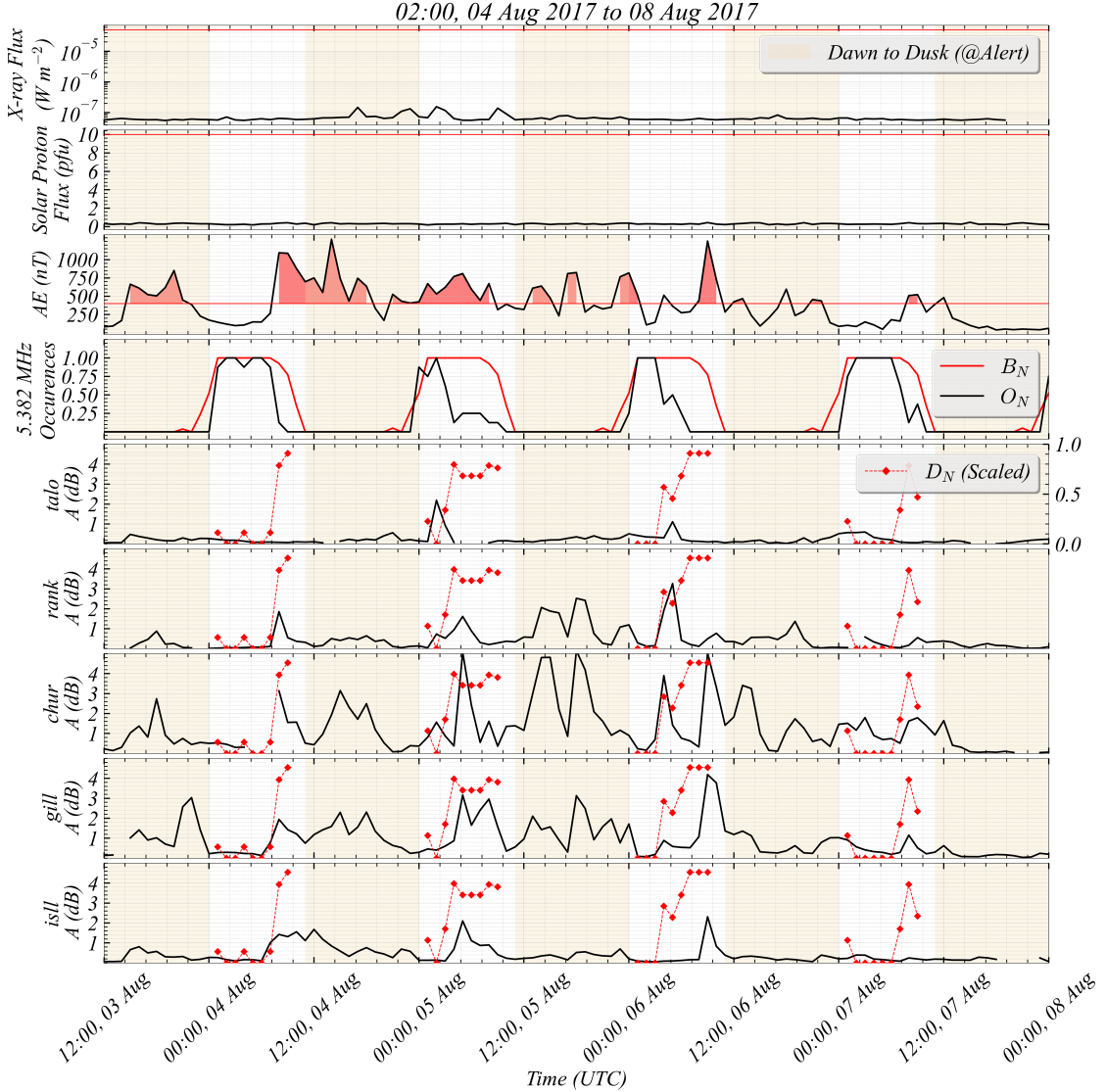


Figure 5.8: An auroral absorption event. From the top, each panel represents: OMNI AE index, 5.382 MHz occurrence and their baselines, then riometer absorption at *talo*, *rank*, *chur*, *gill* and *isll* with dropout (calculated as baseline – occurrence) overplotted for the 5.382 MHz transmissions. Dawn to dusk at Alert are highlighted in yellow, times where AE was above 400 nT are highlighted in red. Gaps in riometer data signify the data are missing.

## 5.4 Data Analysis

In the foregoing, I alluded to the futility of modelling the reception process, or the processes which lead to occurrences. A similar argument can be made for dropouts. Dropouts tend to occur together, and hence are time-dependent. Any forecasting model would have to take that dependence into account. However, for nowcasting, I take an ordinal approach. By categorizing the severity of the dropout within the hour, I divided the events dataset into 4 groups, as shown in Table 5.3. The base level (0), where less than a

quarter of the signals were lost, represents an insignificant amount of dropouts. Minor and moderate levels correspond to dropout rates in the ranges  $[0.25, 0.50)$  and  $[0.50, 0.75)$ , respectively. Above or equal to 3 quarters is considered high (3).

Dropout Level	Dropout Class	Dropouts, $D_N$
0	Quiet	$\leq 0.25$
1	Minor	$[0.25, 0.50)$
2	Moderate	$[0.50, 0.75)$
3	High	$\geq 0.75$

Table 5.3: Ordinal categorization of the dropout level as a function of dropouts.

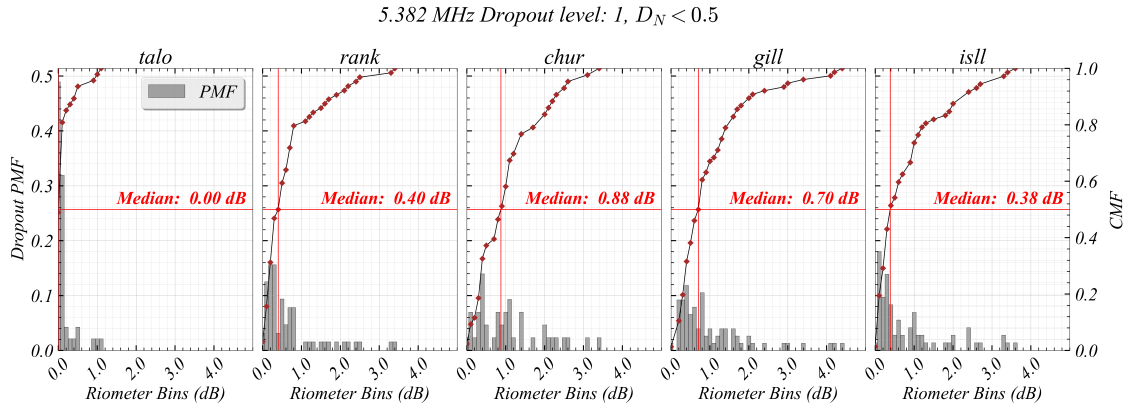


Figure 5.9: Probability Mass Function (PMF) and associated Cumulative Mass Function (CMF) of the distribution of dropouts for 5.382 MHz signal at each riometer absorption bin. The median is marked by a red cross, and is the absorption level below which (and above which) half of the dropouts occurred. Only the dropouts at the Minor class were considered.

Each dropout in the dataset occurs at a given time. At that time, each riometer measures a different level of absorption. If we tally the distribution of dropouts against riometer absorption bins (i.e., how many dropouts occur at times when the riometer measures, say, 0.5 dB absorption), we arrive at the Probability Mass Function (PMF) of dropouts at that riometer site. Shown in Figure 5.9 is the PMF for the 5.382 MHz dropouts for all the riometer sites, if only the minor, or level 1–  $[0.25, 0.5)$ , dropouts were considered. The associated Cumulative Mass Function (CMF) is the aggregate of the PMF. For example, if we add all the probabilities of the riometer bins for *rank*, up to 0.4 dB, the sum is equal to 0.5, and is therefore the median of the distribution. At *rank*, therefore, half of the dropouts at the minor level occurred before 0.4 dB– and consequently, the other half occurred above that level of absorption, since the entire distribution sums to 1. Taking these CMFs for each riometer site and each dropout level for the 5.382 MHz dropouts produces the CMF surfaces in Figure 5.10. The median for each CMF is marked by a red diamond, and its value is displayed.

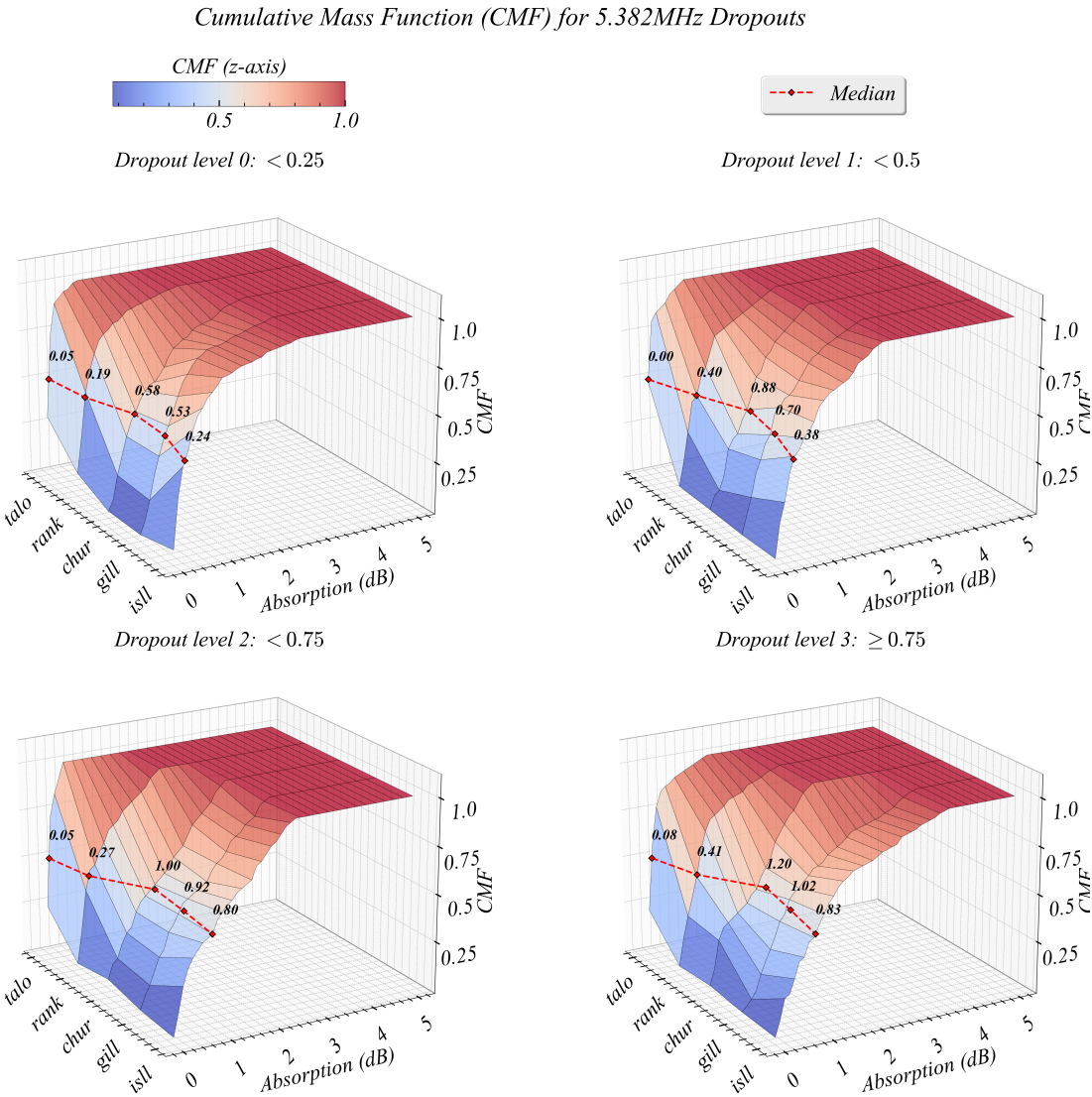


Figure 5.10: The cumulative mass functions surface for the distribution of dropouts (z-axis and colorbar) at different levels as a function of riometer absorption (x-axis) at different sites (y-axis). The median for each distribution is shown as a red diamond.

Figure 5.10, shows that, at times of dropouts, *talo* measures almost no absorption and that *RANK* measures relatively low absorption with little variance for the median between the different levels. To investigate the differences between riometer measurements at each level for the 5.382 MHz occurrences, I performed an Analysis of Variance. The results in Table 5.4 confirm that *talo* does not show differences for riometer measurements between the different dropout rates. Additionally, at the 99% significance level, *rank*'s statistic is borderline insignificant. To note is the high percentage of missing data points for *talo*, *rank* and *chur*, calculated to be around 42%, 20%, and 45%, as compared to the low percentages for *gill* and

*isll*, namely 2% and 7%, respectively, relative to the total number of dropout data points,  $N_{5.382 \text{ MHz}} = 522$ . The riometers at *talo* and *rank* not correlating with dropouts suggests that somewhere on the trans-auroral path, either at or past the boundary of the auroral zone, riometers do not measure significant absorption at times of dropouts. The results indicate that, during AA events, the magnitude of measured absorption scales upward with the riometer's proximity to the middle of the auroral zone.

	<i>talo</i>	<i>rank</i>	<i>chur</i>	<i>gill</i>	<i>isll</i>
<b>F-statistic</b>	2.30	3.46	5.80	15.41	13.04
<b>p-value</b>	$7.83 \times 10^{-2}$	$1.64 \times 10^{-3}$	$7.64 \times 10^{-4}$	$1.38 \times 10^{-9}$	$3.48 \times 10^{-8}$
<b>N</b>	258	384	264	486	459

Table 5.4: Analysis of Variance (ANOVA) for riometer measurements at different dropout levels at 5.382 MHz. Shown are the F-statistic, associated p-value, and the number of samples, **n**, for each riometer.

If, excluding *talo* and *rank*, the median curves for each dropout level from Figure 5.10 are taken for each frequency, we arrive at Figure 5.11. The increase in the number of significant ( $\geq 0.75$  dropout rate) dropouts at the high frequencies is a strong indication that propagation phenomena are confounding the results. For example, MUF depression would incur dropouts that do not necessarily occur at times where riometers measure high absorption. A combination of both MUF depression and absorption maximizes dropouts above the MUF. Besides MUF depression, during AA events, it is known that both an increase in LUF (S. E. Milan et al., 1998; Uryadov et al., 2019), which is mostly accounted for by absorption, and a decrease in MUF take effect (Blagoveshchenskii, 2020; S. Milan et al., 1994; S. E. Milan et al., 1998; Uryadov et al., 2019).

In Figure 5.11, for all dropout levels ( $> 0$ ), the median increases up to a frequency where MUF depression starts to take effect, decreases to where the effect maximizes, and gradually rises again. The results indicate that the MUF can decrease to up to at least 6.9285 MHz. The double maxima for the median in Figure 5.11 (levels  $> 0$ ) are therefore associated with points where:

1. The frequency is low enough to be significantly impacted by absorption but is not affected by a decrease in the MUF.
2. The frequency is high enough to be impacted the least by absorption even when it is impacted by MUF depression.

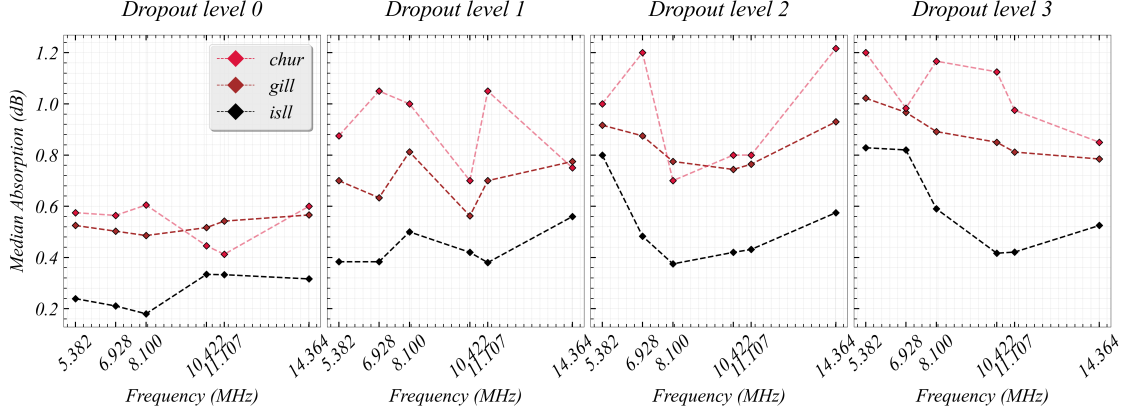


Figure 5.11: Median absorption level at *chur*, *gill*, and *isll* as a function of frequency for different dropout levels. *chur*'s lines are opaque to indicate its missing 45% of the events' data.

## 5.5 Discussion

### 5.382 MHz Median Absorption at Each Dropout Level

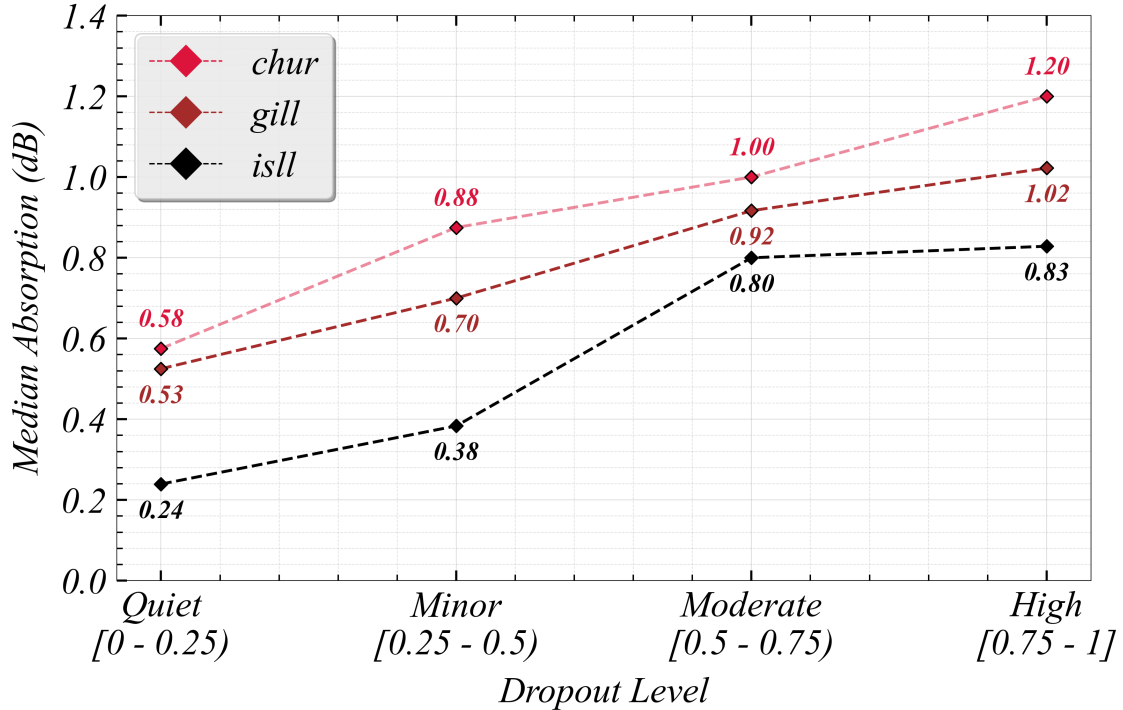


Figure 5.12: Median absorption as a function of dropout level for 5.382 MHz for *chur*, *gill*, and *isll*.

Although one might expect that higher frequencies have higher median levels of absorption (i.e., dropouts for the high frequencies occur at times of higher levels of absorption), the results deviate from this expectation. Presented above (Section 5.4) is strong evidence that the higher frequencies are fading out at times when the riometer absorption is not necessarily high. If more dropouts at a certain level occur at times of

low absorption then the median absorption level (for that frequency) increases. Therefore, some variables are conflating the results as shown in Figure 5.11, which is expected, since the MUF can be depressed before the onset of an AA event and sometimes at the recovery phase, when riometer absorption is low (Danilov et al., 2003; R. A. D. Fiori et al., 2022; Uryadov et al., 2019).

Since the lower frequencies are more susceptible to absorption as they traverse the D region on their way to the receiver, I restrict myself to the 5.382 MHz transmissions and their dropouts for establishing riometer thresholds. The median absorption as a function of dropout level for 5.382 MHz is displayed in Figure 5.12. The traced curves represent sigmoids, the scale of which is higher for riometers closer to the middle of the auroral zone. For riometers at *isll*, *gill* and *chur*, absorption levels of 0.38, 0.70 and 0.88 dB are to be considered significant, respectively, and are indicative of AA.

Physically, the correlation between riometer absorption and HF dropouts is not expected to be one-to-one, because the riometer is sensitive to 30 MHz absorption, which is a function of the electron density enhancement overhead. When the injected electrons drift away, the local absorption subsides. However, the HF radiowave path might still be affected. AA is also patchy, which limits the correlation between any one riometer and the degree of dropout. The location of the riometer is therefore crucial, and multiple riometers spread across the auroral zone are best for a trans-auroral link such as the one used in this study. The results suggest that somewhere past the auroral zone, I am unable to establish proxies for HF dropouts using riometers. If riometers are to be deployed, it is best to space them out in latitude, such that the boundary of area which most correlates with HF dropouts can be detected, and should coincide, roughly, with the auroral zone.

Besides MUF depression, considered to be a “negative effect” of the ongoing geomagnetic activity during an event, there are “positive” effects. For example, HF enhancements can (though are less likely to) occur. Studies report electron density enhancements in the F region prior to the onset of the ensuing geomagnetic activity (Blagoveshchensky & Kalishin, 2009; Danilov, 2013; Uryadov et al., 2019). HF waves can propagate via the auroral E region in the oval during AA events, which leads to an increase in the MUF, effectively increasing the available HF band (Blagoveshchenskii, 2020; S. E. Milan et al., 1997; Uryadov et al., 2019). For this reason, I restricted myself to a subset of events with HF fadeouts. To clarify, within this subset, there were instances when more signals were received than anticipated. An enhancement would fall under the Quiet category of Table 5.3. The occurrence rate for these enhancements within the events subset I chose does not exceed 2% for any frequency, and, as such, do not significantly alter the results. I discuss enhancements further in Section 6.2.1.

# Chapter 6

# Conclusions and Future Work

## 6.1 Conclusions

Through my thesis work I have shown how riometers can be used to quantify the spatial extent of D-region electron density enhancements as well as how riometer absorption can serve as an element of nowcasting spaceweather alerts.

### **Remote Sensing D-region Electron Density Enhancements**

Prototype data from the SWAN Hyper-Spectral Riometers have proven capable of capturing a time-series of power from known terrestrial transmitters in addition to nominal cosmic noise. In combination with cosmic absorption and ray tracing, I use a simple methodology to analyze HF link status information and derive a minimum size of the D-region enhancement under certain assumptions discussed in Section 4.6.

### **Riometer Absorption Thresholds**

This study analyzed data from riometers at Taloyoak, Rankin Inlet, Churchill, Gillam, and Island Lake, and HF radio-link data for a trans-auroral path from Ottawa to Alert during 28 AA events. The results suggest that somewhere past the auroral zone, I am unable to establish proxies for HF dropouts using riometers, indicating that the significance of a riometer's position depends on the HF-path and proximity to the auroral zone. For absorption thresholds, the riometer's location must be considered. Additionally, I find lower-frequency links to be more suitable for establishing riometer absorption proxies, namely, the 5.382 MHz transmissions were used. For a riometer at Island Lake, Gillam, and Churchill, absorption levels higher than 0.38, 0.70, and 0.88 dB are to be considered significant, and should be used as proxies for AA.

## 6.2 Future Work

To continue where I last left off, in the discussion of my second project (Section 5.5), I made mention of HF enhancements. In my studies, such enhancements occurred multiple times, and, using both (or either separately) the HSRs and the GO riometers, one can potentially analyze these events. In the following, I showcase the relevance of such events to the work done in Chapters 5 and 4, in that order, to aid transition the reader from the last discussion to this topic.

### 6.2.1 HF Enhancements

Figure 3.11 in Section 3.3.1 showed that the SNR for the 5.382 and 6.9285 MHz signals was enhanced roughly around 6 UTC. Below, in Figure 6.1, is the riometer voltage from *talo*, *rank*, and *chur*, for that day. One clearly observes absorption around that same time. The reason and mechanisms driving such enhancement can be potentially studied.

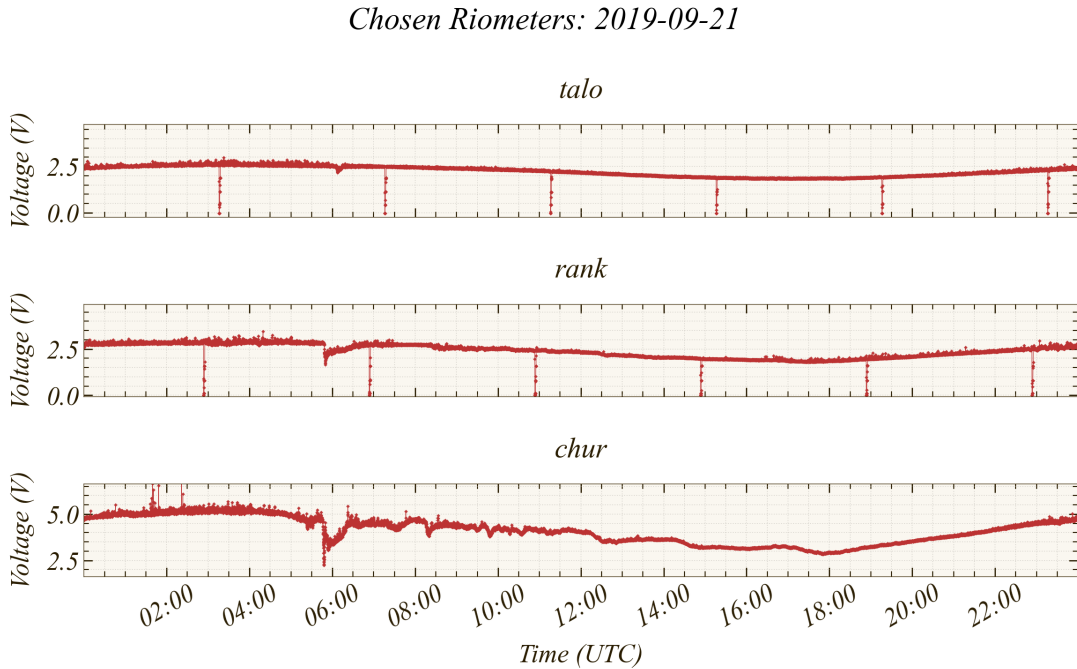


Figure 6.1: Riometer on the path of the HF-link from OTTW to ALRT showing absorption at the time of signal enhancement.

One can also observe enhancements in HSR data. During the initial testing stage, an HSR installed at Gillam, Manitoba, observed an event similar to those described in Section 5.1 on the 21 November 2019, shown in Figure 6.2. Using a similar methodology to that in Chapter 4, I investigated this event. I found

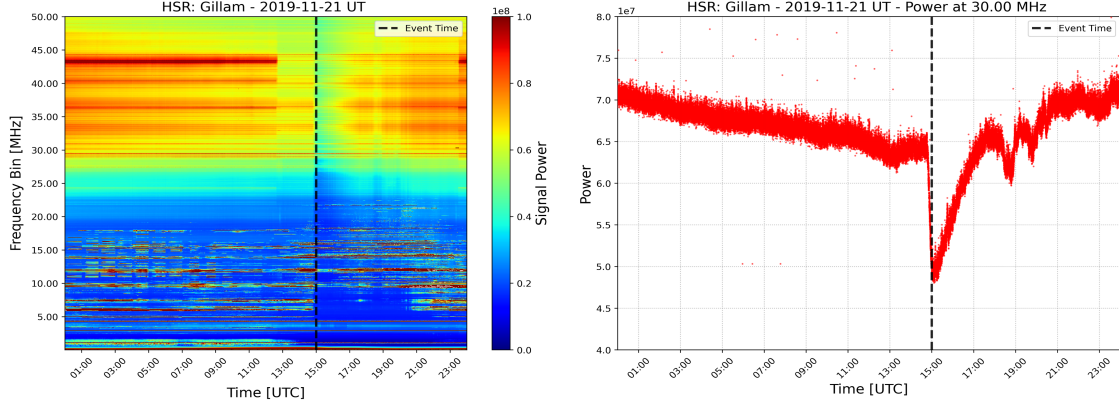


Figure 6.2: Early observations of an AA event at an HSR in Gillam (GILL). The full spectrum data is shown on the left. The event occurs at about 15 UTC, as shown in the 30 MHz power plot on the right.

both absorption of the lower frequencies and enhancements of the higher frequencies, as shown in Figure 6.3. The WWV/WWVH links at 5 MHz completely fade, while those at 10 and 15 MHz come online during the event. For CHU, the link at 7.85 MHz is lost during the event, but that at 14.67 MHz is received only during the event.

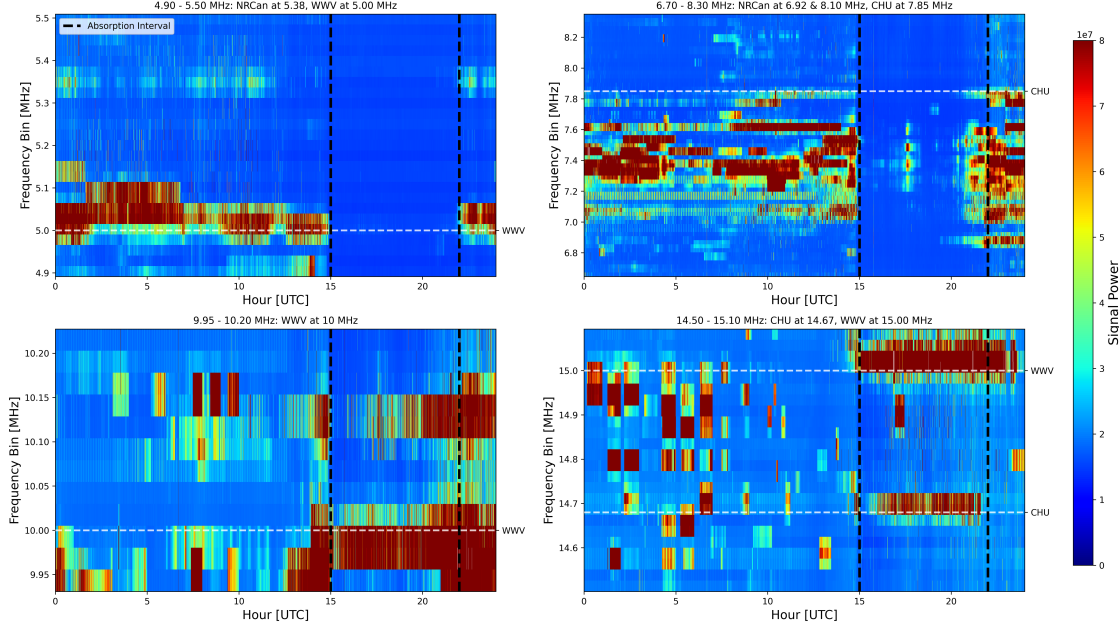


Figure 6.3: Zoomed in plots on parts of the spectrogram in Figure 6.2, showcasing the loss of the 5 MHz WWV/WWVH link (top left) and the 7.85 MHz CHU link (top right) in contrast with the enhancement of the WWV/WWVH link at 10 MHz (bottom left) and 15 MHz (bottom right). The CHU link at 14.67 MHz is also enhanced (bottom right).

Another event on 2 August 2021, the spectrum and 30.5 MHz signal of which were previously shown in

Figure 3.7, in Section 3.2.2, showed enhancements for the low-power NRCan signals. During the absorption at 20 UTC, NRCan transmissions at 11.107 MHz were received, as shown in Figure 6.4. The times of receptions were manually inspected and superimposed on a plot of HSR absorption at 30 MHz as a function of time, as displayed in Figure 6.5.

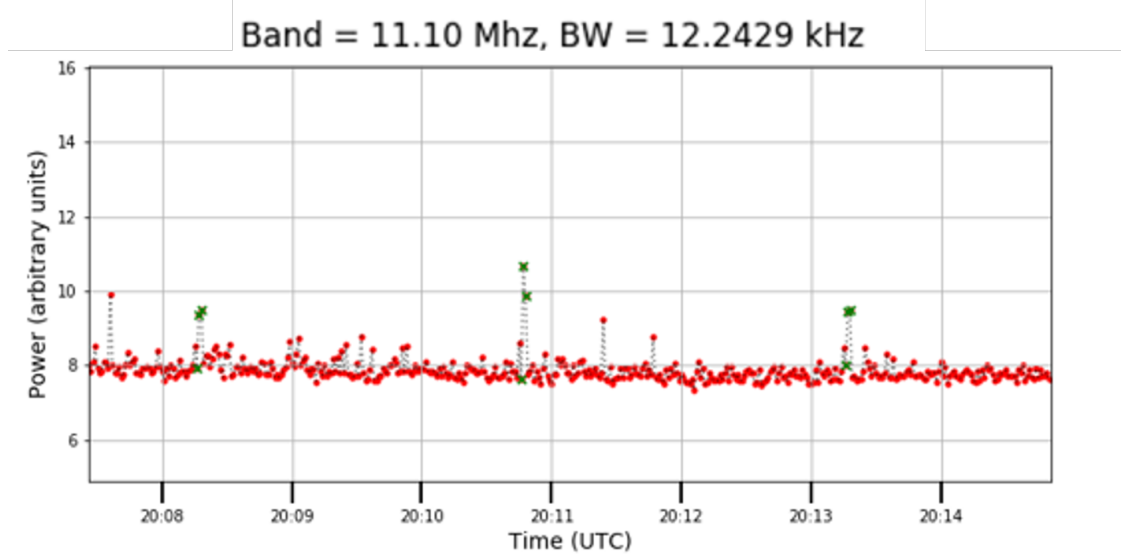


Figure 6.4: Example showing HF enhancements at the 11.107 MHz band as shown in the HSR data (red) via the green markers, which shows reception during the time of the event.

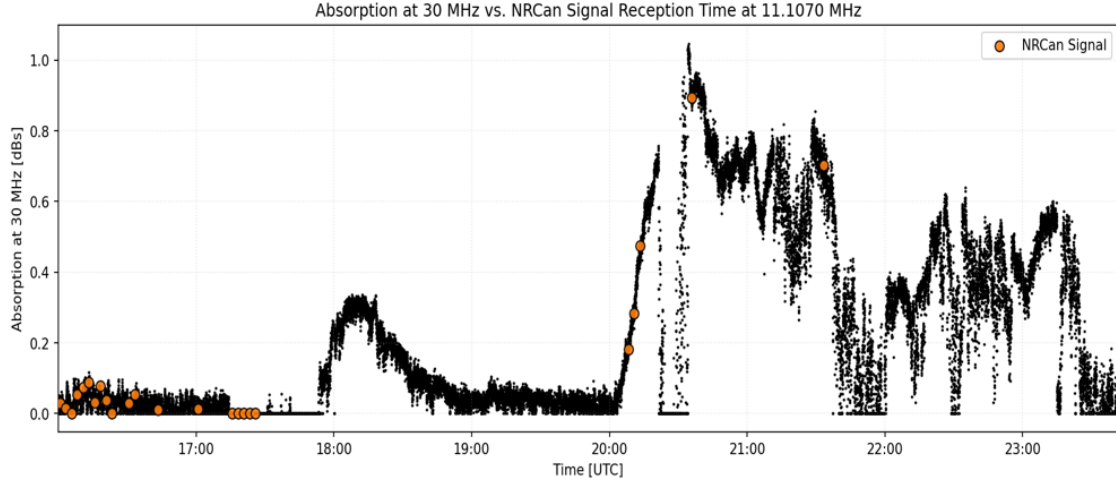


Figure 6.5: Absorption vs. time for the same day (2 August 2021), showing receptions at 11.107 MHz as yellow dots, showcasing enhancement during the rise to the peak absorption level.

The enhancement of the 11.107 MHz from NRCan's transmitter is contrasted by the loss of the 14.67 MHz signals from CHU, as shown in the full spectrum plot in Figure 6.6. The absorption, overplotted in white, is high when the signal power is low, indicating a negative correlation. Thus, riometer absorption

might indicate the loss of some signals, but the enhancement of others, depending on the location of the transmitter and the frequency used.

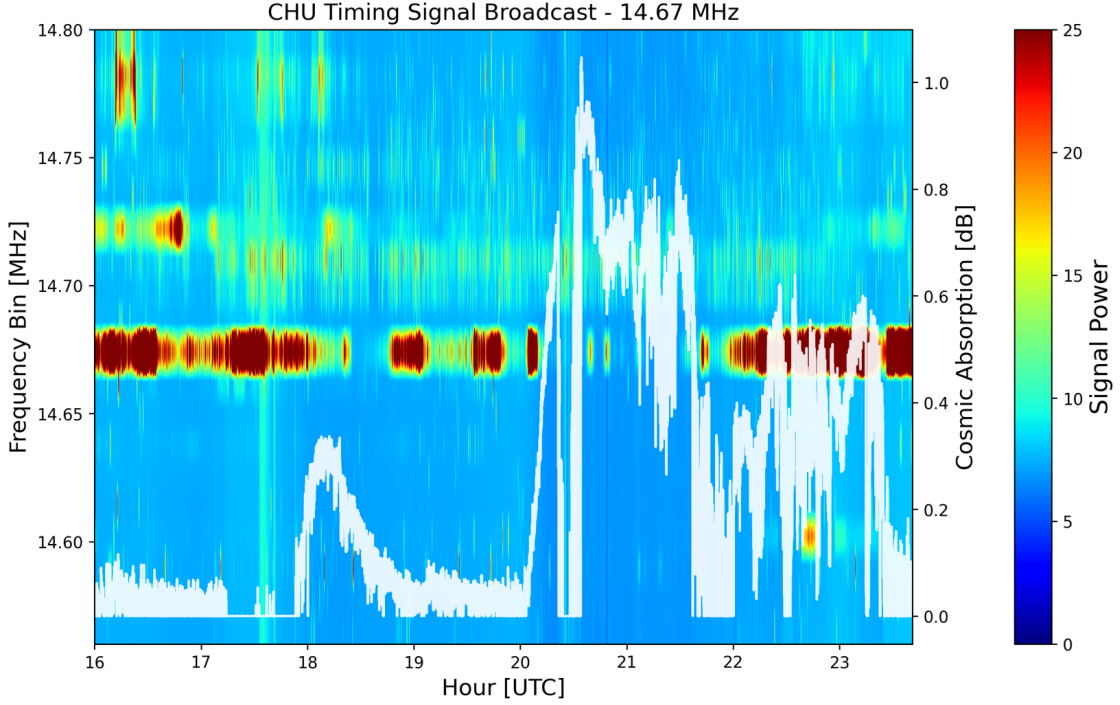


Figure 6.6: CHU signal absorption during the 2 August 2021 event.

For another event, observed from an HSR at MEAN at 3 February 2022, showcased in Figure 6.7, I opted for a statistical approach instead of manual inspection for identifying receptions. The 10<sup>th</sup> percentile of power measurements in each 7.5 min transmission cycle is taken as the noise floor. The power in the appropriate frequency bin at the expected time of transmission, according to NRCan's schedule (the schedule changed over time, and I kept track of these changes in .json files) at that time, is compared to the noise floor to calculate the SNR. The distribution of SNR values for each transmitted pulse from each of the receivers at Yellowknife (YKN), Ottawa (OTT) and Fort Churchill (FCC), are displayed in Figure 6.8. An SNR of > 1 dB constitutes reception. Receptions for the 11.107 and 14.3644 MHz are overplotted on the HSR signal at 30 MHz and shown in Figure 6.9. Some enhancements can be seen during times of AA, at about 9 UTC, for the 14.3644 MHz signal.

I think the HSRs and the GO riometers can be used to study these enhancements. Future work with NRCan can involve their HF datasets to study not only signal loss but also signal reception during disturbed times.

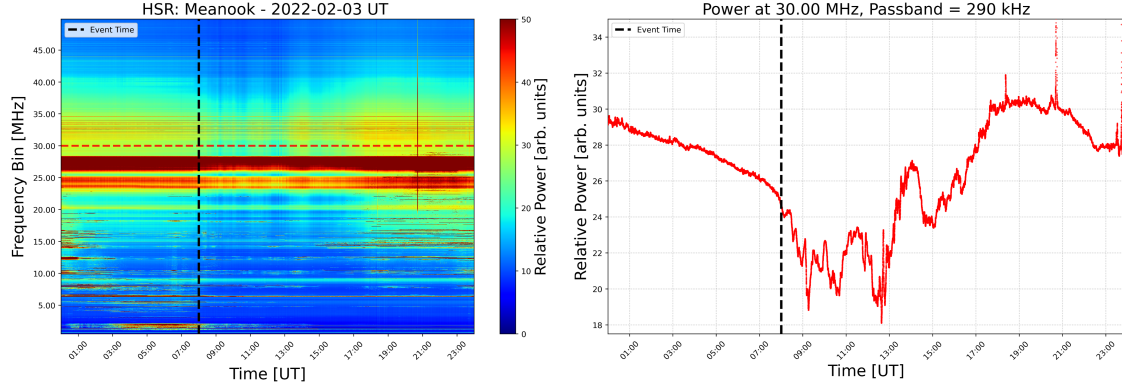


Figure 6.7: Another, more sporadic, AA event on 3 February 2022. Data shown is from an HSR at MEAN, with the full spectrogram on the left and the 30 MHz signal power is shown on the right. Event onset is shown via the dashed black line.

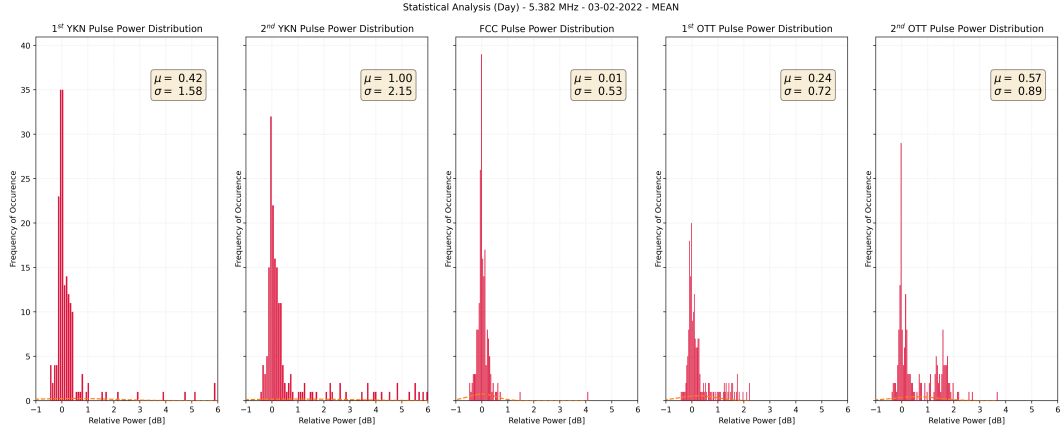


Figure 6.8: The distribution of SNR for each pulse in the NRCan transmission schedule (active during the 3 February 2022 event) for the 5.382 MHz signal. The mean,  $\mu$ , and standard deviation,  $\sigma$  is highest for the 2<sup>nd</sup> pulse from the Yellowknife transmitter.

### 6.2.2 Frequency Dependence

In my work with the HSRs, I was tasked with baselining the instrument. Some of the work I have done is shown in **Appendix B**. Part of the benefit to having multiple frequencies is that, by finding baselines and calculating absorption at various frequencies, one can, in principle, use the previously derived relationship (equation 2.31)

$$A(dB) = 4.611 \times 10^{-5} \int \frac{N_e \nu}{\omega^2 + \nu^2} dh,$$

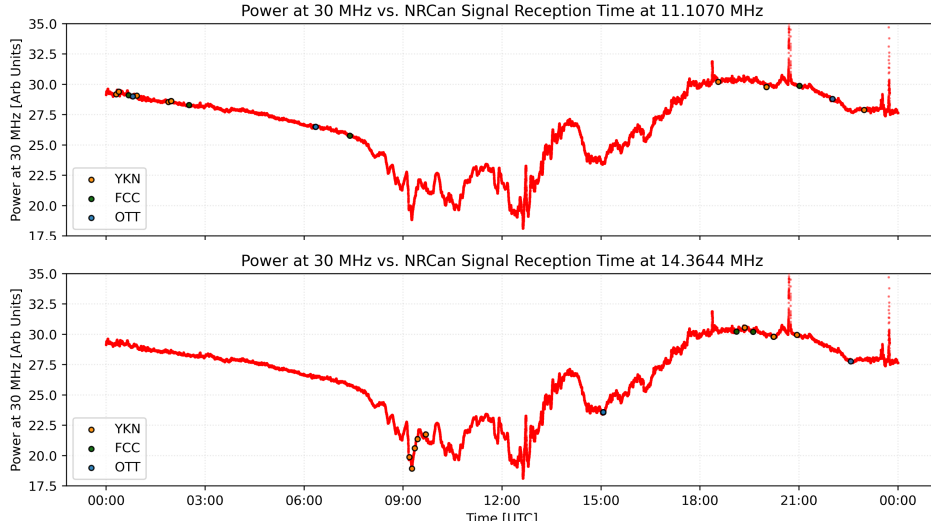


Figure 6.9: Raw signal power at 30 MHz is shown in red with receptions from each transmitter superimposed on top. 14.3644 MHz transmissions are enhanced during the event, around 9 UTC.

to derive the electron density profile,  $N_e(h)$ . After calculating many baselines, I failed to observe the proportionality derived in Section 2.3:

$$A(dB) \propto \frac{1}{\omega^2} \int N_e \nu \, dh.$$

Rather, I observed that, at 30 MHz and beyond the relationship seems to hold. Somewhere below 30 MHz, I start observing less absorption (see Section B.2). I repeated this baselining procedure for PFRR, RABB and MEAN, to no avail.

Much later, during my visit to NRCan to collaborate on my second project (Chapter 5), I learned that Dr. Robyn Fiori was finding a similar observation during her research. The  $\frac{1}{f^2}$  relationship broke down for the lower frequencies (R.A.D Fiori, private communication). Further research into this area is needed and would contribute significantly to the HF radiowave propagation literature.

### **6.2.3 Link Status and D-region Electron Density using HSRs**

While only in the prototype stage, the methodology described in Chapter 4 could be utilized in future studies to explore the evolution of the HF environment in consort with more advanced models of the ionospheric electron density and leveraging the known response of the riometer to D-region electron density enhancements. Having the two capabilities on a unified platform, from an extended array of riometers, will provide significant information about overall spatial extent with numerous intersecting terrestrial signal paths for validation. Details of the time of signal loss for different frequencies in comparison to the onset of overhead cosmic absorption could also provide information about the motion of D-region electron enhancements prior to complete terrestrial signal loss. Future work will include further exploration of the signal timings for events with multiple riometers when there is observed motion between two riometers.

## References

- Abdu, M. A. (1971, November). On the possible relationship between substorm electron drift and cosmic noise absorption on the morning side of the auroral zone. *Journal of Atmospheric and Terrestrial Physics*, 33(11), 1703–1710. Retrieved 2023-05-23, from <https://www.sciencedirect.com/science/article/pii/0021916971902182> doi: 10.1016/0021-9169(71)90218-2
- Akasofu, S.-I. (1981). Auroral Arcs and Auroral Potential Structure. In *Physics of Auroral Arc Formation* (pp. 1–14). American Geophysical Union (AGU). Retrieved 2023-05-25, from <https://onlinelibrary.wiley.com/doi/abs/10.1029/GM025p0001> (\_eprint: <https://onlinelibrary.wiley.com/doi/pdf/10.1029/GM025p0001>) doi: 10.1029/GM025p0001
- Aminaei, A., Honary, F., Kavanagh, A. J., Spanswick, E., & Viljanen, A. (2006, August). Characteristics of night-time absorption spike events. *Annales Geophysicae*, 24(7), 1887–1904. Retrieved 2024-05-15, from <https://angeo.copernicus.org/articles/24/1887/2006/> (Publisher: Copernicus GmbH) doi: 10.5194/angeo-24-1887-2006
- Appleton, S. E., & Piggott, W. R. (1954, January). Ionospheric absorption measurements during a sunspot cycle. *Journal of Atmospheric and Terrestrial Physics*, 5(1), 141–172. Retrieved 2024-05-17, from <https://www.sciencedirect.com/science/article/pii/002191695490029X> doi: 10.1016/0021-9169(54)90029-X
- Baker, D. N., Hoxie, V., Zhao, H., Jaynes, A. N., Kanekal, S., Li, X., & Elkington, S. (2019). Multiyear Measurements of Radiation Belt Electrons: Acceleration, Transport, and Loss. *Journal of Geophysical Research: Space Physics*, 124(4), 2588–2602. Retrieved 2023-05-31, from <https://onlinelibrary.wiley.com/doi/abs/10.1029/2018JA026259> (\_eprint: <https://agupubs.onlinelibrary.wiley.com/doi/pdf/10.1029/2018JA026259>) doi: 10.1029/2018JA026259
- Baker, D. N., Stauning, P., Hones Jr., E. W., Higbie, P. R., & Belian, R. D. (1981). Near-equatorial, high-resolution measurements of electron precipitation at L 6.6. *Journal of Geophysical Research: Space Physics*, 86(A4), 2295–2313. Retrieved 2022-05-12, from <https://onlinelibrary.wiley.com/doi/abs/10.1029/JA086iA04p02295> (\_eprint: <https://onlinelibrary.wiley.com/doi/pdf/10.1029/JA086iA04p02295>) doi: 10.1029/JA086iA04p02295
- Berkey, F. T., Driatskiy, V. M., Henriksen, K., Hultqvist, B., Jelly, D. H., Shchuka, T. I., ... Ylindemi, J. (1974, February). A synoptic investigation of particle precipitation dynamics for 60 substorms in IQSY (1964–1965) and IASY (1969). *Planetary and Space Science*, 22(2), 255–307. Retrieved 2023-05-18, from <https://www.sciencedirect.com/science/article/pii/0032063374900282> doi:

10.1016/0032-0633(74)90028-2

- Bilitza, D., Altadill, D., Truhlik, V., Shubin, V., Galkin, I., Reinisch, B., & Huang, X. (2017). International Reference Ionosphere 2016: From ionospheric climate to real-time weather predictions. *Space Weather*, 15(2), 418–429. Retrieved 2022-05-21, from <https://onlinelibrary.wiley.com/doi/abs/10.1002/2016SW001593> (\_eprint: <https://onlinelibrary.wiley.com/doi/pdf/10.1002/2016SW001593>) doi: 10.1002/2016SW001593
- Birch, M. J., Hargreaves, J. K., & Bromage, B. J. I. (2013, December). Properties of auroral radio absorption patches observed in the morning sector using imaging riometer and incoherent-scatter radar. *Journal of Atmospheric and Solar-Terrestrial Physics*, 105-106, 262–272. Retrieved 2023-04-11, from <https://www.sciencedirect.com/science/article/pii/S1364682612003021> doi: 10.1016/j.jastp.2012.12.004
- Blagoveshchenskii, D. V. (2020, May). Features of High-Frequency Radio Wave Propagation on Auroral Paths at Different Geomagnetic Activity. *Geomagnetism and Aeronomy*, 60(3), 335–344. Retrieved 2022-05-13, from <https://doi.org/10.1134/S0016793220030020> doi: 10.1134/S0016793220030020
- Blagoveshchensky, D. V., & Kalishin, A. S. (2009, April). Increase in the critical frequency of the ionospheric F region prior to the substorm expansion phase. *Geomagnetism and Aeronomy*, 49(2), 200–209. Retrieved 2022-08-12, from <https://doi.org/10.1134/S0016793209020091> doi: 10.1134/S0016793209020091
- Blagoveshchensky, D. V., Sergeeva, M. A., & Vystavnoi, V. M. (2006, March). Effects of substorms during HF propagation in the auroral oval. *Geomagnetism and Aeronomy*, 46(2), 166–172. Retrieved 2022-05-13, from <https://doi.org/10.1134/S0016793206020058> doi: 10.1134/S0016793206020058
- Bland, E., Bozóki, T., & Partamies, N. (2022). Spatial extent of the energetic electron precipitation region during substorms. *Frontiers in Astronomy and Space Sciences*, 9. Retrieved 2023-04-11, from <https://www.frontiersin.org/articles/10.3389/fspas.2022.978371>
- Bland, E., Tesema, F., & Partamies, N. (2021, February). D-region impact area of energetic electron precipitation during pulsating aurora. *Annales Geophysicae*, 39(1), 135–149. Retrieved 2023-04-11, from <https://angeo.copernicus.org/articles/39/135/2021/> (Publisher: Copernicus GmbH) doi: 10.5194/angeo-39-135-2021
- Boteler, D. H. (2019). A 21st Century View of the March 1989 Magnetic Storm. *Space Weather*, 17(10), 1427–1441. Retrieved 2024-05-21, from <https://onlinelibrary.wiley.com/doi/abs/10.1029/2019SW002278> (\_eprint: <https://onlinelibrary.wiley.com/doi/pdf/10.1029/2019SW002278>) doi: 10.1029/2019SW002278
- Budden, K. G. (1985). *The Propagation of Radio Waves: The Theory of Radio Waves of Low Frequency*. London: Pergamon Press.

*Power in the Ionosphere and Magnetosphere.* Cambridge: Cambridge University Press. Retrieved 2024-05-29, from <https://www.cambridge.org/core/books/propagation-of-radio-waves/BD8F03DDFEC9E2D3ABB1CAD7DEF3B91A> doi: 10.1017/CBO9780511564321

Burns, C. J., Howarth, W. G., & Hargreaves, J. K. (1990, March). High-resolution incoherent scatter radar measurements during electron precipitation events. *Journal of Atmospheric and Terrestrial Physics*, 52(3), 205–218. Retrieved 2023-05-24, from <https://www.sciencedirect.com/science/article/pii/0021916990901246> doi: 10.1016/0021-9169(90)90124-6

Cameron, T. G., Fiori, R. A. D., Warrington, E. M., Stocker, A. J., Thayaparan, T., & Danskin, D. W. (2021, August). Characterization of high latitude radio wave propagation over Canada. *Journal of Atmospheric and Solar-Terrestrial Physics*, 219, 105666. Retrieved 2023-01-31, from <https://www.sciencedirect.com/science/article/pii/S1364682621001231> doi: 10.1016/j.jastp.2021.105666

Canada, N. R. C. (2019, March). *NRC shortwave station broadcasts (CHU)*. Retrieved 2024-06-11, from <https://nrc.canada.ca/en/certifications-evaluations-standards/canadas-official-time/nrc-shortwave-station-broadcasts-chu> (Last Modified: 2019-03-23)

Cannon, P. S. (2009). Mitigation and exploitation of the ionosphere: A military perspective. *Radio Science*, 44(1). Retrieved 2022-05-13, from <https://onlinelibrary.wiley.com/doi/abs/10.1029/2008RS004021> (\_eprint: <https://onlinelibrary.wiley.com/doi/pdf/10.1029/2008RS004021>) doi: 10.1029/2008RS004021

Clilverd, M. A., Rodger, C. J., Brundell, J., Bähr, J., Cobbett, N., Moffat-Griffin, T., ... Menk, F. W. (2008). Energetic electron precipitation during substorm injection events: High-latitude fluxes and an unexpected midlatitude signature. *Journal of Geophysical Research: Space Physics*, 113(A10). Retrieved 2023-04-11, from <https://onlinelibrary.wiley.com/doi/abs/10.1029/2008JA013220> (\_eprint: <https://onlinelibrary.wiley.com/doi/pdf/10.1029/2008JA013220>) doi: 10.1029/2008JA013220

Collis, P. N., Hargreaves, J. K., & White, G. P. (1996, December). A localised co-rotating auroral absorption event observed near noon using imaging riometer and EISCAT. *Annales Geophysicae*, 14(12), 1305–1316. Retrieved 2023-05-24, from <https://angeo.copernicus.org/articles/14/1305/1996/> (Publisher: Copernicus GmbH) doi: 10.1007/s00585-996-1305-y

Cresswell-Moorcock, K., Rodger, C. J., Kero, A., Collier, A. B., Clilverd, M. A., Häggström, I., & Pitkänen, T. (2013). A reexamination of latitudinal limits of substorm-produced energetic electron precipitation. *Journal of Geophysical Research: Space Physics*, 118(10), 6694–6705. Retrieved 2023-05-17, from <https://onlinelibrary.wiley.com/doi/abs/10.1002/jgra.50598> (\_eprint: <https://onlinelibrary.wiley.com/doi/pdf/10.1002/jgra.50598>) doi: 10.1002/jgra.50598

Danilov, A. D. (2013, August). Ionospheric F-region response to geomagnetic disturbances. *Advances*

- in Space Research*, 52(3), 343–366. Retrieved 2022-05-16, from <https://www.sciencedirect.com/science/article/pii/S0273117713002470> doi: 10.1016/j.asr.2013.04.019
- Danilov, A. D., Smirnova, N. V., Blix, T. A., Thrane, E. V., & Vanina, L. B. (2003, March). Some features of electron density behaviour in the high latitude D-region derived from *in situ* measurements. *Journal of Atmospheric and Solar-Terrestrial Physics*, 65(4), 417–427. Retrieved 2024-05-17, from <https://www.sciencedirect.com/science/article/pii/S1364682602001980> doi: 10.1016/S1364-6826(02)00198-0
- Davies, K. (1990). *Ionospheric Radio*. IET. (Google-Books-ID: qdWUKSj5PCcC)
- Detrick, D. L., & Rosenberg, T. J. (1988, January). IRIS: An imaging riometer for ionospheric studies. *Antarctic Journal of the United States; (United States)*, 23:5. Retrieved 2023-05-24, from <https://www.osti.gov/biblio/5370581>
- Devlin, T., Hargreaves, J. K., & Collis, P. N. (1986, September). Eiscat observations of the ionospheric D-region during auroral radio absorption events. *Journal of Atmospheric and Terrestrial Physics*, 48(9), 795–805. Retrieved 2023-05-24, from <https://www.sciencedirect.com/science/article/pii/0021916986900541> doi: 10.1016/0021-9169(86)90054-1
- Drevin, G. R., & Stoker, P. H. (1990). Riometer quiet day curves determined by the maximum density method. *Radio Science*, 25(6), 1159–1166. Retrieved 2024-05-15, from <https://onlinelibrary.wiley.com/doi/abs/10.1029/RS025i006p01159> (\_eprint: <https://agupubs.onlinelibrary.wiley.com/doi/pdf/10.1029/RS025i006p01159>) doi: 10.1029/RS025i006p01159
- Drevin, G. R., & Stoker, P. H. (2003). Determining riometer quiet day curves 1. The matrix method. *Radio Science*, 38(2). Retrieved 2024-05-15, from <https://onlinelibrary.wiley.com/doi/abs/10.1029/2001RS002537> (\_eprint: <https://agupubs.onlinelibrary.wiley.com/doi/pdf/10.1029/2001RS002537>) doi: 10.1029/2001RS002537
- Fiori, R. a. D., Koustov, A. V., Chakraborty, S., Ruohoniemi, J. M., Danskin, D. W., Boteler, D. H., & Shepherd, S. G. (2018). Examining the Potential of the Super Dual Auroral Radar Network for Monitoring the Space Weather Impact of Solar X-Ray Flares. *Space Weather*, 16(9), 1348–1362. Retrieved 2023-10-23, from <https://onlinelibrary.wiley.com/doi/abs/10.1029/2018SW001905> (\_eprint: <https://agupubs.onlinelibrary.wiley.com/doi/pdf/10.1029/2018SW001905>) doi: 10.1029/2018SW001905
- Fiori, R. A. D., Kumar, V. V., Boteler, D. H., & Terkildsen, M. B. (2022). Occurrence rate and duration of space weather impacts on high-frequency radio communication used by aviation. *Journal of Space Weather and Space Climate*, 12, 21. Retrieved 2023-10-04, from <https://www.swsc-journal.org/>

[articles/swsc/abs/2022/01/swsc220003/swsc220003.html](https://onlinelibrary.wiley.com/doi/abs/10.1051/swsc/2022017) (Publisher: EDP Sciences) doi: 10.1051/swsc/2022017

Frissell, N. A., Miller, E. S., Kaepller, S. R., Ceglia, F., Pascoe, D., Sinanis, N., ... Shovkopyas, A. (2014). Ionospheric Sounding Using Real-Time Amateur Radio Reporting Networks. *Space Weather*, 12(12), 651–656. Retrieved 2022-05-17, from <https://onlinelibrary.wiley.com/doi/abs/10.1002/2014SW001132> (\_eprint: <https://onlinelibrary.wiley.com/doi/pdf/10.1002/2014SW001132>) doi: 10.1002/2014SW001132

Froí, A., Galkin, I., Krankowski, A., Bilitza, D., Hernández-Pajares, M., Reinisch, B., ... García-Rigo, A. (2020, January). Towards Cooperative Global Mapping of the Ionosphere: Fusion Feasibility for IGS and IRI with Global Climate VTEC Maps. *Remote Sensing*, 12(21), 3531. Retrieved 2024-06-12, from <https://www.mdpi.com/2072-4292/12/21/3531> (Number: 21 Publisher: Multidisciplinary Digital Publishing Institute) doi: 10.3390/rs12213531

Ghaly, F., Spanswick, E., Gillies, R., Cameron, T., Skone, S., Fiori, R. a. D., & Weatherwax, A. T. (2024). Use of Terrestrial High Frequency Signals in Riometer Data to Explore the Size of D-Region Electron Density Enhancements. *Journal of Geophysical Research: Space Physics*, 129(5), e2023JA032375. Retrieved 2024-05-26, from <https://onlinelibrary.wiley.com/doi/abs/10.1029/2023JA032375> (\_eprint: <https://onlinelibrary.wiley.com/doi/pdf/10.1029/2023JA032375>) doi: 10.1029/2023JA032375

Grant, A., Shaw, G., & Ward, N. (2012, November). The Effect of Space Weather on Maritime Aids-to-Navigation Service Provision. *Annual of Navigation*, 19. doi: 10.2478/v10367-012-0005-9

Griffiths, D. J. D. J. (2017). *Introduction to electrodynamics*. Cambridge, United Kingdom ; New York, NY : Cambridge University Press. Retrieved 2024-05-16, from <http://archive.org/details/introductiontoel0000grif>

Hargreaves, J. (1968, January). Auroral motions observed with riometers: latitudinal movements and a median global pattern. *Journal of Atmospheric and Solar-Terrestrial Physics*, 30(8), 1461–1470. (MAG ID: 2095178342) doi: 10.1016/s0021-9169(68)90168-2

Hargreaves, J. (1969, August). Auroral absorption of HF radio waves in the ionosphere: A review of results from the first decade of riometry. *Proceedings of the IEEE*, 57(8), 1348–1373. (Conference Name: Proceedings of the IEEE) doi: 10.1109/PROC.1969.7275

Hargreaves, J., Chivers, H., & Nielsen, E. (1979). Properties of spike events in auroral radio absorption. *Journal of Geophysical Research: Space Physics*, 84(A8), 4245–4250. Retrieved 2023-05-18, from <https://onlinelibrary.wiley.com/doi/abs/10.1029/JA084iA08p04245> (\_eprint: <https://onlinelibrary.wiley.com/doi/pdf/10.1029/JA084iA08p04245>) doi: 10.1029/JA084iA08p04245

Hargreaves, J., & Devlin, T. (1990, March). Morning sector electron precipitation events observed by incoherent scatter radar. *Journal of Atmospheric and Solar-Terrestrial Physics*, 52(3), 193–203. (MAG ID: 2060336050 S2ID: 9e75293246448f86b391beefef595eae03c63e25) doi: 10.1016/0021-9169(90)90123-5

Hargreaves, J. K. (1980, September). D-region electron densities observed by incoherent-scatter radar during auroral-absorption spike events. *Journal of Atmospheric and Terrestrial Physics*, 42(9), 783–789. Retrieved 2023-05-24, from <https://www.sciencedirect.com/science/article/pii/0021916980900811> doi: 10.1016/0021-9169(80)90081-1

Hargreaves, J. K. (2005, February). A new method of studying the relation between ionization rates and radio-wave absorption in polar-cap absorption events. *Annales Geophysicae*, 23(2), 359–369. Retrieved 2023-10-23, from <https://angeo.copernicus.org/articles/23/359/2005/> (Publisher: Copernicus GmbH) doi: 10.5194/angeo-23-359-2005

Hargreaves, J. K., Birch, M. J., & Bromage, B. J. I. (2007, August). D- and E-region effects in the auroral zone during a moderately active 24-h period in July 2005. *Annales Geophysicae*, 25(8), 1837–1849. Retrieved 2023-05-18, from <https://angeo.copernicus.org/articles/25/1837/2007/> (Publisher: Copernicus GmbH) doi: 10.5194/angeo-25-1837-2007

Hargreaves, J. K., Browne, S., Ranta, H., Ranta, A., Rosenberg, T. J., & Detrick, D. L. (1997, May). A study of substorm-associated nightside spike events in auroral absorption using imaging riometers at South Pole and Kilpisjärvi. *Journal of Atmospheric and Solar-Terrestrial Physics*, 59(8), 853–872. Retrieved 2022-05-12, from <https://www.sciencedirect.com/science/article/pii/S1364682696000612> doi: 10.1016/S1364-6826(96)00061-2

Hargreaves, J. K., Detrick, D. L., & Rosenberg, T. J. (1991). Space-time structure of auroral radio absorption events observed with the imaging riometer at south pole. *Radio Science*, 26(4), 925–930. Retrieved 2023-04-11, from <https://onlinelibrary.wiley.com/doi/abs/10.1029/91RS00179> (eprint: <https://onlinelibrary.wiley.com/doi/pdf/10.1029/91RS00179>) doi: 10.1029/91RS00179

Hargreaves, J. K., Ranta, A., Annan, J. D., & Hargreaves, J. C. (2001). Temporal fine structure of nighttime spike events in auroral radio absorption, studied by a wavelet method. *Journal of Geophysical Research*, 106(A11), 24621. Retrieved 2023-05-29, from [https://www.academia.edu/3454478/Temporal\\_fine\\_structure\\_of\\_nighttime\\_spike\\_events\\_in\\_auroral\\_radio\\_absorption\\_studied\\_by\\_a\\_wavelet\\_method](https://www.academia.edu/3454478/Temporal_fine_structure_of_nighttime_spike_events_in_auroral_radio_absorption_studied_by_a_wavelet_method)

He, F., Hu, H., Hu, Z., & Liu, R. (2014, October). A new technique for deriving the quiet day curve from imaging riometer data at Zhongshan Station, Antarctic. *Science China Technological Sciences*, 57(10), 1967–1976. Retrieved 2024-05-16, from <https://doi.org/10.1007/s11431-014-5616-z> doi:

10.1007/s11431-014-5616-z

Hunsucker, R. D., & Hargreaves, J. K. (2003). *The high-latitude ionosphere and its effects on radio propagation*. Cambridge ; New York: Cambridge University Press.

IEEE Standard Definitions of Terms for Radio Wave Propagation. (1998). *IEEE Std 211-1997*, i-. Retrieved 2024-09-16, from <https://ieeexplore.ieee.org/stampPDF/getPDF.jsp?tp=&arnumber=705931&ref=aHR0cHM6Ly93d3cuZ29vZ2x1LmNvbS8=> (Conference Name: IEEE Std 211-1997) doi: 10.1109/IEEEESTD.1998.87897

Jones, S. L., Lessard, M. R., Rychert, K., Spanswick, E., & Donovan, E. (2011). Large-scale aspects and temporal evolution of pulsating aurora. *Journal of Geophysical Research: Space Physics*, 116(A3). Retrieved 2023-04-11, from <https://onlinelibrary.wiley.com/doi/abs/10.1029/2010JA015840> (eprint: <https://onlinelibrary.wiley.com/doi/pdf/10.1029/2010JA015840>) doi: 10.1029/2010JA015840

Kainuma, S., Ishii, M., Murayama, Y., Kikuchi, T., Mori, H., & Igarashi, K. (2001, July). Drift motion of ionospheric arc-like absorption regions observed with a 256-beam imaging riometer in Alaska. *Earth, Planets and Space*, 53(7), 753–760. Retrieved 2023-05-18, from <https://doi.org/10.1186/BF03352403> doi: 10.1186/BF03352403

Karttunen, H., Kröger, P., Oja, H., Poutanen, M., & Donner, K. J. (Eds.). (2017). *Fundamental Astronomy*. Berlin, Heidelberg: Springer. Retrieved 2024-05-16, from <http://link.springer.com/10.1007/978-3-662-53045-0> doi: 10.1007/978-3-662-53045-0

Kavanagh, A. J., Honary, F., McCrea, I. W., Donovan, E., Woodfield, E. E., Manninen, J., & Anderson, P. C. (2002, September). Substorm related changes in precipitation in the dayside auroral zone – a multi instrument case study. *Annales Geophysicae*, 20(9), 1321–1334. Retrieved 2023-05-18, from <https://angeo.copernicus.org/articles/20/1321/2002/> (Publisher: Copernicus GmbH) doi: 10.5194/angeo-20-1321-2002

Kavanagh, A. J., Marple, S. R., Honary, F., McCrea, I. W., & Senior, A. (2004, April). On solar protons and polar cap absorption: constraints on an empirical relationship. *Annales Geophysicae*, 22(4), 1133–1147. Retrieved 2023-10-23, from <https://angeo.copernicus.org/articles/22/1133/2004/> (Publisher: Copernicus GmbH) doi: 10.5194/angeo-22-1133-2004

Kikuchi, T., Yamagishi, H., & Lester, M. (1990, January). Drift of auroral absorption due to the magnetospheric convection observed with the scanning narrow beam riometer during SUNDIAL-86. *Annales Geophysicae*, 8, 431–439.

King, J. H., & Papitashvili, N. E. (2020). *OMNI 1-min Data Set*. NASA Space Physics Data Facility. Retrieved 2024-06-19, from <https://hpde.io/NASA/NumericalData/OMNI/>

[HighResolutionObservations/Version1/PT1M](#) doi: 10.48322/45BB-8792

Krishnaswamy, S., Detrick, D. L., & Rosenberg, T. J. (1985). The inflection point method of determining riometer quiet day curves. *Radio Science*, 20(1), 123–136. Retrieved 2024-05-15, from <https://onlinelibrary.wiley.com/doi/abs/10.1029/RS020i001p00123> (eprint: <https://agupubs.onlinelibrary.wiley.com/doi/pdf/10.1029/RS020i001p00123>) doi: 10.1029/RS020i001p00123

Laundal, K. M., & Richmond, A. D. (2017, March). Magnetic Coordinate Systems. *Space Science Reviews*, 206(1), 27–59. Retrieved 2024-07-09, from <https://doi.org/10.1007/s11214-016-0275-y> doi: 10.1007/s11214-016-0275-y

Little, C. G., & Leinbach, H. (1959, February). The Riometer-A Device for the Continuous Measurement of Ionospheric Absorption. *Proceedings of the IRE*, 47(2), 315–320. (Conference Name: Proceedings of the IRE) doi: 10.1109/JRPROC.1959.287299

Makarevitch, R. A., Honary, F., McCrea, I. W., & Howells, V. S. C. (2004, November). Imaging riometer observations of drifting absorption patches in the morning sector. *Annales Geophysicae*, 22(10), 3461–3478. Retrieved 2023-05-18, from <https://angeo.copernicus.org/articles/22/3461/2004/> (Publisher: Copernicus GmbH) doi: 10.5194/angeo-22-3461-2004

Malik, H., Rotake, D., & Mahajan, M. (2014, January). Design and Implementation of Bpsk Modulator and Demodulator Using Vhdl. *IOSR Journal of Electronics and Communication Engineering*, 9, 98–105. doi: 10.9790/2834-093498105

Mann, I. R., Milling, D. K., Rae, I. J., Ozeke, L. G., Kale, A., Kale, Z. C., ... Singer, H. J. (2008, December). The Upgraded CARISMA Magnetometer Array in the THEMIS Era. *Space Science Reviews*, 141(1), 413–451. Retrieved 2024-06-20, from <https://doi.org/10.1007/s11214-008-9457-6> doi: 10.1007/s11214-008-9457-6

McRae, W. M., & Thomson, N. R. (2004, January). Solar flare induced ionospheric D-region enhancements from VLF phase and amplitude observations. *Journal of Atmospheric and Solar-Terrestrial Physics*, 66(1), 77–87. Retrieved 2023-10-24, from <https://www.sciencedirect.com/science/article/pii/S1364682603002207> doi: 10.1016/j.jastp.2003.09.009

Meeus, J. (1991). *Astronomical Algorithms*. Willmann-Bell. (Google-Books-ID: 1smAQgAACAAJ)

Milan, S., Jones, T., Warrington, E., & Reeves, G. (1994, July). Observations of substorm associated absorption events on a 3200 km high latitude HF propagation path. In *1994 Sixth International Conference on HF Radio Systems and Techniques* (pp. 69–73). doi: 10.1049/cp:19940467

Milan, S. E., Jones, T. B., & Warrington, E. M. (1997, January). Enhanced MUF propagation of HF radio waves in the auroral zone. *Journal of Atmospheric and Solar-Terrestrial Physics*, 59(2),

- 237–248. Retrieved 2022-05-13, from <https://www.sciencedirect.com/science/article/pii/S1364682696000314> doi: 10.1016/S1364-6826(96)00031-4
- Milan, S. E., Lester, M., Jones, T. B., & Warrington, E. M. (1998, April). Observations of the reduction in the available HF band on four high latitude paths during periods of geomagnetic disturbance. *Journal of Atmospheric and Solar-Terrestrial Physics*, 60(6), 617–629. Retrieved 2022-05-12, from <https://www.sciencedirect.com/science/article/pii/S1364682698000054> doi: 10.1016/S1364-6826(98)00005-4
- Mitra, A. P. (1974). *Ionospheric Effects of Solar Flares* (Vol. 46). Dordrecht: Springer Netherlands. Retrieved 2024-06-14, from <http://link.springer.com/10.1007/978-94-010-2231-6> doi: 10.1007/978-94-010-2231-6
- Neal, J. J., Rodger, C. J., & Green, J. C. (2013). Empirical determination of solar proton access to the atmosphere: Impact on polar flight paths. *Space Weather*, 11(7), 420–433. Retrieved 2024-05-17, from <https://onlinelibrary.wiley.com/doi/abs/10.1002/swe.20066> (\_eprint: <https://onlinelibrary.wiley.com/doi/pdf/10.1002/swe.20066>) doi: 10.1002/swe.20066
- Nelson, G., Lombardi, M. A., & Oskay, W. (2005, January). NIST time and frequency radio stations: WWV, WWVH, and WWVB. *NIST*. Retrieved 2024-06-11, from <https://www.nist.gov/publications/nist-time-and-frequency-radio-stations-wwv-wwvh-and-wwvb> (Last Modified: 2021-10-12T11:10-04:00 Publisher: Glenn Nelson, Michael A. Lombardi, Windell Oskay)
- Oguti, T. (1981). Tv Observations of Auroral Arcs. In *Physics of Auroral Arc Formation* (pp. 31–41). American Geophysical Union (AGU). Retrieved 2023-05-25, from <https://onlinelibrary.wiley.com/doi/abs/10.1029/GM025p0031> (\_eprint: <https://onlinelibrary.wiley.com/doi/pdf/10.1029/GM025p0031>) doi: 10.1029/GM025p0031
- Pirjola, R., Kauristie, K., Lappalainen, H., Viljanen, A., & Pulkkinen, A. (2005). Space weather risk. *Space Weather*, 3(2). Retrieved 2024-05-17, from <https://onlinelibrary.wiley.com/doi/abs/10.1029/2004SW000112> (\_eprint: <https://onlinelibrary.wiley.com/doi/pdf/10.1029/2004SW000112>) doi: 10.1029/2004SW000112
- Pudovkin, M. I., Shumilov, O. I., & Zaitzeva, S. A. (1968, July). Dynamics of the zone of corpuscular precipitations. *Planetary and Space Science*, 16(7), 881–890. Retrieved 2023-05-18, from <https://www.sciencedirect.com/science/article/pii/0032063368901128> doi: 10.1016/0032-0633(68)90112-8
- Rees, M. H. (1963, October). Auroral ionization and excitation by incident energetic electrons. *Planetary and Space Science*, 11(10), 1209–1218. Retrieved 2023-10-24, from <https://www.sciencedirect.com/science/article/pii/0032063363902526> doi: 10.1016/0032-0633(63)90252-6

- Rees, M. H. (1964, July). Note on the penetration of energetic electrons into the earth's atmosphere. *Planetary and Space Science*, 12(7), 722–725. Retrieved 2023-05-18, from <https://www.sciencedirect.com/science/article/pii/0032063364902363> doi: 10.1016/0032-0633(64)90236-3
- Ritchie, S. E., & Honary, F. (2009). Storm sudden commencement and its effect on high-latitude HF communication links. *Space Weather*, 7(6). Retrieved 2022-08-12, from <https://onlinelibrary.wiley.com/doi/abs/10.1029/2008SW000461> (\_eprint: <https://onlinelibrary.wiley.com/doi/pdf/10.1029/2008SW000461>) doi: 10.1029/2008SW000461
- Ruck, J. J., & Themens, D. R. (2021). Impacts of Auroral Precipitation on HF Propagation: A Hypothetical Over-the-Horizon Radar Case Study. *Space Weather*, 19(12), e2021SW002901. Retrieved 2023-02-27, from <https://onlinelibrary.wiley.com/doi/abs/10.1029/2021SW002901> (\_eprint: <https://agupubs.onlinelibrary.wiley.com/doi/pdf/10.1029/2021SW002901>) doi: 10.1029/2021SW002901
- Sen, H. K., & Wyller, A. A. (1960). On the generalization of the Appleton-Hartree magnetoionic formulas. *Journal of Geophysical Research (1896-1977)*, 65(12), 3931–3950. Retrieved 2024-05-17, from <https://onlinelibrary.wiley.com/doi/abs/10.1029/JZ065i012p03931> (\_eprint: <https://agupubs.onlinelibrary.wiley.com/doi/pdf/10.1029/JZ065i012p03931>) doi: 10.1029/JZ065i012p03931
- Shain, C. A. (1951). Galactic Radiation at 18.3 Mc/s. *Australian Journal of Chemistry*, 4(3), 258–267. Retrieved 2024-05-18, from <https://www.publish.csiro.au/ch/ch9510258> (Publisher: CSIRO PUBLISHING) doi: 10.1071/ch9510258
- Spanswick, E., Donovan, E., Friedel, R., & Korth, A. (2007). Ground based identification of dispersionless electron injections. *Geophysical Research Letters*, 34(3). Retrieved 2023-04-11, from <https://onlinelibrary.wiley.com/doi/abs/10.1029/2006GL028329> (\_eprint: <https://onlinelibrary.wiley.com/doi/pdf/10.1029/2006GL028329>) doi: 10.1029/2006GL028329
- Spanswick, E., Donovan, E., Liu, W., Wallis, D., Aasnes, A., Hiebert, T., ... Frey, H. (2005). Substorm Associated Spikes in High Energy Particle Precipitation. In *The Inner Magnetosphere: Physics and Modeling* (pp. 227–236). American Geophysical Union (AGU). Retrieved 2023-06-01, from <https://onlinelibrary.wiley.com/doi/abs/10.1029/155GM24> (\_eprint: <https://agupubs.onlinelibrary.wiley.com/doi/pdf/10.1029/155GM24>) doi: 10.1029/155GM24
- Tsyganenko, N. A., & Stern, D. P. (1996). Modeling the global magnetic field of the large-scale Birkeland current systems. *Journal of Geophysical Research: Space Physics*, 101(A12), 27187–27198. Retrieved 2024-07-02, from <https://onlinelibrary.wiley.com/doi/abs/10.1029/96JA02735> (\_eprint: <https://onlinelibrary.wiley.com/doi/pdf/10.1029/96JA02735>) doi: 10.1029/96JA02735

- Uryadov, V. P., Vybornov, F. I., Kolchev, A. A., Vertogradov, G. G., Sklyarevsky, M. S., Egoshin, I. A., ... Chernov, A. G. (2018, April). Impact of heliogeophysical disturbances on ionospheric HF channels. *Advances in Space Research*, 61(7), 1837–1849. Retrieved 2022-05-13, from <https://www.sciencedirect.com/science/article/pii/S0273117717304970> doi: 10.1016/j.asr.2017.07.003
- Uryadov, V. P., Vybornov, F. I., & Pershin, A. V. (2019, July). Features of the HF Signal Propagation on Oblique Sounding Paths During Solar and Magnetic Activity in September 2017. *Radiophysics and Quantum Electronics*, 62(2), 85–98. Retrieved 2022-05-13, from <https://doi.org/10.1007/s11141-019-09956-z> doi: 10.1007/s11141-019-09956-z
- van de Kamp, M., Rodger, C. J., Seppälä, A., Clilverd, M. A., & Verronen, P. T. (2018). An Updated Model Providing Long-Term Data Sets of Energetic Electron Precipitation, Including Zonal Dependence. *Journal of Geophysical Research: Atmospheres*, 123(17), 9891–9915. Retrieved 2023-05-17, from <https://onlinelibrary.wiley.com/doi/abs/10.1029/2017JD028253> (\_eprint: <https://onlinelibrary.wiley.com/doi/pdf/10.1029/2017JD028253>) doi: 10.1029/2017JD028253
- Yakovchuk, O., & Wissing, J. M. (2023). Polar particle flux distribution and its spatial extent. *Journal of Space Weather and Space Climate*, 13, 9. Retrieved 2024-06-11, from <https://www.swsc-journal.org/articles/swsc/abs/2023/01/swsc220035/swsc220035.html> (Publisher: EDP Sciences) doi: 10.1051/swsc/2023009

## Appendix A

# Proofs and Derivations

### A.1 Plasma Electric Field

In **Section 2.1.3**, the derivation for the plasma oscillation frequency starts by assuming a thin sheet of plasma has an electric field of the form

$$E = -\frac{\sigma_b}{\epsilon_0},$$

where  $\sigma_b$  is the bound surface charge density defined as

$$\sigma_b = \vec{P} \cdot \hat{n}, \tag{A.1}$$

for some polarization  $\vec{P}$  across the sheet, where  $\hat{n}$  is the unit surface normal. While that starting point provides an intuitive picture, since the field is that of a thin sheet, here, I provide a mathematical derivation of that form of the electric field.

Using the divergence theorem, we can write

$$\int_S \sigma_b \, dA = \int_V \vec{\nabla} \cdot \vec{P} \, dV \tag{A.2}$$

where  $dA$  and  $dV$  are the differential area and volume elements, respectively. Since all the electrons are bound to the ions in the plasma (and both have the same density on average—quasi-neutrality),

$$\vec{\nabla} \cdot \vec{P} = -\rho_b = -\rho, \tag{A.3}$$

where  $\rho_b$  is the bound charge density, and  $\rho$  is the total charge density. Therefore, we can rewrite equation A.2 as

$$\int_S \sigma_b \, dA = - \int_V \rho \, dV.$$

Dividing both sides by the permittivity of free space,  $\epsilon_0$ , we have

$$\frac{1}{\epsilon_0} \int_S \sigma_b \, dA = - \frac{Q}{\epsilon_0},$$

where  $Q$  is the total charge. Using **Gauss's Law** in integral form, we have

$$\int_S \frac{\sigma_b}{\epsilon_0} \, dA = - \int_S \vec{E} \cdot \hat{n} \, dA,$$

or,

$$\boxed{E = -\frac{\sigma_b}{\epsilon_0}}.$$

From here, the derivation for the plasma oscillation frequency follows as in **Section 2.1.3**.

## A.2 Evanescent Waves

This section discusses why evanescent waves are non-propagating waves. I discuss the energy of the wave in A.2.1 and why it is reflected in A.2.2. These derivations are based off Griffiths (2017).

### A.2.1 Poynting Flux

The Poynting Flux vector of a monochromatic plane electromagnetic wave is given by:

$$\vec{S} = \frac{1}{\mu} \vec{E} \times \vec{B}, \quad (\text{A.4})$$

where  $\vec{E} = \text{Re}\{\tilde{E}\} = \text{Re}\{\tilde{E}_0 e^{i(\tilde{k} \cdot \vec{r} - \omega t)}\}$ ,  $\mu$  is the permeability of the medium, and the justification for plane-wave geometry is that a spherical wave would expand by the time it reaches the ionosphere. A similar argument can be made for the ionosphere itself, whose radius of curvature is high enough even at its lower-most layers to be considered a plane. Therefore, considering a unit wave normal,  $\hat{k}$ , in the  $\hat{z}$  direction, we can rewrite the Poynting Flux as

$$\vec{S} = \frac{1}{\mu} E_0 e^{-\kappa z} \cos(kz - \omega t + \delta_E) \hat{x} \times B_0 e^{-\kappa z} \cos(kz - \omega t + \delta_E + \phi) \hat{y},$$

where it is implied that the wave vector,  $\vec{k}$  is complex, or  $\vec{k} = \tilde{k} = k + i\kappa$ , and  $\phi$  is the phase difference between the electric and magnetic field, which can be derived from

$$\tilde{B} = c \tilde{E} \quad (\text{A.5})$$

$$\tilde{B}_0 e^{i(\tilde{k} \cdot \vec{r} - \omega t)} = c \tilde{E}_0 e^{i(\tilde{k} \cdot \vec{r} - \omega t)}$$

$$\vec{B}_0 e^{i\delta_B} = c \vec{E}_0 e^{i\delta_E}$$

and

$$c = \frac{\tilde{k}}{\omega} = \frac{\|\tilde{k}\| e^{i\phi}}{\omega} \quad (\text{A.6})$$

when there is no refraction or in the medium. Therefore, the phase difference between the electric and magnetic field is given by

$$\vec{B}_0 e^{i\delta_B} = \frac{\|\tilde{k}\| e^{i\phi}}{\omega} \vec{E}_0 e^{i\delta_E},$$

yielding

$$e^{i\delta_B} = e^{i\phi} e^{i\delta_E},$$

or

$$\phi = \delta_B - \delta_E. \quad (\text{A.7})$$

For an evanescent wave, the wave vector is purely imaginary, and thus the expression for the Poynting Flux in **Equation A.4** becomes

$$\vec{S} = \frac{1}{\mu} E_0 B_0 e^{-2\kappa z} \cos(-\omega t + \delta_E) \cos(-\omega t + \delta_E + \phi) \hat{z},$$

which does not necessarily reduce to zero. However, the time average of  $\vec{S}$  can be written as

$$\begin{aligned} \langle \vec{S} \rangle &= \frac{E_0 B_0}{\mu} e^{-2\kappa z} \langle \cos(-\omega t + \delta_E) \cos(-\omega t + \delta_E + \phi) \rangle \hat{z} \\ \langle \vec{S} \rangle &= \frac{E_0 B_0}{\mu} e^{-2\kappa z} \cdot \frac{\cos(\phi)}{2} \hat{z} \end{aligned}$$

and the phase difference,  $\phi$ , can be retrieved from the phasor form of the wave vector:

$$\tilde{k} = \|\tilde{k}\| e^{i\phi},$$

where the argument of the phasor is given by

$$\phi = \arg(\tilde{k}) = \tan^{-1} \left( \frac{\text{Im}\{\tilde{k}\}}{\text{Re}\{\tilde{k}\}} \right) = \tan^{-1} \left( \frac{\kappa}{k} \right). \quad (\text{A.8})$$

Since  $\text{Re}\{\tilde{k}\} = 0$ ,  $\phi = \frac{\pi}{2}$ , this implies

$$\langle \vec{S} \rangle = \frac{E_0 B_0}{\mu} e^{-2\kappa z} \cdot \frac{\cos(\pi/2)}{2} \hat{z}$$

$$\therefore \boxed{\langle \vec{S} \rangle = 0}$$

### A.2.2 Total Internal Reflection

Here I outline the consequences of the **Fresnel Equation** dealing with reflection. The reflected electric field amplitude,  $\tilde{E}_R$  in terms of the incident electric field,  $\tilde{E}_I$  is given by

$$\tilde{E}_R = \left( \frac{1 - \tilde{\beta}}{1 + \tilde{\beta}} \right) \tilde{E}_I, \quad (\text{A.9})$$

where

$$\tilde{\beta} = \frac{\mu_1 v_1}{\mu_2 v_2} = \frac{\mu_1 v_1}{\mu_2 \omega} \tilde{k}_2. \quad (\text{A.10})$$

In equation A.10,  $\mu_i$  is the permeability of the  $i^{th}$  medium and  $v_i$  is the phase velocity of the wave in that medium.  $\tilde{k}$  is the wave vector, which, in general, is complex. Equation A.9 applies for the case of normal incidence on the medium. For the general case of oblique incidence we have

$$\tilde{E}_R = \left( \frac{\alpha - \tilde{\beta}}{\alpha + \tilde{\beta}} \right) \tilde{E}_I, \quad (\text{A.11})$$

where

$$\alpha = \frac{\cos(\theta_T)}{\cos(\theta_I)} \quad (\text{A.12})$$

is the ratio of the cosine of the angle of transmission,  $\theta_T$ , to that of the angle of incidence,  $\theta_I$ . Both cosine functions range from 0 to 1, hence their ratio can have extreme cases. To investigate these cases, we first use **Snell's Law**,

$$\frac{\sin(\theta_T)}{\sin(\theta_I)} = \frac{n_1}{n_2} \quad (\text{A.13})$$

where  $n_1$  is the index of refraction of the first medium and  $n_2$  of the second, to rewrite A.12 as follows:

$$\alpha = \frac{\sqrt{1 - \sin^2(\theta_T)}}{\cos(\theta_I)} = \frac{\sqrt{1 - \left( \frac{n_1}{n_2} \sin(\theta_I) \right)^2}}{\cos(\theta_I)}.$$

#### Reflection

At  $\theta_I = 0^\circ$ ,  $\alpha = 1$ , and equation A.11 yields back equation A.9, the condition for normal incidence. At  $\theta_I = 90^\circ$ , the condition for grazing incidence, the wave is reflected and  $\alpha = 0$  in A.11 yields

$$\tilde{E}_R = -\tilde{E}_I.$$

## Transmission

There is however an angle of incidence for which the reflected amplitude is zero, called Brewster's Angle,  $\theta_B$ , which occurs when  $\alpha = \beta$  (now purely real). Setting  $\alpha = \beta$  and replacing  $\theta_I$  with  $\theta_B$  in ??, we get

$$\sin^2(\theta_B) = \frac{1 - \beta^2}{\left(\frac{n_1}{n_2}\right)^2 - \beta^2} \quad (\text{A.14})$$

This is a special case for which there will be no reflected wave.

## Total Internal Reflection

In the case of an evanescent wave,  $\tilde{k}_2$  is purely imaginary, hence we can write

$$\tilde{\beta} = \frac{\mu_1 v_1}{\mu_2 \omega} \operatorname{Im}\{\tilde{k}_2\} \cdot i = \gamma i$$

for some constant

$$\gamma = \frac{\mu_1 v_1}{\mu_2 \omega} \operatorname{Im}\{\tilde{k}_2\}.$$

Since  $\gamma$  is a constant,  $\tilde{\beta}$  cannot be equal to  $\alpha$ , which is purely real. Substituting in equation A.11, we get:

$$\tilde{E}_R = \left( \frac{\alpha - \gamma i}{\alpha + \gamma i} \right) \tilde{E}_I.$$

And using  $|\tilde{E}_R| = \sqrt{\operatorname{Re}\{\tilde{E}_R\}^2 + \operatorname{Im}\{\tilde{E}_R\}^2} = \sqrt{\tilde{E}_R \cdot \tilde{E}_R^*}$ , we write

$$|\tilde{E}_R| = \sqrt{\left( \frac{\alpha - \gamma i}{\alpha + \gamma i} \right) \tilde{E}_I \cdot \left( \frac{\alpha - \gamma i}{\alpha + \gamma i} \right)^* \tilde{E}_I^*}$$

$$\therefore |\tilde{E}_R| = |\tilde{E}_I|$$

Therefore, the **Reflectivity**,  $\mathcal{R} = (\tilde{E}_R / \tilde{E}_I)^2$ , has a magnitude of 1.

### A.3 The Fourier Trick

The Fourier trick of replacing the time derivative  $\frac{d}{dt}$  with  $i\omega$  is a powerful technique used in solving differential equations, particularly in the context of signal processing. This section explains the theory behind this trick, provides the mathematical derivation, and highlights important caveats.

The Fourier transform converts a time-domain signal  $f(t)$  into its frequency-domain representation  $F(\omega)$ , defined as:

$$F(\omega) = \int_{-\infty}^{\infty} f(t)e^{-i\omega t} dt. \quad (\text{A.15})$$

The inverse Fourier transform converts a frequency-domain signal  $F(\omega)$  back to the time domain:

$$f(t) = \frac{1}{2\pi} \int_{-\infty}^{\infty} F(\omega)e^{i\omega t} d\omega. \quad (\text{A.16})$$

To understand how the derivative transforms, we take the Fourier transform of  $\frac{d}{dt}f(t)$ , denoted by  $\mathcal{F}\left\{\frac{d}{dt}f(t)\right\}$ , given by

$$\mathcal{F}\left\{\frac{d}{dt}f(t)\right\} = \int_{-\infty}^{\infty} \frac{d}{dt}f(t)e^{-i\omega t} dt. \quad (\text{A.17})$$

Using integration by parts, where  $u = \frac{d}{dt}f(t)$  and  $dv = e^{-i\omega t} dt$ , we get:

$$\mathcal{F}\left\{\frac{d}{dt}f(t)\right\} = (f(t)e^{-i\omega t})_{-\infty}^{\infty} + i\omega \int_{-\infty}^{\infty} f(t)e^{-i\omega t} dt. \quad (\text{A.18})$$

Assuming that  $f(t)$  vanishes at infinity, the boundary term is zero, and we have:

$$\mathcal{F}\left\{\frac{d}{dt}f(t)\right\} = i\omega F(\omega). \quad (\text{A.19})$$

Thus, the Fourier transform of the time derivative  $\frac{d}{dt}$  corresponds to multiplication by  $i\omega$  in the frequency domain. While the Fourier trick is powerful, several caveats must be noted. First, the integration by parts assumes that the function  $f(t)$  and its derivatives vanish at infinity, which is true for many physical signals but not all. Furthermore, the Fourier transform may not exist for all functions, especially those that are not integrable.

## A.4 Absorption Coefficient

Here I discuss the absorption coefficient and the form it takes in specific propagation cases of interest.

### A.4.1 With Collisions, No Magnetic Field

Following the introduction of collisions in **Section 2.2**, the modification to the dispersion relation of equation 2.9 into equation 2.10 implied that both the index of refraction and the wave vectors take on complex forms as discussed in **Section 2.2**:

$$n = \eta - i\chi \quad (\text{A.20})$$

$$\vec{k} = \tilde{k} = k + i\mathcal{K}. \quad (\text{A.21})$$

The imaginary part of the index of refraction is commensurable with absorption since the electric field takes the form

$$\tilde{E} = \tilde{E}_0 e^{i(\vec{k} \cdot \vec{r} - \omega t)} = \tilde{E}_0 e^{-\mathcal{K}z} e^{i(kz - \omega t)}$$

and

$$n \equiv \frac{c}{\omega} \tilde{k}. \quad (\text{A.22})$$

Therefore,

$$k = \eta \frac{\omega}{c} \quad (\text{A.23})$$

$$\mathcal{K} = \chi \frac{\omega}{c}. \quad (\text{A.24})$$

To reiterate, the dispersion relation derived in **Section 2.2** (equation 2.10), had the form

$$\boxed{n^2 = \epsilon_r = 1 - \frac{\omega_P^2}{\omega^2 \left(1 - i\frac{\nu}{\omega}\right)}}.$$

In the absence of the term

$$Z = \frac{\nu}{\omega}, \quad (\text{A.25})$$

in equation 2.10,  $\chi$  goes to zero, and we retrieve only the real part,  $n^2 = \eta^2 = 1 - X$ . With collisions, we may re-express equation 2.10 as

$$n^2 = (\eta - i\chi)^2 = 1 - \frac{X}{1 - iZ}. \quad (\text{A.26})$$

Since we can write

$$\frac{X}{1+Z^2} = \frac{1}{2} \left( \frac{X}{1+iZ} + \frac{X}{1-iZ} \right),$$

we can rewrite A.26 as

$$\begin{aligned} (\eta - i\chi)^2 &= 1 - \frac{X}{1-iZ} \\ \eta^2 - 2i\eta\chi + \chi^2 &= 1 - \frac{2X}{1+Z^2} - \frac{X}{1+iZ} \\ \eta^2 - 2i\eta\chi + \chi^2 &= 1 - \frac{X}{1+Z^2} - i \frac{XZ}{1+Z^2} \end{aligned}$$

Equating the imaginary parts, we have

$$\begin{aligned} -2i\eta\chi &= -i \frac{XZ}{1+Z^2} \\ \chi &= \frac{1}{2\eta} \frac{XZ}{1+Z^2} \\ \chi &= \frac{1}{2\eta} \frac{\omega_P^2}{\omega} \frac{\nu}{\omega^2 \left(1 + \frac{\nu^2}{\omega^2}\right)} \\ \chi &= \frac{1}{\omega} \frac{e^2}{2m_e\epsilon_0} \frac{1}{\eta} \frac{N_e\nu}{\omega^2 + \nu^2} \end{aligned}$$

and we arrive at equation 2.26

$$\boxed{\mathcal{K} = \frac{e^2}{2m_e\epsilon_0 c} \frac{1}{\eta} \frac{N_e\nu}{\omega^2 + \nu^2}}.$$

#### A.4.2 Quasi-Longitudinal, Trans-ionospheric Waves

The introduction of Earth's magnetic field in **Section 2.3** modified the dispersion relation of **Section 2.2**,

after collisions were accounted for (equation 2.10), as per the Appleton-Hartree treatment to that of equation

A.51:

$$\boxed{n^2 = 1 - \frac{X}{U - \frac{Y_T^2}{2(U-X)} \pm \sqrt{\frac{Y_T^4}{4(U-X)} + Y_L^2}}}.$$

The full derivation of this dispersion relation is complex, and is not needed for the forthcoming analysis.

However, a complete derivation can be found in the following section (**Appendix A.5**). Here, I only examine a specific case of interest to my research, that of trans-ionospheric waves under the quasi-longitudinal approximation. The quasi-longitudinal approximation, introduced in **Section 2.3.2**, reduced the Appleton-

Hartree equation to equation 2.11:

$$n^2 = 1 - \frac{X}{U \pm Y_L}.$$

Multiplying by the complex conjugate and equating the imaginary parts, we get

$$\begin{aligned}\eta^2 - 2i\eta\chi + \chi^2 &= 1 - \frac{X(1 \pm Y_L + iZ)}{(1 \pm Y_L - iZ)(1 \pm Y_L + iZ)} \\ -2i\eta\chi &= -i \frac{XZ}{(1 \pm Y_L)^2 + Z^2}.\end{aligned}$$

For trans-ionospheric propagation, where  $\eta \approx 1$ , this yields

$$\begin{aligned}\chi &= \frac{1}{2} \frac{XZ}{(1 \pm Y_L)^2 + Z^2} \\ \chi &= \frac{1}{\omega} \frac{e^2}{2m_e \epsilon_0} \frac{N_e \nu}{\omega^2 \left( (1 \pm Y_L)^2 + \left(\frac{\nu}{\omega}\right)^2 \right)}.\end{aligned}$$

Finally, since  $\cos \theta \approx 1$ ,  $Y_L \approx \frac{\omega_c}{\omega}$ , and the absorption coefficient now takes the form of equation 2.29:

$$\mathcal{K} \approx \frac{e^2}{2m_e \epsilon_0 c} \frac{N_e \nu}{(\omega \pm \omega_c)^2 + \nu^2}.$$

## A.5 Appleton-Hartree Equation

Continuing with the derivation started in **Section 2.3**, the modification to the equation of motion leads to the following

$$m_e \frac{\partial^2 \vec{r}}{\partial t^2} = -e\vec{E} - m_e\nu \frac{\partial \vec{r}}{\partial t} - e \frac{\partial \vec{r}}{\partial t} \times \vec{B}$$

$$m_e(i\omega)^2 \vec{r} = -e\vec{E} - m_e\nu(i\omega)\vec{r} - e(i\omega)\vec{r} \times \vec{B}$$

Multiplying by  $\frac{N_e e}{m_e \omega^2}$ :

$$-N_e e \vec{r} = -\frac{N_e e^2}{m_e \omega^2} \vec{E} + i \frac{-N_e e \nu \vec{r}}{\omega} - i e \frac{N_e e \vec{r}}{m_e \omega} \times \vec{B}$$

$$\vec{P} = -\epsilon_0 X \vec{E} + i \frac{\nu}{\omega} \vec{P} + i \frac{e}{m_e \omega} \vec{P} \times \vec{B}$$

$$\epsilon_0 X \vec{E} = \vec{P}(-1 + iZ) + i \frac{e}{m_e \omega} \vec{P} \times \vec{B}$$

$$-\epsilon_0 X \vec{E} = \vec{P}(1 - iZ) - i \frac{e}{m_e \omega} \vec{P} \times \vec{B},$$

where the term

$$\omega_c = \frac{e \|\vec{B}\|}{m_e} \quad (\text{A.27})$$

is the electro *Gyrofrequency*, and it is customary to define the vector

$$\vec{Y} = -\frac{\omega_c}{\omega} \hat{B}, \quad (\text{A.28})$$

and the quantity,

$$U = 1 - iZ, \quad (\text{A.29})$$

to simplify the notation. This leads to the following equation, which decomposes into a set of 3 equations,

$$\boxed{-\epsilon_0 X \vec{E} = U \vec{P} + i \vec{P} \times \vec{Y}} \left\{ \begin{array}{l} -\epsilon_0 X E_x = U P_x + i (\vec{P} \times \vec{Y})_x \\ -\epsilon_0 X E_y = U P_y + i (\vec{P} \times \vec{Y})_y \\ -\epsilon_0 X E_z = U P_z + i (\vec{P} \times \vec{Y})_z \end{array} \right. \quad (\text{A.30})$$

To simplify the analysis, we start with a monochromatic plane wave (see **Appendix A.2.1** for the justification for plane waves), propagating in the  $\hat{z}$  direction, and orient the wave normal such that the magnetic

field lies in the xz-plane, or

$$\vec{B} \cdot \hat{z} = B \cos \theta \quad (\text{A.31})$$

$$\vec{B} \cdot \hat{x} = B \sin \theta. \quad (\text{A.32})$$

This orientation allows us to make useful approximations later by defining longitudinal,  $Y_L$ , and traverse,  $Y_T$ , components for the vector  $\vec{Y}$  associated with the external magnetic field as

$$Y_L = Y_z = \frac{\omega_c}{\omega} \cos \theta \quad (\text{A.33})$$

$$Y_T = Y_x = \frac{\omega_c}{\omega} \sin \theta. \quad (\text{A.34})$$

The electric field of the wave propagating in the  $\hat{z}$  is given by

$$\tilde{E} = \tilde{E}_0 e^{i(\vec{k} \cdot \vec{r} - \omega t)} = \tilde{E}_0 e^{i(\tilde{k}z - \omega t)}. \quad (\text{A.35})$$

Using the Fourier trick (see **Appendix A.3**), taking first-order temporal and spatial derivatives of equation A.35, we get

$$\frac{\partial \tilde{E}}{\partial t} = -i\omega \tilde{E} \quad (\text{A.36})$$

$$\frac{\partial \tilde{E}}{\partial z} = -ik\tilde{E}. \quad (\text{A.37})$$

Using Maxwell's equation for the curl of the electric field,

$$\vec{\nabla} \times \vec{E} = -\mu_0 \frac{\partial \vec{H}}{\partial t}, \quad (\text{A.38})$$

where  $\vec{H}$  is the auxiliary field and  $\mu_0$  is the permeability of free space, and employing the above derivative, we obtain

$$\begin{aligned} & \left( \frac{\partial E_z}{\partial y} - \frac{\partial E_y}{\partial z} \right) \hat{x} - \left( \frac{\partial E_z}{\partial x} - \frac{\partial E_x}{\partial z} \right) \hat{y} + \left( \frac{\partial E_y}{\partial x} - \frac{\partial E_x}{\partial y} \right) \hat{z} = i\omega \mu_0 \vec{H} \\ & -ikE_y \hat{x} + ikE_x \hat{y} = i\omega \mu_0 \vec{H} \\ & \vec{H} = \frac{k}{\mu_0 \omega} (-E_y \hat{x} + E_x \hat{y}). \end{aligned}$$

Using Maxwell's equation for the curl of the auxiliary field, we obtain a system of equations

$$\nabla \times \vec{H} = \frac{\partial \vec{D}}{\partial t} = \begin{cases} \frac{\partial H_y}{\partial z} = i\omega D_x \\ \frac{\partial H_x}{\partial z} = -i\omega D_y \\ D_z = 0 \end{cases} \quad (\text{A.39})$$

where  $\vec{D}$  is the displacement vector, which can now be written as

$$\vec{D} = \frac{k^2}{\mu_0 \omega^2} (E_x \hat{x} + E_y \hat{y}), \quad (\text{A.40})$$

or,

$$\begin{aligned} \vec{D} &= \epsilon_0 \frac{k^2}{\mu_0 \epsilon_0 \omega^2} (E_x \hat{x} + E_y \hat{y}) \\ \vec{D} &= \epsilon_0 n^2 (E_x \hat{x} + E_y \hat{y}), \end{aligned}$$

since

$$n \equiv k \frac{c}{\omega}. \quad (\text{A.41})$$

Using the displacement vector,

$$\vec{D} = \epsilon \vec{E} = \epsilon_0 \vec{E} + \vec{P}, \quad (\text{A.42})$$

we can write

$$\vec{P} = \epsilon_0 (n^2 - 1) (E_x \hat{x} + E_y \hat{y}) - \epsilon_0 E_z \hat{z}. \quad (\text{A.43})$$

Notice that the components of the displacement, polarization, and auxiliary field vectors are related to the electric field components by:

$$\frac{D_y}{D_x} = \frac{P_y}{P_x} = -\frac{H_x}{H_y} = \frac{E_y}{E_x}. \quad (\text{A.44})$$

Using equations A.43 and A.44, we can revisit the set of 3 equations A.30, to write

$$-\epsilon_0 X E_x = U P_x + i P_y Y_L \quad (\text{A.45})$$

$$-\epsilon_0 X E_y = U P_y - i P_x Y_L + i P_z Y_T \quad (\text{A.46})$$

$$-\epsilon_0 X E_z = U P_z - i P_y Y_T. \quad (\text{A.47})$$

From equation A.45, and using the x-component of equation A.43,  $P_x = \epsilon_0(n^2 - 1)E_x$  we get

$$n^2 = 1 - \frac{X}{U + i\frac{P_y}{P_x}Y_L}. \quad (\text{A.48})$$

From equation A.47, and using the z-component of equation A.43,  $P_z = -\epsilon_0 E_z$  we get

$$P_z = i\frac{Y_T P_y}{U - X}.$$

Dividing equation A.46 by A.45 and substituting for  $P_z$  we get

$$\frac{P_y}{P_x} = \frac{-iY_L + \frac{P_y}{P_x}\left(U - \frac{Y_T^2}{U - X}\right)}{U + i\frac{P_y}{P_x}Y_L}, \quad (\text{A.49})$$

where we used  $\frac{P_y}{P_x} = \frac{E_y}{E_x}$  and divided the numerator and denominator on the right-hand side by  $P_x$ . After rearranging, equation A.49 is a quadratic equation for  $p = P_y/P_x$ , rewritten as

$$p^2 - ip\frac{Y_T^2}{Y_L^2(U - X)} + 1 = 0$$

with  $A = C = 1$  and  $B = -i\frac{Y_T^2}{Y_L^2(U - X)}$ , and

$$p = \frac{-B \pm \sqrt{B^2 - 4AC}}{2A},$$

leading to

$$p = i\frac{Y_T^2}{2Y_L(U - X)} \pm i\sqrt{\frac{Y_T^4}{4Y_L^2(U - X)^2} - 1}. \quad (\text{A.50})$$

Substituting this last equation(A.50) in that for the index of refraction (A.48, we finally arrive at the Appleton-Hartree equation:

$$n^2 = 1 - \frac{X}{U - \frac{Y_T^2}{2(U - X)} \pm \sqrt{\frac{Y_T^4}{4(U - X)^2} + Y_L^2}}.$$

(A.51)

The most important property of the medium as gleaned from this equation is anisotropy: different propagation characteristics in different directions with respect to Earth's magnetic field. In the absence of the

geomagnetic field,  $Y_T = Y_L = 0$  and  $n^2 = 1 - \frac{X}{U}$  as obtained in **Section 2.2**.

# Appendix B

## Realtime Baselining

### B.1 Baselining

During my work with the HSRs, I was tasked with developing a method for generating automatic, realtime baselines. There are two major problems to address in that regard:

1. The multi-frequency riometers (HSRs) allow too much noise into the receiver, and the noise varies by frequency bin.
2. Aggregating quiet times for baseline generation is difficult to automate since there are many sources of noise that plague the data. There are in general two categories of noise in this context:-
  - **Positive:** Solar radio bursts, local interference, or otherwise; noise that increase signal level.
  - **Negative:** Absorption decreases signal level.

Therefore, the method developed should be able to account for these two types. Sample raw data from PFRR at multiple frequencies shows both absorption and interference, displayed in **Figure B.1**. Black and brown are used to distinguish between consecutive days, to showcase the time evolution of noise. Of particular interest is how the noise abruptly disappears after the 22<sup>nd</sup>, where there is a small gap in the data. This happens frequently: noise accumulates in the receiver, perhaps due to overheating, and the operations team lead performs a power cycle, which leaves a gap in the data, but then the noise almost entirely disappears. Other 'positive' noise appears towards the end of the 26<sup>th</sup>. Absorption spikes on the other hand, bring down the signal level.

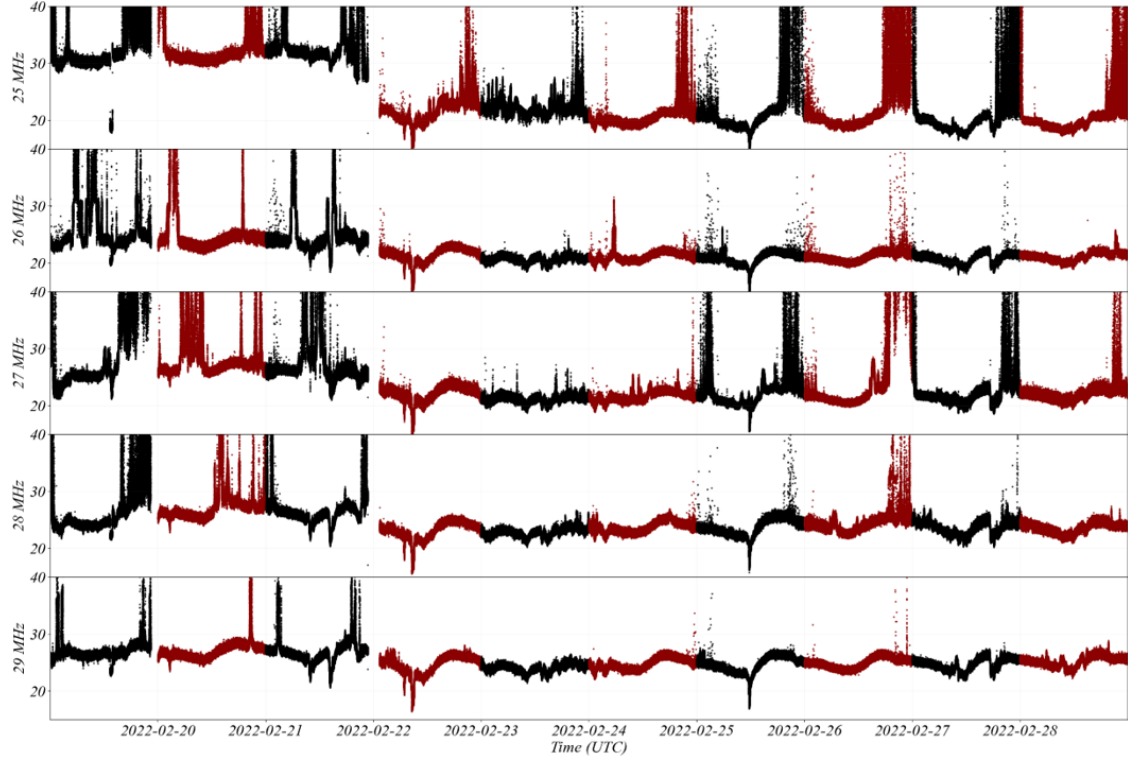


Figure B.1: Example of raw HSR data at various frequencies. Data is contaminated by interference (positive spikes in power level) and absorption (negative spikes in signal level). These noise sources evolve with time, with many factors at play.

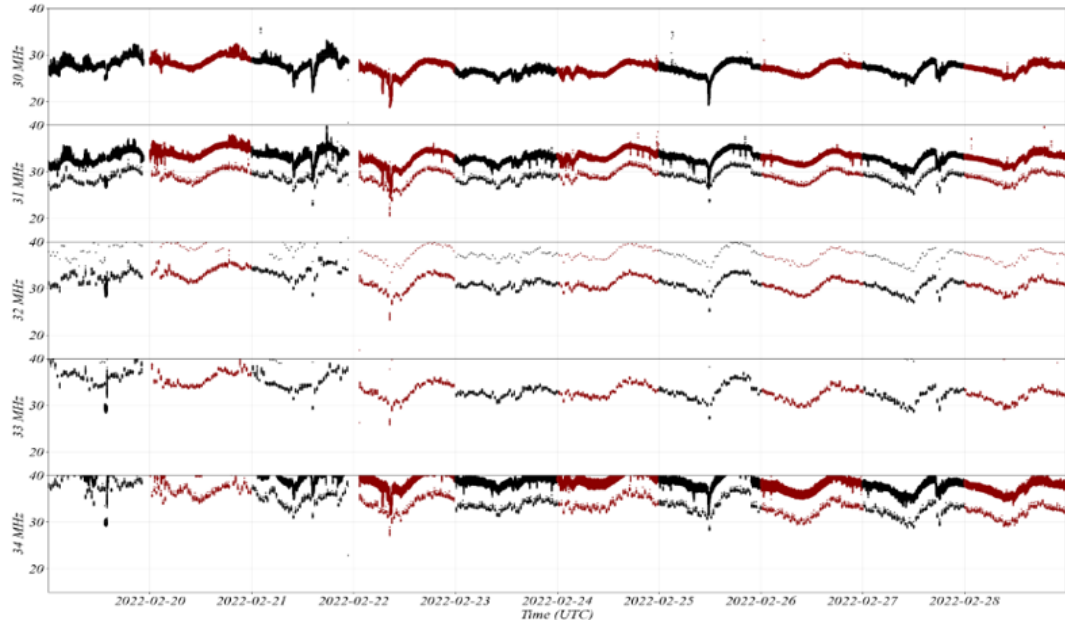


Figure B.2: An example of signal level taking multiple values as a function of time for specific frequency bins.

There are, however, other manifestations of noise. For example, the signal can split such as shown in **Figure B.2**. In such cases, the frequency bin must be avoided. Other manifestations, such as the “waving” or “ticking”, shown in **Figures B.3** and **B.4**, respectively. The latter two can be detected using a high-pass filter. For example, the data from various bins around 30 MHz in **Figure B.5** shows the bins with ‘ticking’ in red. Applying a low-pass filter to the data, by convolving it with a Kaiser window, shown in **Figure B.6**, shows that all of the bins have the underlying ticking, as shown in **Figure B.7**. One can ignore these ticks, by inverting the curve, finding its peaks, and then inverting back. Shown in red in **Figure B.8** is the filtered signal curve, without the underlying ticking.

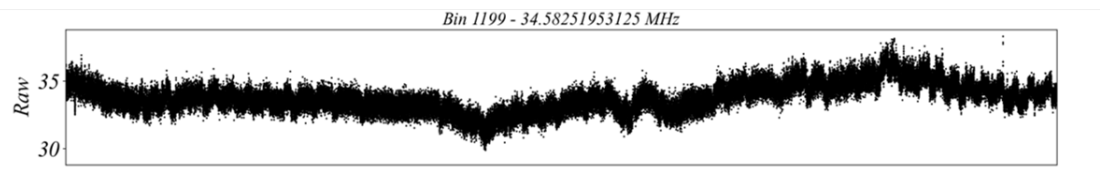


Figure B.3: Example of raw signal taking a wave form, analogous to a carrier signal.

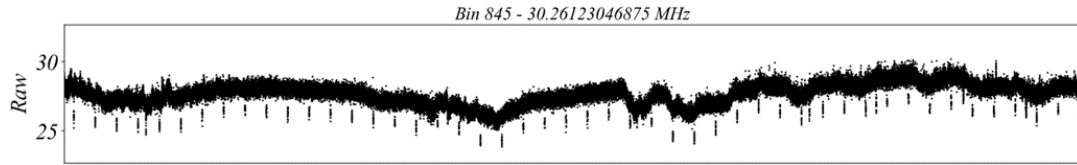


Figure B.4: Example of low frequency ticks within the data.

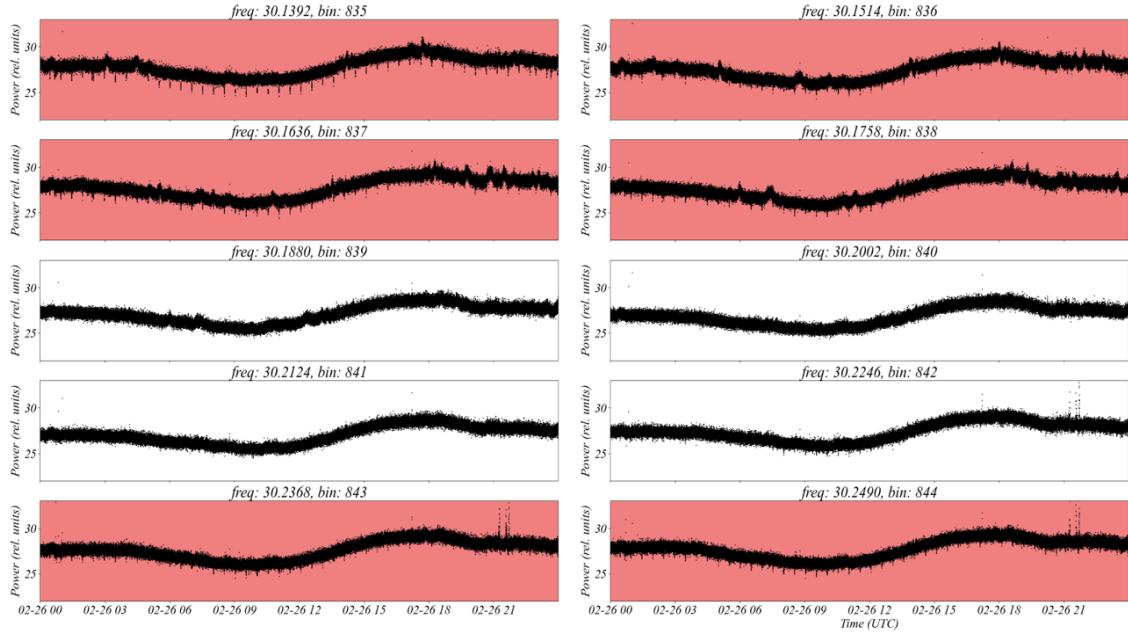


Figure B.5: Raw signal at various frequency bins around 30 MHz. Some bins, highlighted in red, exhibit the 'ticking' underlying signal.

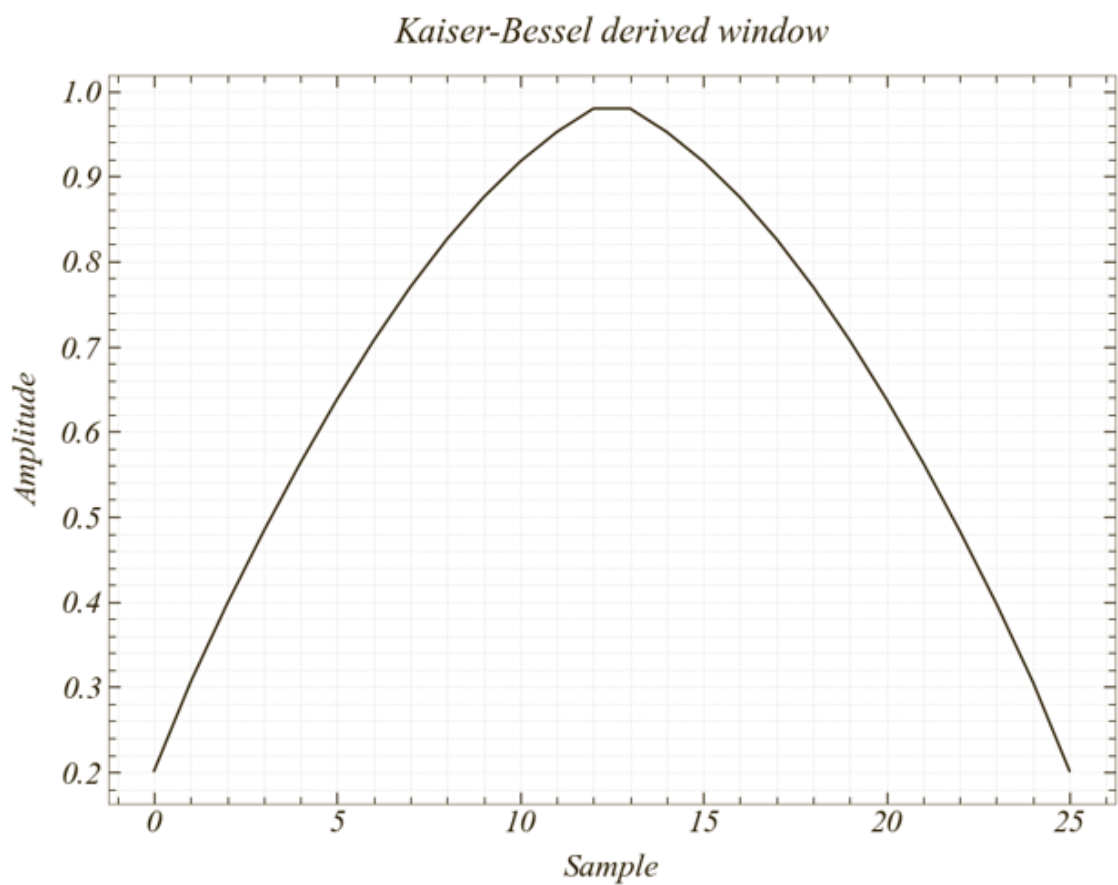


Figure B.6: The Kaiser window used to extract the 'ticking'.

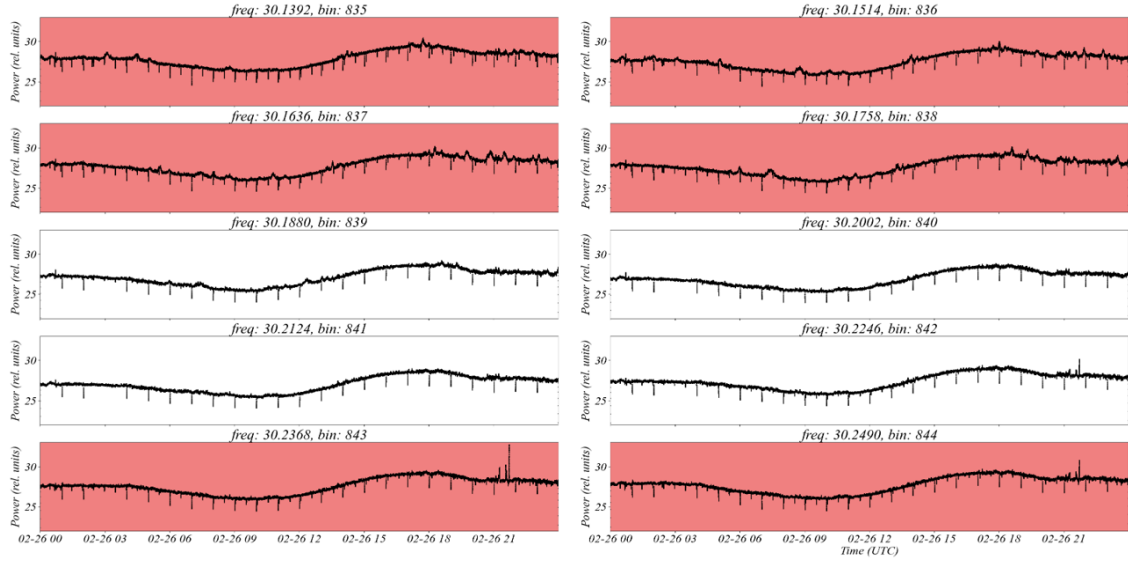


Figure B.7: Same as **Figure B.5** but the data is convolved with the Kaiser window in **Figure B.6**.

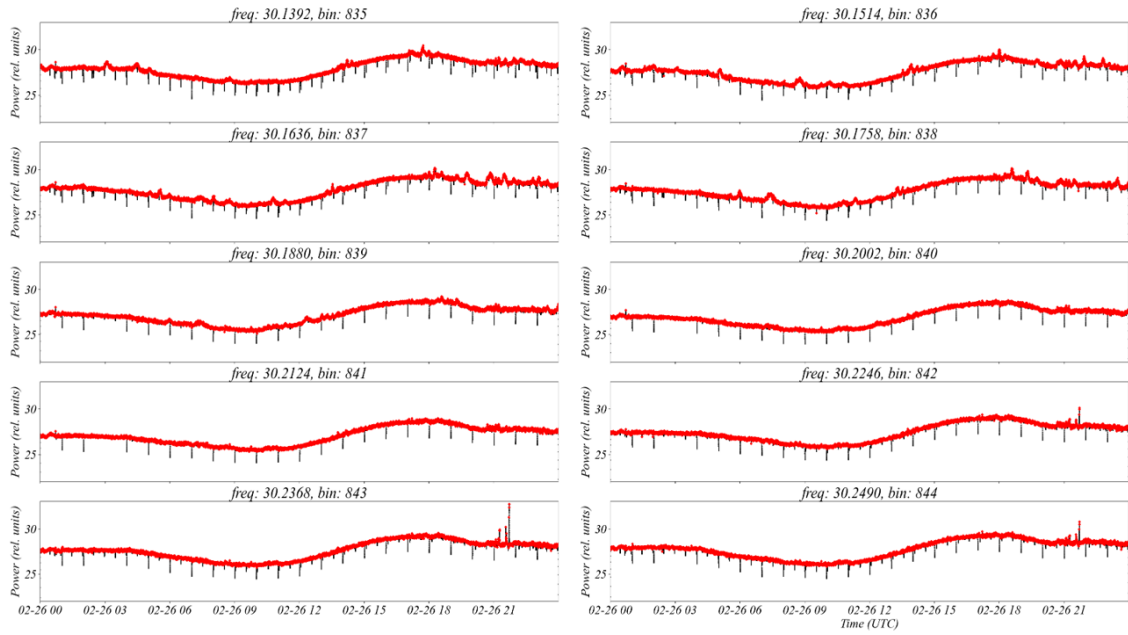


Figure B.8: Same as **Figure B.7**, but the envelope of the data, without the ticking is shown in red.

Extracting such ticks becomes more tedious for bins with more noise. **Figure B.9** shows one such bins. Taking the FFT, one can see many underlying tones. Instead, of cleaning the bins, one should eliminate the noisy ones. A scoring system is made such that a bin with more of the aforementioned features has a higher score, and should be eliminated. The scores are standardized individually for each bin and each time period, since, as we saw earlier, each bin's noise evolves differently in time.

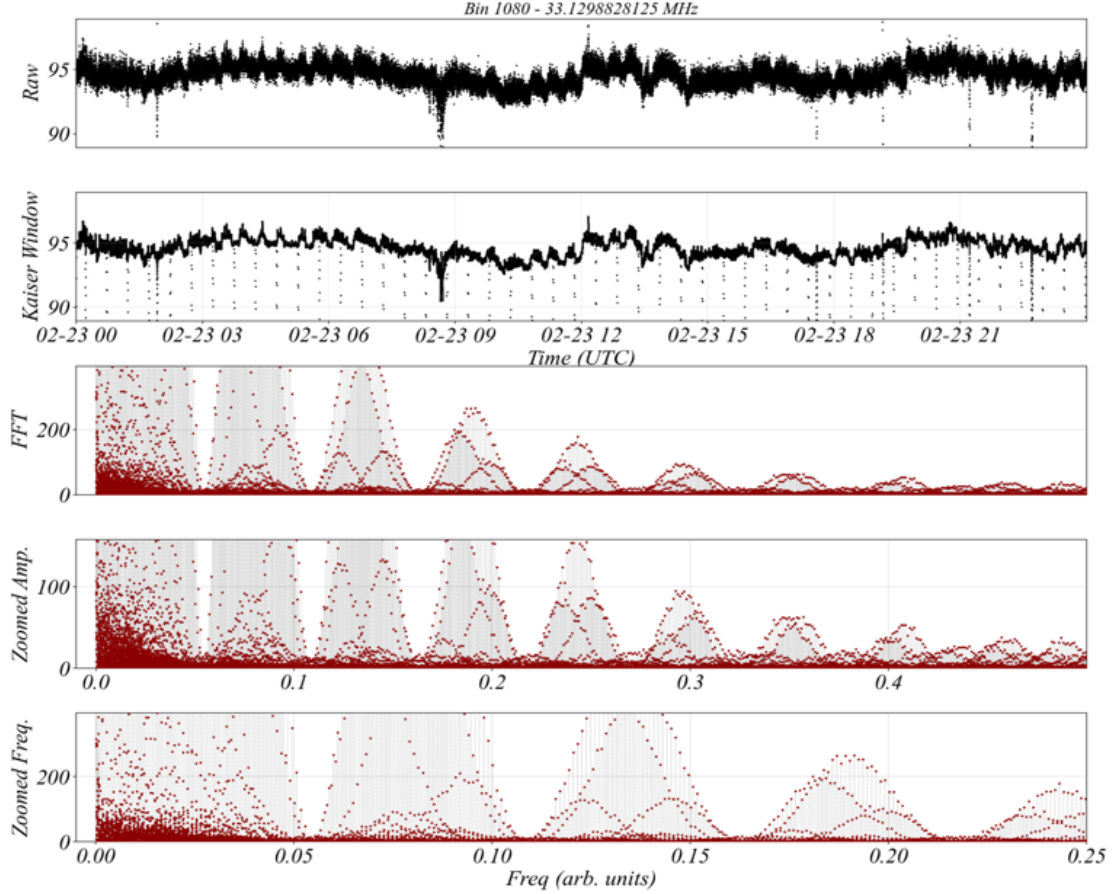


Figure B.9: An example of a heavily contaminated frequency bin. The same Kaiser window fails to detect any specific underlying signal that can be filtered. An FFT shows complicated harmonics. Zoomed-in versions of the FFT in both amplitude and frequency are included for illustration.

Noise can also come in the form of short bursts. An example of such noise occurs around 12 UTC for the data shown in **Figure B.10**. I developed an algorithm that can detect such noise based on the following ideas:

1. The distribution of power values during noisy times can be complex (e.g., bimodal, hyper-tailed, etc.).
2. The distribution of power measurements during quiet times should be a Gaussian, if considering short enough time intervals, on the order of 30 min to 1 hr.

3. Gaussians and ONLY Gaussians have only 1<sup>st</sup> and 2<sup>nd</sup> order cumulants.
4. The sum of two or more Gaussians is also a Gaussian.
5. Any deviation from a Gaussian for power measurements that span an hour can therefore be used to detect a noisy hour.

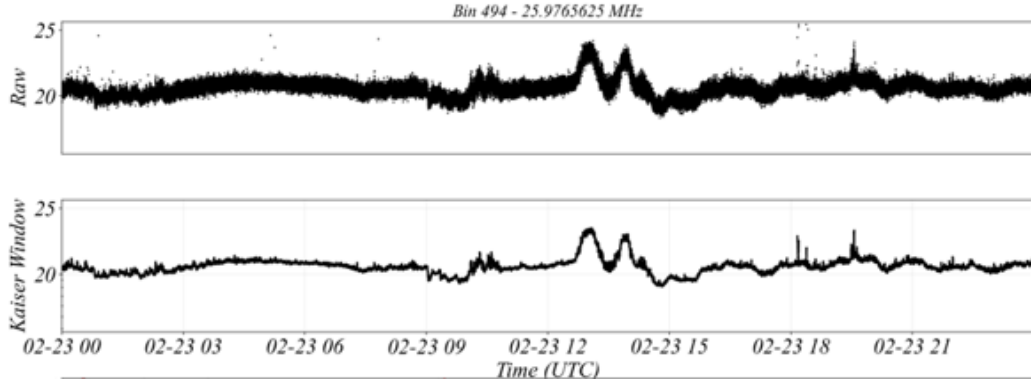


Figure B.10: An example of noise bursts, lasting on the order of an hour.

The distribution of power measurements for the four hours starting at 12 UTC (from the data in **Figure B.10**) is shown in **Figure B.11**. All the distributions before 15 UTC showcase the noisy nature of the data. For 15 UTC, the distribution starts resembling a Gaussian. While this method was able to detect positive noise accurately, as highlighted in red in **Figure B.12**, it could not always do the same for absorption.

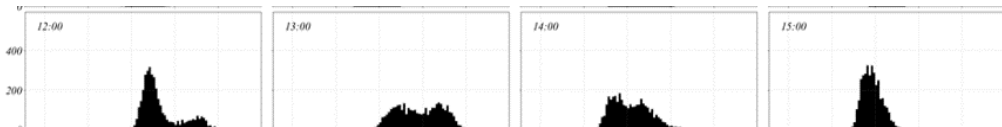


Figure B.11: The power distributions of the data from **Figure B.10** spanning 12–13, 13–14, 14–15 and 15–16 UTC, in that order.

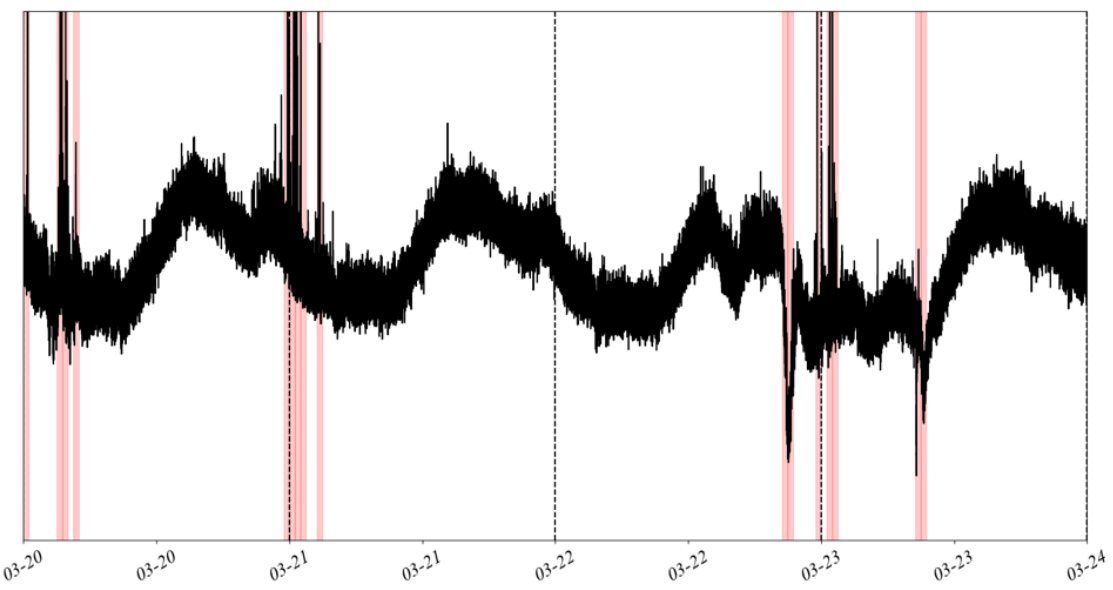


Figure B.12: A plot showcasing accuracy of the hourly distribution algorithm, where red highlights a noisy hour.

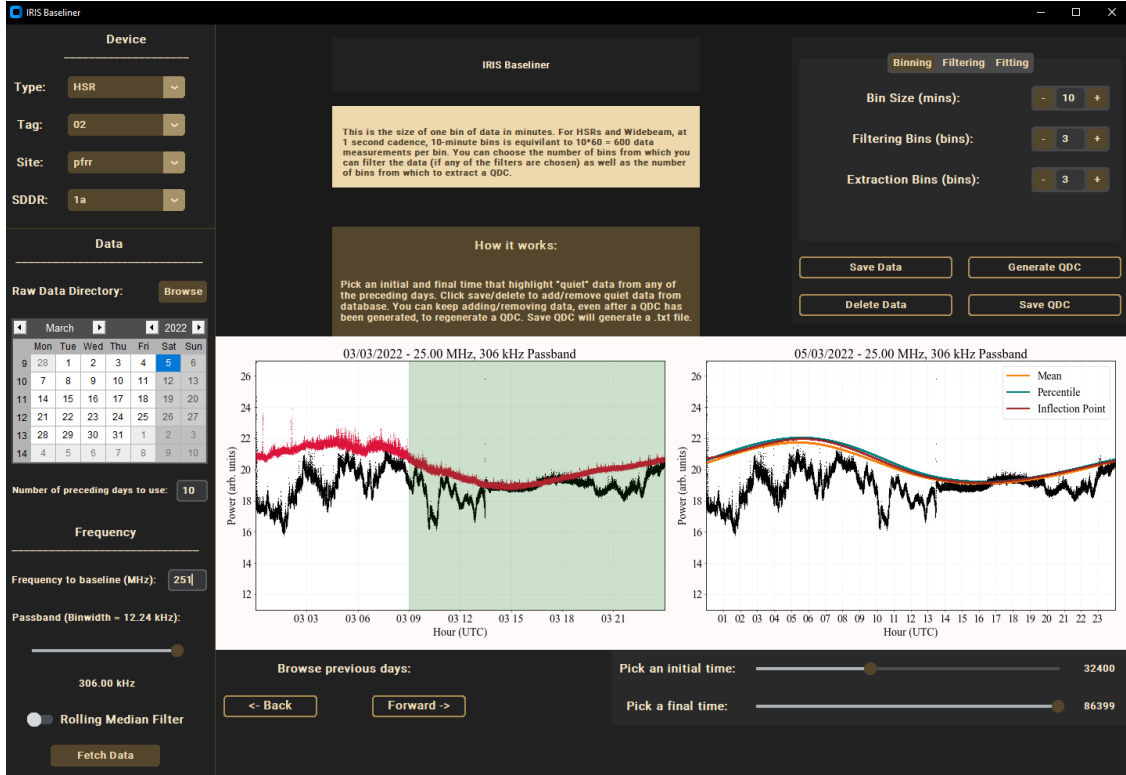


Figure B.13: A screenshot taken from my manual baseliner application in its beta stages of development.

After a specific bin has been deemed free of noise for a given day, that bin becomes a suitable candidate for baseline generation. The only remaining problem becomes that of identifying quiet times. While ‘positive’ noise can be detected using the aforementioned methods, absorption is harder to detect using such methods. Instead, I opted for an iterative process, starting from a manually generated baseline. If, let’s say, 30 MHz was deemed noise-free, then I will manually generate a baseline at that frequency by picking the quiet times myself. I do this using an application I had developed for manual baselining, a screenshot of which is shown in **Figure B.13**. It lets the user pick quiet times over an extended period, ideally more than 7 days prior to some day of interest. The data is aggregated in a large matrix that bins the data according to sidereal time. The user can employ some filtering and fitting and the application outputs a QDC for that day that is continuous in sidereal time.

Using that manual QDC at 30 MHz (30 MHz is an example, but this can be applied to any frequency) as a starting point is the only non-automated part of this methodology. From there, I can exclude absorption times as they constitute negative excursions from the QDC. Around 30 MHz, there might be bins that should not be used. According to the number of issues (as presented above) a bin has, it should be scored and eliminated. Only noise-free bins can be used to form the passband of the K0 level (after raw) data. Then,

since we know the absorption times and can deduce the noisy times using the hourly distribution of power measurements, the quiet times can be found. Power measurements for the quiet times is then added to the QDC look-up-table, and a baseline for the next day is generated. A mind map of this algorithm is shown in **Figure B.14**.

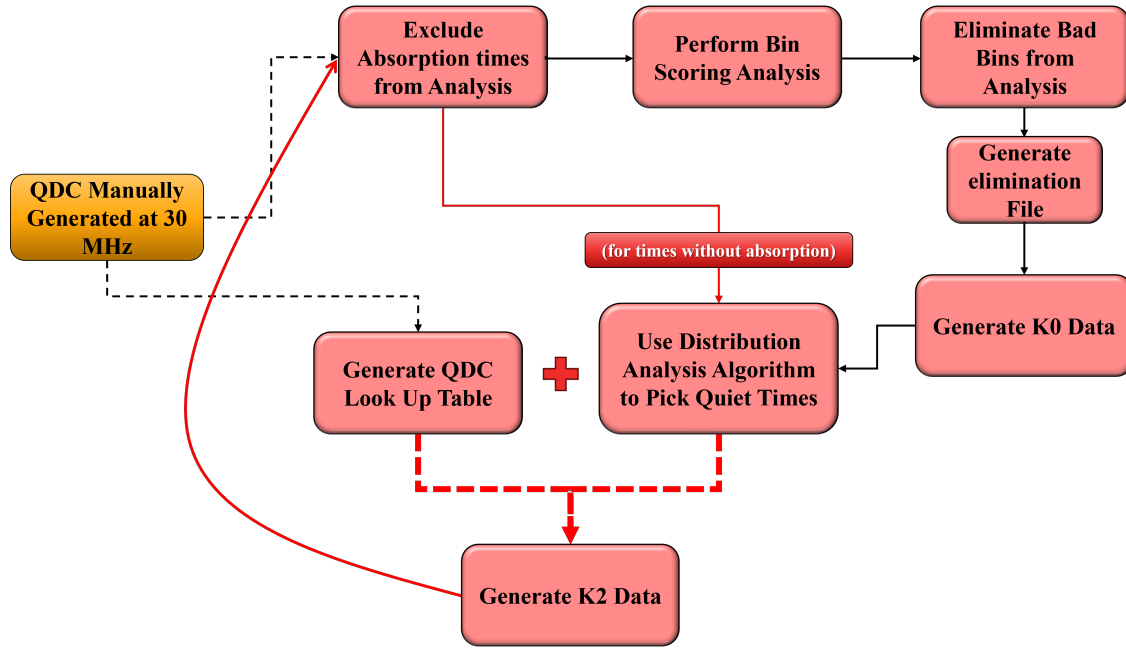


Figure B.14: A mind map of the iterative baselining procedure.

Starting with a manual QDC for 28 February 2022, for data at PFRR, as shown in red in **Figure B.15**, I can detect the absorption times, shown in blue. Applying the hourly distribution algorithm, I can detect the positive noise in red. The rest of the day is deemed quiet and is added to the QDC look-up-table to generate a QDC for the next day. The process is repeated for each next day, producing near-realtime QDCs, as shown in **Figure B.16**.

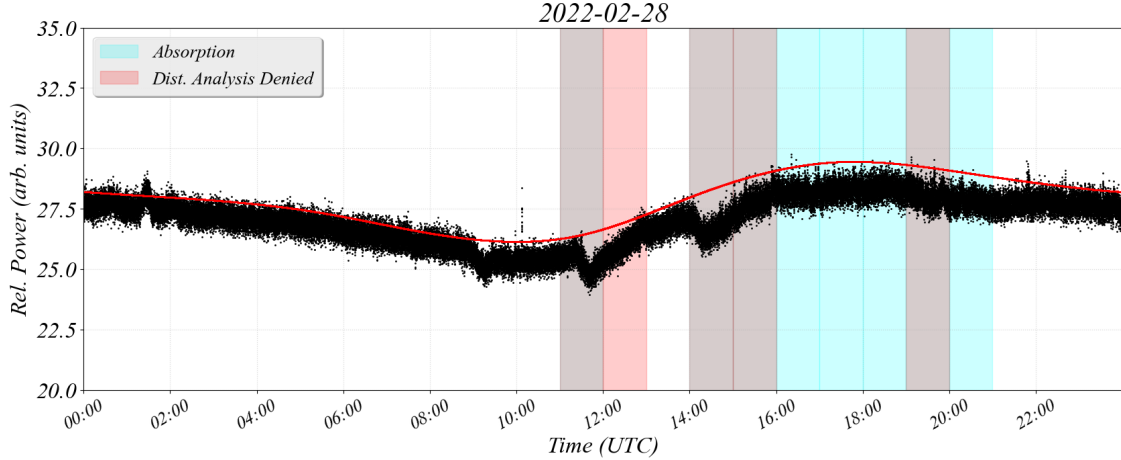


Figure B.15: A plot of signal level for the 28<sup>th</sup> of February for data from PFRR, used to showcase the baselining procedure in action. The raw data is shown in red. Quiet data from the 7 previous days is used to generate the baseline, shown in red. From there, the algorithm starts detecting absorption, highlighted in light blue, and uses the hourly distribution algorithm to highlight interference (red). The hourly distribution sometimes (but not always) detects absorption, where the two colors overlap.

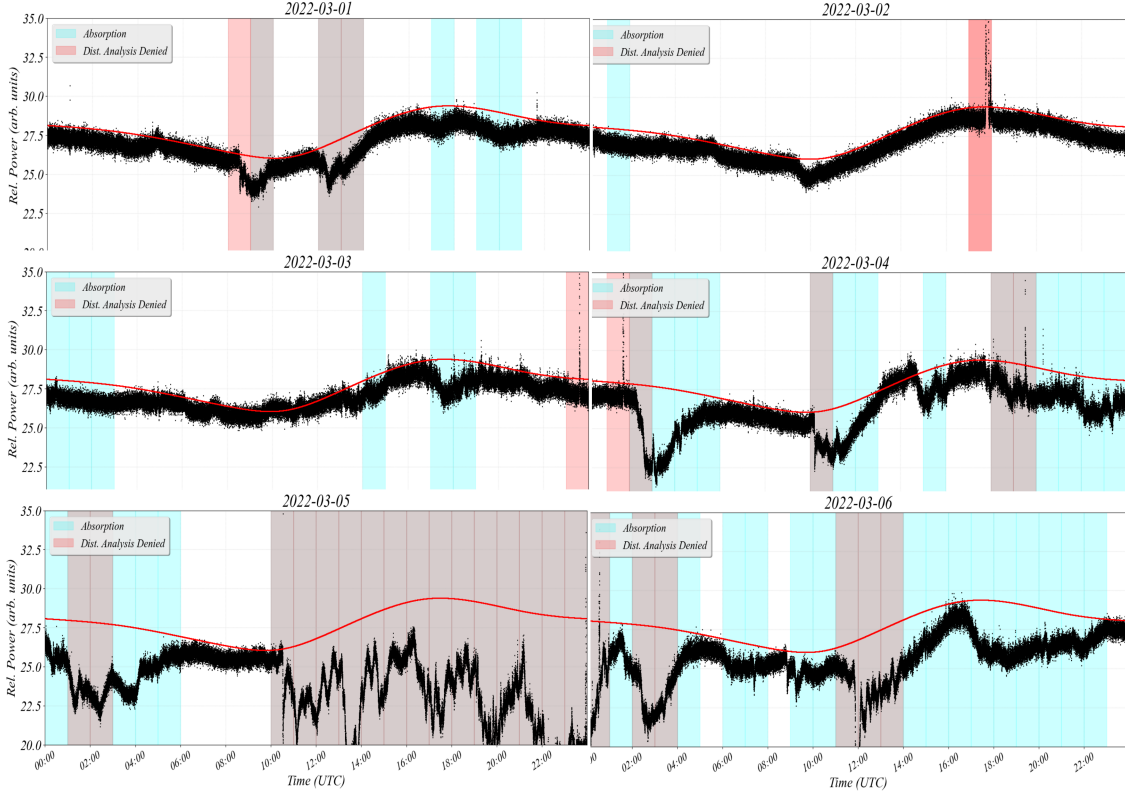


Figure B.16: Example application of the iterative procedure to multiple days following the 28<sup>th</sup> (**Figure B.15**), by taking the quiet time data (data at times void of noise or absorption) and binning them in sidereal time to generate a new QDC for the next day, iterating with each day.

While, here, I show how this methodology works for baselining a day at a time, one can go down to a lower cadence if desired. To do so, starting with a day's QDC, one would go through each hour. If an hour has either positive or negative noise, the data within that hour are discarded. Otherwise, the data are added to the manual QDC database, and a new baseline is generated. This recursive process can be done at an hourly cadence. However, I do not advise using a lower temporal resolution, since the hourly distribution of power values (or voltage) was most appropriate for identifying positive spikes, and negative deviations can be too small within, say, 30 min, for absorption to be detected.

## B.2 Frequency Dependence

A note about the the inverse square law derived earlier in **Section 2.3** is in order. One expects that after generating baselines, the absorption measurement would scale as

$$A \propto \frac{1}{f^2}.$$

However, while generating manual baselines, I ran into an unexpected result. I observed the absorption to be higher for the higher frequencies. **Figures B.17 and B.18** show that inconsistency. The degree of absorption, measured as the deviation of the signal measurements (black) from the QDC (orange) is higher for 41 MHz than for 25 MHz.

I discuss this issue further in **Section 6.2.2**.

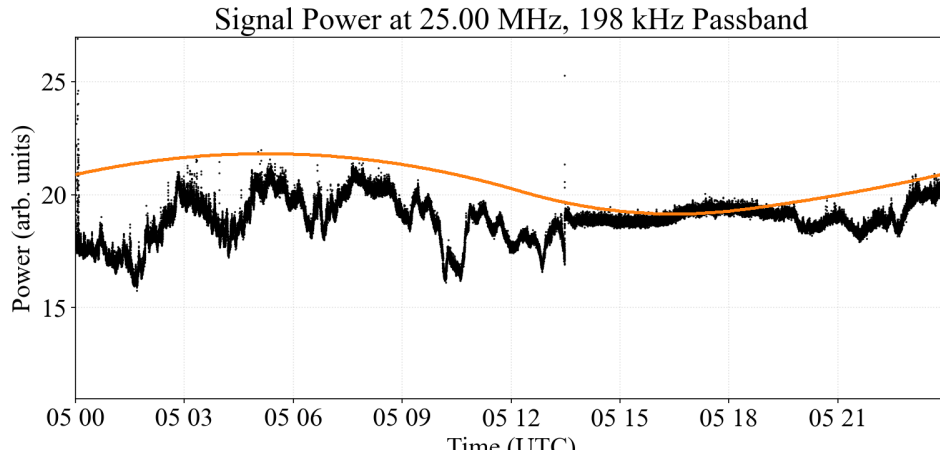


Figure B.17: A plot showing the manually generated baseline for 25 MHz. Raw data is shown in black and the QDC is shown in orange.

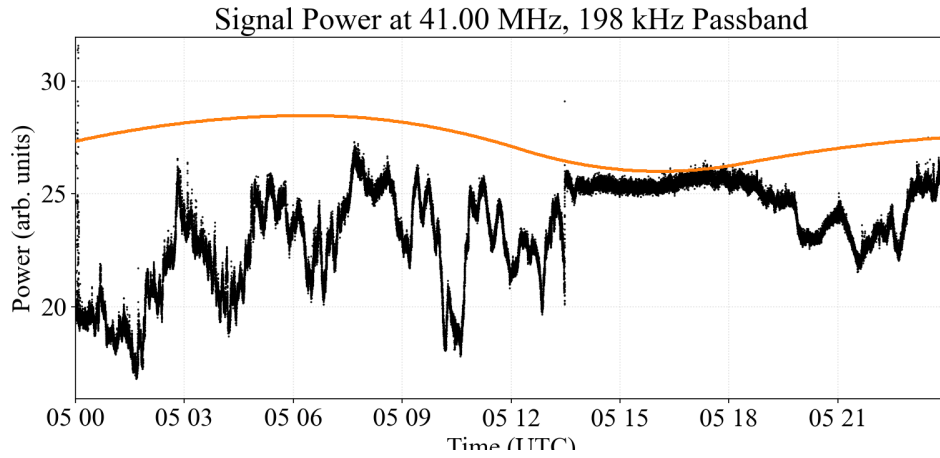


Figure B.18: Same as **Figure B.17** but for 41 MHz. The deviation from the baseline is much higher!

## Appendix C

# International Standard HF

## Propagation Nomenclature

Throughout this thesis, I use terminology to describe radiowave propagation in the ionosphere. In the following, I shall document these terms, providing a simple definition for each that complies the the Institute of Electrical and Electronics Engineers standards (“IEEE Standard Definitions of Terms for Radio Wave Propagation”, 1998).

### Nomenclature

Plasma Frequency, $f_p$	The frequency of the plasma oscillations.
Skywave	Signals that propagate via successive refraction through Earth’s ionosphere and reflections from the ground.
Trans-ionospheric	Signals that penetrate the ionosphere without significant refraction.
Ground Range, $R$	The travelled distance of the radiowave, projected to the ground.
Virtual Height, $h'$	The height of the reflecting layer if successive refractions are modelled as one reflection.
Maximum Usable Frequency (MUF)	The maximum frequency that can be used to establish a radio link between two locations.
Least Usable Frequency (LUF)	The lowest frequency that can be used to establish a radio link between two locations.

Absorption (dB)	The attenuation (in decibels) of a radio signal as it propagates through the medium.
Ordinary/Extraordinary (O/X-mode)	Referring to the different propagation modes allowed for in the presence of Earth's magnetic field.
Radiation Pattern	The gain or sensitivity pattern of the radio antenna.